Journal of Aerosol Science 192 (2026) 106716

Contents lists available at ScienceDirect

Journal of Aerosol Science

journal homepage: www.elsevier.com/locate/jaerosci

Assessment of the predictive ability of standard and refined laser-induced incandescence models against experimental databases from the literature – A benchmarking analysis of commonly used modeling approaches

R. Lemaire [a,*], S. Menanteau [b]

[a] TFT laboratory, Department of Mechanical Engineering, École de Technologie Supérieure, Montreal, Quebec, H3C 1K3, Canada
[b] Icam School of Engineering, Lille Campus, 6 rue Auber, B.P 10079, Cedex, 59016, Lille, France

ARTICLE INFO

Keywords:
Soot particles
Laser-induced incandescence
Model
Benchmarking analysis
Parameterization

ABSTRACT

Laser-induced incandescence (LII) has become a workhorse of particulate measurement. Interpreting measured signals properly, while inferring soot properties and/or physical parameters needed for signal simulations, however, requires developing modeling tools capable of predicting the radiative emission from laser-heated soot. Although significant effort has gone into gaining an in-depth understanding of the physical processes driving the LII phenomenon, the validity of current models, which are based on soot unsteady nanoscale heat and mass balances, is still subject to large uncertainties. The variability in the results from different simulation tools notably stems from their widely diverging formulations and parameterizations. Efforts must thus be directed at determining the critical energy and mass balance mechanisms, formulating the equations accounting for these mechanisms, estimating underlying parameters, and proposing adapted model validation protocols. To address these issues, the present work, which first proposes a detailed review of LII modeling approaches commonly used in the literature, aims at assessing the predictive capability of a series of LII simulation tools against various published datasets. Overall, 21 model formulations and 236 parameterizations were tested, and to the best of the authors' knowledge, this benchmarking analysis ranks as the most comprehensive of its kind. This paper also includes sensitivity analyses focusing on the values and/or expressions used to represent the thermal and mass accommodation coefficients as well as the density, heat capacity and absorption properties of soot, while analyzing the impact of the formulation used to account for the annealing, oxidation, sublimation and thermionic emission processes. To conclude, the predictive capability of a comprehensive model integrating terms representing the saturation of linear, single- and multiphoton absorption processes, non-thermal photodesorption of carbon clusters and corrective factors accounting for the shielding effect and multiple scattering within aggregates, was evaluated against data collected in laminar and turbulent spray flames of gaseous and liquid fuels stabilized under both atmospheric and high-pressure conditions. Although this work does not set out to identify a model which should be considered as universally valid, it still contributes to highlighting the potential strengths and weaknesses of particular models and sub-models, depending on targeted applications, while proposing insights into how to parameterize them. The detailed analysis proposed should thus be of interest for the

* Corresponding author. École de technologie supérieure, Montréal, Department of Mechanical Engineering, Québec, H3C 1K3, Canada.
E-mail address: romain.lemaire@etsmtl.ca (R. Lemaire).

https://doi.org/10.1016/j.jaerosci.2025.106716
Received 14 July 2025; Received in revised form 10 September 2025; Accepted 9 November 2025
Available online 15 November 2025

LII community, notably by paving the way for future experimental and modeling works to be undertaken in order to improve our understanding of the fundamental mechanisms at play during LII and determining the underlying parameters.

1. Introduction

The past decades have been characterized by ever-growing concern over the effects of soot on human health and the environment, due notably to the cytotoxicity of combustion-generated particles. The reported adverse effects of the latter on the cardiovascular and pulmonary systems indeed make them a serious public health risk (Arden Pope III & Dockery, 2006; Lippmann, 2014; Du et al., 2016). Since soot particles absorb radiation strongly in both the visible and the near-infrared (IR) spectral regions, they are also identified as among the greatest anthropogenic contributors to radiative forcing. Of note, they also modify the albedo of snow and ice surfaces (Ramanathan & Carmichael, 2008; Bond et al., 2013), while acting as cloud condensation nuclei (Jia et al., 2021). Fundamental efforts targeting the elucidation of soot formation are therefore required in order to allow to mitigate its emission from combustion processes. For over a half-century now, major progress in the field has been reported in various reviews (see Wang (2011); Michelsen et al. (2020); Xu, Wang, & Liu (2022); Jiaqiang et al. (2022); Martin, Salamanca, & Kraft (2022), as examples). Additional work in the domain is still required, however, as highlighted by Michelsen (2017), who emphasizes the need for advanced in situ techniques allowing probing complex reacting media.

In this context, laser-induced incandescence (LII) has proven to be one of the most powerful techniques for soot characterization in flames and exhaust gases (Michelsen et al., 2015). It involves heating particles to their incandescence temperature by means of a pulsed laser source before collecting the radiation emitted above the flame emission using an adapted detector such as a photomultiplier tube or an intensified camera for time- and spatially-resolved measurement approaches, respectively. Ever since Melton (1984) showed that the intensity of the radiative emission from laser-heated soot could be considered as proportional to its volume fraction in the probed medium for detection wavelengths in the visible spectral range, the laser extinction method (LEM) calibrated LII has been extensively used for the quantitative determination of soot volume fractions in flames (Zhang, Zhou, & He, 2023). Furthermore, LII has also been combined with a variety of diagnostics, including elastic light scattering and transmission electron microscopy (TEM), to infer the size of primary particles and aggregates (Bladh et al., 2011a; Reimann, Kuhlmann, & Will, 2009; Snelling et al., 2011; Will, Schraml, & Leipertz, 1995), transmittance measurements to infer information on soot optical properties (Michelsen, Schrader, & Goulay, 2010; Yon et al., 2011) or laser-induced fluorescence (LIF) to detect both soot and its aromatic precursors by means of the so-called multiple-excitation wavelength LII-LIF approach, for example (Bejaoui, Lemaire, & Therssen, 2015; Lemaire et al., 2013). Thanks to a detailed examination of the theoretical background underlying the laser-induced incandescence phenomenon, progress has been achieved in the application of the LII technique itself as well. This includes the development of the auto-compensating approach, which enables the quantification of soot volume fractions without requiring any coupling with LEM (Snelling et al., 2005) or the development of the two-excitation wavelength LII approach to assess the relative wavelength dependence of the soot absorption function (Bejaoui et al., 2014; Yon et al., 2011).

Nevertheless, properly applying these techniques and correctly interpreting measured signals calls for an in-depth understanding of the physical mechanisms and parameters controlling the laser-induced incandescence of soot. Consequently, since the early works of Weeks & Duley (1974), Eckbreth (1977) and Melton (1984), significant effort has gone into developing theoretical models capable of predicting the radiative emission from laser-heated particles. Their predictive capabilities, however, strongly depend on the nature of the energy fluxes integrated within the energy and mass balance equations accounting for the temporal evolution of the soot temperature and diameter during the laser heating and subsequent cooling stages. In addition to the existence of wide varying sub-models aimed at representing laser absorption, heat conduction or soot sublimation, the parameterization of their governing equations also significantly differs from one study to another, thus explaining why LII models commonly used in the literature can lead to divergent predictions, as exemplified by Michelsen et al. (2007). A great deal of efforts must therefore be directed at determining the energy and mass-balance mechanisms that must be considered and how they should be formulated and parameterized, as pointed out in Michelsen et al. (2015).

In view of the foregoing, the present work aims at assessing the predictive capability of different LII model formulations against different comprehensive experimental datasets, including those provided by Goulay et al. (2013) and Bejaoui et al. (2015). It will thus help identify the potential strengths and weaknesses of particular sub-models while proposing avenues into how to parameterize them. That being said, and before detailing the contents of this research, the main progress achieved in the field of LII model development will be reviewed in section 2. This will allow to identify the most relevant models to consider within the context of this benchmarking study while highlighting the importance of various soot properties and empirical factors whose influence on simulated signals has to be clearly assessed, notably by conducting sensitivity analyses.

2. Recent progress in LII modeling

2.1. Review of LII models from the literature

Among the first attempts to model the radiation from laser-heated particles, one can cite the work by Weeks & Duley (1974), who investigated light emission from submicron carbon black particles excited by TEA CO_2 laser pulses. In this pioneering work, the authors

computed the time-dependent temperature of aerosol particles exposed to laser irradiation by means of an energy balance, including terms representing absorption of the radiative flux, radiation, as well as cooling through molecular collision with the particles. Eckbreth (1977) subsequently introduced the concept of laser-modulated incandescence (LMI) of soot, which, back then, was considered as a source of significant interference during Raman scattering measurements in flames. Time-resolved incandescence signatures were notably analyzed therein to elucidate the dominant heat transfer mechanisms at play, with a particular emphasis on the sublimation process.

Notwithstanding the above, almost all LII models currently used are derived, to a certain extent, from the one proposed by Melton (1984). In this reference work, Melton proposed an LMI model which integrates particle heating by laser absorption and cooling by conduction to the surrounding atmosphere, emission of thermal radiation, and sublimation of carbon clusters at high temperatures. Since then, radiation from laser-heated soot has been typically computed in LII modeling tools by introducing the temporal evolution of the soot temperature (T_p) and diameter (D_p) in a Planck function, with T_p and D_p being calculated by solving a couple of differential equations accounting for particle energy and mass balances during the heating and cooling stages. Actually, the main differences between existing models are related to the nature of the energy fluxes integrated within the above-mentioned balance equations, the governing equations representing these fluxes, and their parameterization. This variability notably explains why significantly diverging LII responses can be predicted as a function of the considered model formulation (see Schulz et al. (2006) or Michelsen et al. (2007) for example). This variability is, moreover, exemplified in Table A1 (see Appendix 1), which summarizes the main features of a series of LII models issued from more than 30 studies published over the last 40 years. Although this synthesis is not intended to provide an exhaustive overview of the theoretical analyses of the laser heating of carbon particles (the early works by Weeks & Duley (1974), Eckbreth (1977), Burakov et al. (1977) or Bukatyi, Sutorikhin, & Shaiduk (1983) are indeed not reported in Table A1 in a bid to focus attention on the development of simulation tools following the work by Melton (1984)), it still contributes to highlighting the recent developments which helped refine LII models and elucidate the mechanisms at play during the laser-induced incandescence of soot.

Among recent contributions in the field, one can mention the works by Snelling et al. (2000) and by Smallwood et al. (2001), who considered the effects of multiple carbon clusters evaporating from the soot surface during sublimation. These authors also compared different evaporation sub-models while evidencing the significance of parameters such as the molecular weight for solid carbon associated with the heat of evaporation and the thermal velocity of carbon vapor. Michelsen (2003) then proposed a more refined treatment of the energy- and mass-balance equations underlying the LII process by adding terms representing melting, annealing and oxidation of the soot particles, in addition to the non-thermal photodesorption of carbon clusters from the soot surface to the fluxes usually considered (i.e., particle heating by absorption and cooling by sublimation, conduction and radiation). While leading to predicted signals matching those measured in Michelsen et al. (2003), the complementary terms added by Michelsen (2003) were found to be particularly relevant when it came to properly simulating the lack of fluence dependence of the peak LII signals above the sublimation threshold. In a subsequent work aimed at estimating the values taken by the soot absorption function $E(m)$ and the thermal accommodation coefficient α_T (two fundamental factors controlling the absorption and conduction fluxes, respectively), Snelling et al. (2004) proposed an updated version of their 2000 model (Snelling et al., 2000), which considered the fractal structure of soot aggregates in the calculation of the heat conduction rate, thus accounting for the so-called shielding effect (referred to as SE in the following). The same research team then further improved their simulation tool by incorporating the Fuchs approach to calculate the heat loss rate between a heat conduction equivalent sphere accounting for the mass-fractal structure of soot aggregates and the surrounding gas in the transition regime (Liu et al., 2006a; Liu, Smallwood, & Snelling, 2005). Furthermore, the authors also reviewed the conduction sub-model formulations commonly used in the LII literature and provided an overview of the physical mechanisms involved in heat conduction loss from a single spherical particle in the entire range of the Knudsen number (Liu et al., 2006b). The importance of taking into account the variation of the thermal properties of the surrounding gas between the gas temperature and the particle temperature was notably highlighted therein. The theoretical analysis undertaken by Liu et al. (2006b) to evaluate the accuracy of various models for heat conduction in the transition regime, moreover, led the authors to strongly recommend the Fuchs approach, which they believed, ought to be considered as the 'default' heat conduction model in LII applications. In a 2007 benchmark (Michelsen et al., 2007), Michelsen proposed an updated model derived from the one introduced in Michelsen (2003). While neglecting soot melting and annealing, this new formulation integrated, in an original fashion, the saturation of the linear, single- and multi-photon absorption leading to the photodesorption of C_2 clusters at high fluences, in addition to an energy loss term representing cooling by thermionic emission, which involves the thermal ejection of electrons from heated particles. Bladh, Johnsson, & Bengtsson (2008) then led a sensitivity analysis of the impact of different factors (including the gas temperature, the pressure, the level of aggregation, the laser fluence, the detection wavelength, and the laser spatial profile) on the relationship between the LII signal and soot volume fraction. In this work, the authors considered the Fuchs approach in computing the heat loss by conduction, according to the conclusions from Liu et al. (2006b). The model formulation used by Bladh, Johnsson, & Bengtsson (2008) (derived from the one previously developed in Bladh & Bengtsson (2004)), moreover, took soot size and spatial energy distributions into account. The authors proceeded by implementing a linear combination routine, where the balance equations and the LII response were computed for a discrete number of values of the initial diameter and laser fluence before being combined to derive a time-resolved signal representative of those measured in the case of polydisperse size distributions and non-uniform laser profiles. This modeling approach, which was subsequently used in Bladh, Johnsson, & Bengtsson (2009), was shown to be quite valuable in assessing the influence of the spatial distribution of laser energy on the estimation of soot size by time-resolved LII (TiRe-LII) measurements. Meanwhile, a theoretical analysis focusing on sub-models of the change in enthalpy during sublimation, conduction and oxidation was proposed by Michelsen et al. (2008). In addition to expressing the conductive cooling rate in terms of enthalpy instead of energy to account for expansion, this study also demonstrates the sensible effect oxidation can have on the time decays of simulated LII signals. Updated parameterizations

for average enthalpies of formation, molecular weights and total pressures of sublimed carbon clusters for use in LII models were, moreover, provided. In a subsequent work, Michelsen (2009) also proposed a temperature-dependent expression of the accommodation coefficient, which drives cooling by conduction, based on a compilation of data on the temperature dependence of translational, rotational, and vibrational energy transfer for diatomic molecules colliding with graphite surfaces.

Regarding the latest progress in LII modeling, one can cite the development of an updated thermionic emission sub-model by Mitrani et al. (2016), which takes into account the increased barrier to further electron emission due to a positive charge buildup. Of note also is the development of an open-source software application aimed at processing/analyzing LII signals and visualizing/comparing measured and simulated results (Mansmann et al., 2018). Although representing a major contribution to the field, with great potential to help the LII community in evaluating and comparing data obtained by various research groups, this powerful tool currently only considers relatively standard model formulations which do not integrate photolytic processes such as multi-photon absorption or carbon cluster photodesorption (Michelsen, 2003; Michelsen et al., 2007). The importance of integrating these mechanisms in order to reproduce LII signals over a wide range of excitation conditions was, however, illustrated in the framework of an inverse technique-based analysis of standard and refined LII models (Lemaire & Mobtil, 2015), which concluded that further developments on the matter was still required. In a recent analysis aimed at inferring thermal accommodation coefficient values from LII measurements performed in a turbulent flame of Diesel, Menanteau & Lemaire (2020) analyzed the influence of the aggregate size and the formulation of the conduction sub-model on signals simulated by means of a comprehensive model built upon expressions representing soot heating by absorption, annealing, and oxidation as well as cooling by radiation, sublimation, conduction, and thermionic emission. Predictions merging on a single curve with measured data were then obtained. This work, however, also showed that the good ability of refined models to properly simulate LII signals increased their relative complexity, due particularly to the number of input parameters and empirical factors needing to be properly set as a function of the considered operating conditions (e.g., excitation wavelength (EW), soot maturity level, etc.). This observation motivated the authors to conduct a series of works aimed at parameterizing refined LII model formulations against a comprehensive set of experimental data issued from the analysis of the above-mentioned Diesel flame (Lemaire & Menanteau, 2021, 2023a; Menanteau & Lemaire, 2022). In addition to implementing an advanced optimization procedure coupling design of experiments (DoE) with a genetic algorithm-based solver to infer the values taken by different parameters whose values were barely available in the literature for EWs of 266, 355 or 1064 nm (e.g., multiphoton absorption cross-sections for C_2 photodesorption ($\sigma_{\lambda n}$), saturation coefficients for linear and multiphoton absorption ($B_{\lambda 1}$ and $B_{\lambda n}$), enthalpy required to photodesorb carbon clusters ($\Delta H_{\lambda n}$), etc.), Lemaire & Menanteau also proposed a model formulation integrating for the first time the generalized structure factor from Yon et al. (2014, 2015) to account for the scattering behavior of fractal aggregates. In doing so, LII signals measured with EWs of 266, 355, 532 and 1064 nm were correctly simulated in the low-to-intermediate fluence regime, providing information on the impact of multiple scattering, soot maturation and the wavelength on the evolution of soot absorption function values (Lemaire & Menanteau, 2023a).

To conclude, and notwithstanding the good agreement between measured and predicted LII signals in different studies (see Michelsen (2003), Snelling et al. (2004), Hofmann et al. (2008), Hadef et al. (2010, 2013), López-Yglesias, Schrader, & Michelsen (2014), and Lemaire & Menanteau (2023a) for instance), simulation results diverging more or less significantly from their experimental counterparts were alternatively reported, depending on the model formulation considered and on its parameterization (Bejaoui et al., 2015; Betrancourt et al., 2017; Lemaire & Mobtil, 2015; Mansmann et al., 2018; Menanteau & Lemaire, 2022). This observation particularly illustrates that despite the significant progress that has been made in refining LII modeling tools, their predictive character still depends on numerous factors, including the nature of the energy fluxes considered in the energy and mass balance equations, as mentioned above, as well as on the formulation and parameterization of the sub-models accounting for these fluxes, whether or not the behavior and properties of fractal aggregates are taken into account, the nature of the investigated medium, the selected operating conditions (wavelength and fluence range, among others), etc. Furthermore, it is rather difficult to distinguish whether the discrepancies sometimes observed between measured and simulated data are dependent on the specific experiment or on the implemented models since most LII modeling studies (with the exception of those by Mansmann et al. (2018) and Lemaire & Menanteau (2021) and (2023a)) consider a more or less customized model to simulate just one dataset, without verifying the validity of the implemented model against theoretical and/or measured results from other studies. Properly assessing the predictive capability of current LII modeling tools therefore prompts the need for systematic comparisons between signals predicted with different models and various datasets from the literature, which is the core of the present paper. As a consequence, and before detailing the work which has been carried out as part of this research, section 2.2 will review the few comparison studies and benchmarks of LII models that have been undertaken to date.

2.2. Benchmarks of LII models

A description of the sub-models commonly used in LII modeling, together with a presentation of their governing equations can be found in Michelsen et al. (2015). The assessment of the predictive capability of current LII models was, however, out of the scope of this general review. As far as benchmarks are concerned, one can first refer to the above-cited work by Smallwood et al. (2001). Different sublimation sub-models were indeed tested therein to obtain simulated signals, which were notably compared with data measured by Ni et al. (1995). Liu et al. (2006b) then thoroughly reviewed the sub-model formations used to represent conduction in LII while investigating the influence of various parameters, such as the pressure and the temperature, on obtained predictions. No comparison with experimental data was, however, done in Liu et al. (2006b). Furthermore, the focus in these studies was solely on specific sub-models (sublimation in Smallwood et al. (2001) and conduction in Liu et al. (2006b)). Actually, the first comprehensive benchmark of LII models was proposed in Schulz et al. (2006), where predictions from nine models were compared. As highlights, the paper

showed that signals calculated with different models spanned several orders of magnitude, with major variations in signal decay rates at low fluence and in both rise and decay times at high fluence. The most exhaustive benchmark to date is still the one proposed by Michelsen et al. (2007). The results from a fully constrained model implemented by 10 research groups were first compared in this study. LII signals calculated while considering the same set of equations and input parameters were then shown to converge, thus evidencing the consistency in the way simulated signals were computed by the different teams while ensuring that similar treatments of mechanisms gave similar answers. As such, this exercise allowed highlighting the fact that the discrepancies between the predictions from the various models from the literature were apparently not related to implementation issues and/or problems in terms of calculation approaches (a point raised in the wake of the benchmark from Schulz et al. (2006)). Besides, predictions from ten unconstrained models were also compared, and showed a considerable variability in obtained results. This variability was attributed, among other things, to the range of values selected for important input parameters (e.g., $E(m)$ and α_T) at low fluence and to the differences in the treatment of heat and mass loss by sublimation at high fluence. Although the work from Michelsen et al. (2007) was highly valuable when it came to identifying the most important differences between tested models while highlighting the aspects of the physical description of the LII phenomenon that led to the greatest uncertainties in signal prediction and analysis, no comparison with experimental databases was, however, proposed, thus removing the predictive capability of the considered models to be assessed. To address this issue, some case studies were undertaken by Lemaire & Mobtil (2015) and Bejaoui et al. (2015), among others. Signals measured in atmospheric flames were notably compared in these works with predictions from standard and refined models derived from the formulations proposed by Melton (1984), Michelsen (2003) and Michelsen et al. (2007). Only two models and one experimental dataset were nonetheless considered in both these studies. Furthermore, and although the paper from Lemaire & Mobtil (2015) provided brief sensitivity analyses of $E(m)$ and α_T values, the impact of other crucial parameters driving the absorption and sublimation fluxes, including $\sigma_{\lambda n}$, $B_{\lambda 1}$, $B_{\lambda n}$ and $\Delta H_{\lambda n}$, was not assessed, thus limiting the scope of this specific work.

In accordance with the conclusions from previous benchmarks (Michelsen et al., 2007; Schulz et al., 2006), the above survey of the literature confirmed that given the large differences between the results from different LII modeling tools, considerable work still needs to be done to compare wide varying model formulations, in order to perform detailed sensitivity analyses focusing on parameters known to significantly influence the LII response while assessing the predictive capability of each tested model against detailed experimental data. Within this context, the present work, which follows recent preliminary analyses (Lemaire & Menanteau, 2023b, 2024), sets out to compare the ability of four commonly implemented LII models drawn from the literature to simulate results obtained from various comprehensive datasets notably composed of signals measured in an ethylene diffusion flame (Goulay et al., 2013) and in a $CH_4/O_2/N_2$ premixed one (Bejaoui et al., 2015). To that end, two relatively standard model formulations, referred to as models 1 and 2, are first considered. They are drawn from Melton (1984) for model 1 and Hofmann, Kock, & Schulz (2007) for model 2, and integrate mechanisms representing heating by absorption of the laser energy and cooling by radiation, sublimation and conduction. Supported by the conclusions from Lemaire & Mobtil (2015), which showed the importance of integrating additional mechanisms, such as photolytic ones, two refined models issued from Michelsen (2003) and Michelsen et al. (2007) are also considered. The first one (referred to as model 3) integrates the above-listed energy fluxes with terms representing soot annealing and oxidation (Michelsen, 2003). The second one (referred to as model 4) neglects annealing, but includes terms standing for saturation of linear, single- and multi-photon absorption processes and cooling by thermionic emission (Michelsen et al., 2007). In addition to systematically comparing predictions from these four simulation tools with the signals from Goulay et al. (2013) and Bejaoui et al. (2015), sensitivity analyses focusing on key parameters influencing the LII response (e.g., soot absorption function, thermal accommodation coefficients, etc.) will be carried out. Given that parameterizing refined models is, moreover, far from trivial, as exemplified in Bejaoui et al. (2015), where factors proposed by Michelsen (2003) for an EW of 532 nm were used to simulate signals collected using a laser source functioning at 1064 nm, detailed sensitivity analyses focusing on $\sigma_{\lambda n}$, $B_{\lambda 1}$, $B_{\lambda n}$ and $\Delta H_{\lambda n}$, among others, will be provided as well. This should enable a better understanding of the influence of these parameters on computed LII responses, noting that this is the first time, to the best of the authors' knowledge, that a comprehensive analysis focusing on the impact of all these input parameters is proposed within a same work. Conclusions will then be drawn, although it should be noted that the aim of this paper is not to state that some models should be preferred over others. Furthermore, this study does not intend to provide a series of parameters that should be imperatively selected for the correct simulation of LII signals. Rather, it aims at identifying the potential strengths of particular models and sub-models, depending on the targeted applications, while proposing insights into how to parameterize them, given the relative impact of each input property and/or factor, and considering the related range of plausible values, as identified in the literature, depending on the investigated reacting media and operating conditions. Within this context, and in addition to the above-mentioned sensitivity analyses, basic optimization calculations will also be proposed to infer the values that must be set for some parameters in order to minimize the deviation between measured and simulated signals. Reiterating that the objective here is not to provide turnkey model formulations integrating time-tested must-use parameter sets, one should thus note that these calculations only aim at helping to get an overview of the impact of these factors on the LII responses. Furthermore, and since some soot properties and/or physical factors embedded within the equations composing the energy- and mass-balance equations underlying the LII process are already relatively well documented in the literature, the focus will be solely on soot properties (e.g., the absorption function) and thermal/photolytic parameters (e.g., the thermal accommodation coefficient, cross-section for the removal of C_2 clusters by photodesorption, saturation coefficient for multi-photon absorption, etc.), which are subject to large uncertainties and/or for which data are quite rare, if not inexistent, depending on the considered excitation wavelength. As such, this benchmark should be useful to the LII community by providing basic guidelines aimed at aiding the selection and implementation of suitable simulation tools for the analysis and characterization of in-flame generated soot.

3. Experimental databases

For the purposes of the present comparison work, we first considered the dataset for LII model validation proposed by Goulay et al. (2013). The latter provides spectrally and temporally resolved signals measured in an atmospheric co-flow ethylene diffusion flame stabilized on a Santoro burner. To that end, soot was irradiated with both the 1064- and 532-nm output from an injection-seeded Nd:YAG laser producing spatially homogeneous beams, and pulses with a smooth temporal profile (spatial beam profiles and laser temporal profiles being provided at both 532 and 1064 nm in Goulay et al. (2013)). Time-resolved LII signals were recorded with fluences ranging from 0.01 to 3.5 J cm^{-2} using a fast-gated photomultiplier tube (rise time shorter than 800 ps) with a bandpass filter centered at 681.8 nm (10.0-nm bandwidth). Time-resolved emission spectra were used to identify and avoid spectral interferences and to infer soot temperatures over the entire LII signal evolution by fitting a Planck function to collected spectra, noting that soot temperature profiles were also obtained by means of three-color time-resolved LII measurements. Data were recorded at 50 mm height above the burner (HAB) in the annular high-soot region at the edge of the flame, where fits to flame luminosity yielded a temperature value of 1676 ± 40 K. According to previously reported transmission electron microscopy (TEM) data from Dobbins & Megaridis (1987), Megaridis & Dobbins (1989), Puri et al. (1993), and Vander Wal, Ticich, & Stephens (1999), soot is expected to have a primary particle size of 33 nm and an aggregate size of ~135 nm at this specific HAB. The reader is referred to Goulay et al. (2013) for more information on the experimental setup used and the measurement procedure implemented.

The second database considered was derived from Bejaoui et al. (2015). It includes a series of LII time decays collected using a photomultiplier tube having a rise time of 2 ns at different HAB in an atmospheric $CH_4/O_2/N_2$ premixed flat flame stabilized on a McKenna burner. Signals were measured using a 1064-nm nearly top-hat laser beam and a detection wavelength of 610 nm (full width at half maximum (FWHM) of 20 nm), with laser fluences between 0.03 and 0.56 J cm^{-2}. In addition to providing the spatial and temporal profiles of the laser beam energy, this thorough experimental effort also reports averaged temperatures of soot over a 10-ns period shortly after the peak of the laser pulse estimated based on an analysis of spectrally-resolved LII radiation collected in a spectral range of 500-630-nm. Flame gas temperatures were, moreover, measured using NO-laser-induced fluorescence thermometry, while information regarding primary particle and aggregate sizes were assessed by transmission electron microscopy. Signals measured at two specific HAB (9 and 15 mm) in the $CH_4/O_2/N_2$ flame were considered herein in order to cover different soot maturation stages. Mean aggregate size (i.e., the number of particles per aggregate) and primary particle diameter of 2.3 and 11.5 nm at 9 mm HAB versus 9.6 and 12.4 nm at 15 mm HAB were especially assessed at these locations for which flame temperatures of 1835 ± 100 K and 1542 ± 100 K were estimated.

Of note, three additional datasets were considered in section 5.3.2 to provide some perspectives regarding the development and the predictive capability of comprehensive LII modeling tools operating under widely varying conditions. These consist of the experimental results collected by Lemaire et al. in an atmospheric turbulent spray flame of Diesel (Bejaoui, Lemaire, & Therssen, 2015; Lemaire, Bejaoui, & Therssen, 2013; Lemaire & Menanteau, 2021, 2023a) using EWs of 532 and 1064 nm in addition to the LII decay times measured with an EW of 1064 nm by Mi et al. (2021) and Zheng et al. (2023) in laminar premixed ethylene/air flames at pressure ranging from 1 to 10 bar and in a jet-A flame stabilized in a pressurized combustor functioning at a pressure of between 1 and 3.8 bar, respectively. These complementary databases were especially considered in the final analysis proposed in section 5.3.2, since they allow to simulate data collected within both laminar/turbulent and atmospheric/high-pressure flames, noting that the information required to simulate obtained signals, including the laser profiles, the particle size (issued from TEM images), etc., is fully provided in the above-cited references.

Note, to conclude, that even though LII measurements are generally performed using laser fluences significantly lower than the upper values considered in the above-described datasets (especially when it comes to assessing the soot size through TiRe-LII (a point notably discussed in section 5.1.3)), we still considered the whole range of operating conditions reported in the works by Goulay et al. (2013), Bejaoui et al. (2015) or Lemaire & Menanteau (2021, 2023a) in the following. The aim was, indeed, to rule on the predictive ability of the different LII models tested in section 5 over an extended range of laser fluences, further noting that doing so can also be of high interest in elucidating the detailed heat and mass transfer processes involved during the laser heating of soot particles above the sublimation threshold.

4. LII signal modeling

4.1. Governing equations used for the implementation of each model

The core of each implemented model is based on the following system of coupled differential equations depicting the variations of the internal energy rate (dU_{int}/dt) and mass (dM_p/dt) of soot particles as a function of time (t):

$$\begin{cases} \dfrac{dU_{int}}{dt} = \dot{Q}_{abs} - \dot{Q}_{sub} - \dot{Q}_{cond} - \dot{Q}_{rad} + \dot{Q}_{ann} + \dot{Q}_{ox} - \dot{Q}_{th} \\ \dfrac{dM_p}{dt} = \sum_{j=1}^{j_{tot}} \left(\dfrac{dM_p}{dt}\right)_{sub,j} + \left(\dfrac{dM_p}{dt}\right)_{ox} \end{cases} \quad (1)$$

where $\dot{Q}_{abs}$ stands for the rate of energy gained by absorption of the laser energy, $\dot{Q}_{ann}$ and $\dot{Q}_{ox}$ depict the rates of energy production by soot annealing and oxidation, respectively, $\dot{Q}_{rad}$, $\dot{Q}_{th}$, $\dot{Q}_{sub}$ and $\dot{Q}_{cond}$ represent the rates of energy loss by radiation, thermionic

emission, sublimation and conduction, while subscripts 'sub' and 'ox' respectively denote the contributions of the sublimation and oxidation mechanisms to the mass loss, 'j' stands for the contribution of each vaporized carbon cluster C_j to the particle mass loss and j_{tot} corresponds to the total number of vaporized carbon clusters. Of course, and depending on the considered model formulation, the nature of the energy fluxes considered or neglected and their related governing equations significantly diverge, as will be illustrated in the following sections. As for the primary particle mass M_p, it is expressed as a function of the diameter D_p as follows:

$$M_p = \frac{\pi \cdot {D_p}^3}{6} \Big/ \left(\frac{1 - X_a}{\rho_s} + \frac{X_a}{\rho_a} \right) \tag{2}$$

where X_a represents the soot annealed fraction (set to 0 in the models in which annealing is neglected), while ρ_s and ρ_a are the density of the unannealed (denoted with a subscript 's' in the following) and annealed (denoted with a subscript 'a') soot fractions, respectively. One should finally note that although the expressions accounting for the different terms integrated in Eq. (1) depend on the spatial domain *(x,y)* delimited by the dimensions of the laser beams, the time *t* and the number N_p of primary particles contained in soot aggregates, for clarity, the actual identification of this dependence through a "$(x,y,t,\ N_p)$" notation will not be realized.

4.1.1. Internal energy

Models 1, 3 and 4 use Eq. (3) to express the rate of change of energy stored by soot:

$$\frac{dU_{int}}{dt} = N_p \cdot \frac{\pi}{6} {D_p}^3 \cdot \left[\rho_s \cdot c_s \cdot (1 - X_a) + \rho_a \cdot c_a \cdot X_a \right] \cdot \frac{d\,T_p}{dt} \tag{3}$$

where T_p represents the particle temperature, while c_s and c_a stand for the heat capacity of the unannealed and annealed soot fractions, respectively, noting that X_a is set to 0 in models 1 and 4. As for model 2, it also neglects annealing, but alternatively uses Eq. (4) to represent the particle energy variation rate:

$$\frac{dU_{int}}{dt} = \frac{d}{dt}\left(N_p \cdot M_p \cdot c_s \cdot T_p \right) = N_p \cdot \left(M_p \cdot c_s + M_p \cdot T_p \cdot \frac{dc_s}{d\,T_p} \right) \cdot \frac{d\,T_p}{dt} + N_p \cdot c_s \cdot T_p \cdot \frac{dM_p}{dt} \tag{4}$$

Although the use of Eq. (4) has been subject to debate in the LII community (Liu & Snelling, 2007; Michelsen et al., 2008), we still considered this expression in implementing model 2 exactly as originally proposed in Hofmann, Kock, & Schulz (2007). In addition, a discussion, along with a sensitivity analysis dealing with the formulation of this term, will be proposed in section 5.1.1. Regarding soot properties, constant or temperature-dependent expressions of ρ_s and c_s are considered as a function of the selected model. More specifically, the soot density and heat capacity are set to 2.26 g cm^{-3} and 1.9 J g^{-1}·K^{-1} in model 1. Alternatively, model 2 considers a value of 1.86 g cm^{-3} for ρ_s, while c_s is expressed as a function of T_p as follows:

$$c_s = 1.878 + 1.082 \times 10^{-4} \cdot T_p - 1.5149 \times 10^5 / {T_p}^2 \tag{5}$$

Finally, models 3 and 4 compute ρ_s and c_s based on Eqs. (6) and (7), respectively:

$$\rho_s = 2.3031 - 7.3106 \times 10^{-5} \cdot T_p \tag{6}$$

$$c_s = \frac{R}{12.01} \cdot \left\{ 1.115 \left(\frac{597}{T_p} \right)^2 \cdot exp\left(\frac{597}{T_p} \right) \cdot \left[exp\left(\frac{597}{T_p} \right) - 1 \right]^{-2} + 1.789 \cdot \left(\frac{1739}{T_p} \right)^2 \cdot exp\left(\frac{1739}{T_p} \right) \cdot \left[exp\left(\frac{1739}{T_p} \right) - 1 \right]^{-2} + \frac{T_p}{8620} \right\} \tag{7}$$

noting that model 3 additionally requires to define the density of the annealed soot fraction, which is calculated based on Eq. (8), while c_a is considered equal to c_s (Michelsen, 2003).

$$\rho_a = 2.6 - 1.0 \times 10^{-4} \cdot T_p \tag{8}$$

4.1.2. Absorption

Each tested model is based on the Rayleigh-Debye-Gans approximation applied to fractal aggregates, which considers that the light absorption of soot aggregates corresponds to the product of the absorption cross-section of a single primary particle by the number N_p of individual primary particles composing the aggregates. Based on this, the rate of energy change by absorption of the laser pulse is expressed in models 1 to 3 following Eq. (9):

$$\dot{Q}_{abs} = N_p \cdot \left[C_{abs,s} + C_{abs,a} \right] \cdot \frac{F \cdot q_{exp}(t)}{\int_0^{t_l} q_{exp}(t) dt} \tag{9}$$

with q_{exp}, t_l and F respectively denoting the normalized laser irradiance, the pulse duration and the pulse energy density. As for $C_{abs,s}$ and $C_{abs,a}$, they represent the absorption cross-section of unannealed and annealed soot fractions, respectively, so that:

$$C_{abs,s} = (1 - X_a) \cdot \frac{\pi^2 \cdot {D_p}^3}{\lambda_l} \cdot E(m) \tag{10}$$

and

$$C_{\mathrm{abs,a}} = X_{\mathrm{a}} \cdot \frac{\pi^2 \cdot {D_{\mathrm{p}}}^3}{\lambda_{\mathrm{l}}} \cdot f_{\mathrm{a}} \cdot E_{\mathrm{a}}(m) \tag{11}$$

with λ_{l} being the excitation wavelength, f_{a} an absorption empirical scaling factor related to annealed soot while $E(m)$ and $E_{\mathrm{a}}(m)$ stand for the refractive index functions of unannealed and annealed soot. Of note, the subscript 's' is intentionally omitted for unannealed soot to allow consistency with the formalism generally adopted in the literature. Regarding model 4, it expresses the absorption rates considering the saturation of linear, single-photon and multi-photon absorption processes following Eq. (12):

$$\dot{Q}_{\mathrm{abs}} = N_{\mathrm{p}} \cdot C_{\mathrm{abs,s}} \cdot \frac{f_1 \cdot B_{\lambda 1}}{\int_0^{t_{\mathrm{l}}} q_{\mathrm{exp}}(t)dt} \cdot \left\{ 1 - exp\left[-\frac{F \cdot q_{\mathrm{exp}}(t)}{B_{\lambda 1}} \right] \right\} + N_{\mathrm{p}} \cdot k_{\lambda \mathrm{n}} \tag{12}$$

where f_1 is an empirical scaling factor for linear absorption, $B_{\lambda 1}$ corresponds to an empirical saturation factor related to single-photon absorption, while $k_{\lambda \mathrm{n}}$ is a rate constant for removal of C_2 clusters by nonthermal photodesorption defined as follows:

$$k_{\lambda \mathrm{n}} = \sigma_{\lambda \mathrm{n}} \cdot \frac{\pi \cdot {D_{\mathrm{p}}}^3 \cdot N_{\mathrm{ss}}}{6} \cdot \frac{B_{\lambda \mathrm{n}}^n}{\int_0^{t_{\mathrm{l}}} \left(q_{\mathrm{exp}}(t) \right)^n \mathrm{d}t} \cdot \left\{ 1 - exp\left[-\left(\frac{F \cdot q_{\mathrm{exp}}(t)}{B_{\lambda \mathrm{n}}} \right)^n \right] \right\} \tag{13}$$

where $\sigma_{\lambda \mathrm{n}}$ is defined in the work by Michelsen as a cross-section for removal of C_2 clusters by photodesorption (see Michelsen et al. (2007)), n represents the number of photons to be absorbed to photodesorb C_2 clusters , N_{ss} stands for the density of carbon atoms at the soot surface, and $B_{\lambda \mathrm{n}}$ is an empirical saturation factor related to multi-photon absorption process.

4.1.3. Sublimation

The evaporative cooling rate in the two standard models tested herein is expressed based on the following equation:

$$\dot{Q}_{\mathrm{sub}} = N_{\mathrm{p}} \cdot \frac{-\Delta H_{\mathrm{v}}}{\omega_{\mathrm{v}}} \cdot \frac{\mathrm{d}M_{\mathrm{p}}}{\mathrm{d}t} \tag{14}$$

where ΔH_{v} represents the enthalpy of formation of sublimed carbon clusters and ω_{v} denotes their molecular weight. Model 1 assumes that sublimation only generates C_3 clusters and considers constant values for ΔH_{v} (7.78×10^5 J mol^{-1}) and ω_{v} (36 g mol^{-1}). On the other hand, and although Hofmann, Kock, & Schulz (2007) consider that the dominant species generated by sublimation above ~2000 K is C_3, model 2 still computes the sublimation flux by taking into account C_1 to C_7 clusters, which can be present in different concentrations in the vapor phase. Their molecular weight and enthalpy of vaporization are computed as a function of the particle temperature based on polynomial fits to data from Leider, Krikorian, & Young (1973) (see details in Hofmann, Kock, & Schulz (2007)). As far as the mass lost through sublimation is concerned, it is calculated in models 1 and 2 using Eqs. (15) and (16), respectively:

$$\frac{\mathrm{d}M_p}{\mathrm{d}t} = -\frac{\pi \cdot {D_{\mathrm{p}}}^2 \cdot w_{\mathrm{v}} \cdot \alpha_{\mathrm{M}} \cdot p_{\mathrm{v}}}{R_p \cdot T_{\mathrm{p}}} \cdot \sqrt{\frac{R_m \cdot T_{\mathrm{p}}}{2 \cdot w_{\mathrm{v}}}} \tag{15}$$

$$\frac{\mathrm{d}M_{\mathrm{p}}}{\mathrm{d}t} = -\frac{\pi \cdot {D_{\mathrm{p}}}^2 \cdot w_{\mathrm{v}} \cdot \alpha_{\mathrm{M}} \cdot p_{\mathrm{v}}}{R_p \cdot T_{\mathrm{p}}} \cdot \sqrt{\frac{R_m \cdot T_{\mathrm{p}}}{2 \cdot w_{\mathrm{v}}}} \cdot \frac{f \cdot k_p \cdot T_{\mathrm{p}}}{\sqrt{2} \cdot \overline{\sigma} \cdot p_g \cdot D_{\mathrm{p}} \cdot \alpha_{\mathrm{M}} + f \cdot k_p \cdot T_{\mathrm{p}}} \tag{16}$$

where α_{M} is the mass accommodation coefficient of vaporized carbon clusters, R_p and R_m are the universal gas constants expressed in effective pressure and mass units, k_p is the Boltzmann constant, $\overline{\sigma}$ stands for the average molecular cross-section for subliming species, p_g represents the ambient pressure and f denotes the dimensionless Eucken correction to the thermal conductivity of polyatomic gas. Note that the value of the mass accommodation coefficient can be comprised between 0 and 1 to account for the relative efficiency of the evaporation. It is notably mentioned in Hofmann, Kock, & Schulz (2007) that this factor is usually set to 1, as was the case in Melton (1984). We still considered a default value of 0.8 to be consistent with the α_{M} selected in a large number of LII modeling studies (Snelling et al., 2000; Bladh & Bengtsson, 2004; Michelsen et al., 2007; Bladh, Johnsson, & Bengtsson, 2008; Lemaire & Mobtil, 2015, etc.), further noting that a sensitivity analysis focusing on this specific parameter will be proposed in section 5.1.2. Finally, p_{v} represents the partial pressure of the sublimed carbon species, which is determined according to Eqs. (17) and (18) for models 1 and 2, respectively:

$$p_{\mathrm{v}} = exp\left[\frac{-\Delta H_{\mathrm{v}}}{R} \cdot \left(\frac{1}{T_{\mathrm{p}}} - \frac{1}{3915} \right) \right] \tag{17}$$

$$p_{\mathrm{v}} = exp\left(-122.96 + 9.0558 \times 10^{-2} \cdot T_{\mathrm{p}} - 2.7637 \times 10^{-5} \cdot T_{\mathrm{p}}^2 + 4.1754 \times 10^{-9} \cdot T_{\mathrm{p}}^3 - 2.4875 \times 10^{-13} \cdot T_{\mathrm{p}}^4 \right) \tag{18}$$

with R denoting the universal gas constant expressed in standard unit.

For models 3 and 4, they integrate a more refined treatment of the evaporative cooling rate, which can be presented in equation form as follows:

$$\dot{Q}_{\mathrm{sub}} = -N_{\mathrm{p}} \cdot \sum_{j=1}^{j_{\mathrm{tot}}} \frac{1}{w_j} \cdot \left(\frac{\mathrm{d}M_{\mathrm{p}}}{\mathrm{d}t}\right)_{\mathrm{sub},j} \cdot \left[\frac{\Delta H_j \cdot \left(P_{\mathrm{sat}}^{C_j} - P_{\lambda \mathrm{s}} - P_{\mathrm{diss}} - P_{\lambda \mathrm{a}}\right) + \Delta H_{\lambda \mathrm{s}} \cdot P_{\lambda \mathrm{s}} + \Delta H_{\mathrm{diss}} \cdot P_{\mathrm{diss}} + \Delta H_{\lambda \mathrm{a}} \cdot P_{\lambda \mathrm{a}}}{P_{\mathrm{sat}}^{C_j}}\right] \tag{19}$$

where w_j ($12.011 \times \mathrm{j\ g{\cdot}mol^{-1}}$) and ΔH_j stand for the molecular weight and enthalpy of formation of each C_j cluster (with j_{tot} set to 10 and 5 for models 3 and 4, respectively), $P_{\mathrm{sat}}^{C_j}$ refers to the partial saturation pressure of vaporized clusters C_j, P_{diss} is the effective pressure issued from the rate of thermal photodesorption from annealed soot, $\Delta H_{\lambda \mathrm{s}}$ and $\Delta H_{\lambda \mathrm{a}}$ are the energies required to photodesorb C_j clusters from the unannealed and annealed soot fractions, and ΔH_{diss} is the enthalpy of formation of C_j clusters by thermal sublimation of annealed soot. As for $P_{\lambda \mathrm{s}}$ and $P_{\lambda \mathrm{a}}$ which are expressed following Eq. (20), they represent the effective pressures calculated based on the rate constant for removal of carbon clusters by nonthermal photodesorption (denoted $k_{\lambda \mathrm{i}}$) from the annealed (i = a) and unannealed (i = s) soot fractions:

$$P_{\lambda \mathrm{i}} = \frac{k_p \cdot T_{\mathrm{p}}}{\pi \cdot {D_{\mathrm{p}}}^2 \cdot \alpha_j \cdot U_j} \cdot k_{\lambda \mathrm{i}} \tag{20}$$

where α_j is the mass accommodation coefficient of the vaporized species C_j (parameterized as detailed in Michelsen (2003) and Michelsen et al. (2007)), while U_j corresponds to the ejection speed of C_j away from the particle surface (see Michelsen (2003) for information on the calculation procedure of this term). Of note, $k_{\lambda \mathrm{s}}$ and $k_{\lambda \mathrm{a}}$ in model 3 are calculated using Eqs. (21) and (22), respectively:

$$k_{\lambda \mathrm{s}} = \sigma_{\lambda \mathrm{s}} \cdot \frac{\pi \cdot {D_{\mathrm{p}}}^3 \cdot N_{\mathrm{ss}} \cdot (1 - X_{\mathrm{a}})}{6} \cdot \left[1 - exp\left(-B_{\lambda \mathrm{s}} \cdot F^n \cdot q_{\mathrm{exp}}(t)^n\right)\right] \tag{21}$$

$$k_{\lambda \mathrm{a}} = \sigma_{\lambda \mathrm{a}} \cdot \frac{\pi \cdot {D_{\mathrm{p}}}^3 \cdot N_{\mathrm{sa}} \cdot X_{\mathrm{a}}}{6} \cdot \left[1 - exp\left(-B_{\lambda \mathrm{a}} \cdot F^n \cdot q_{\mathrm{exp}}(t)^n\right)\right] \tag{22}$$

where N_{sa} stands for the density of carbon atoms at the annealed soot surface, $B_{\lambda \mathrm{s}}$ and $B_{\lambda \mathrm{a}}$ correspond to empirical saturation factors related to the removal of carbon clusters from the unannealed and annealed particles by photodesorption, while the terms $\sigma_{\lambda \mathrm{s}}$ and $\sigma_{\lambda \mathrm{a}}$ are defined based on the nomenclature proposed in Michelsen (2003) as cross-sections for the photodesorption of carbon clusters (C_1 to C_3 when i = s and C_2 when i = a) of unannealed and annealed soot, respectively. Note also that $k_{\lambda \mathrm{n}}$ (defined as per Eq. (13)) is used in model 4 instead of $k_{\lambda \mathrm{s}}$. It does not take into account the annealing process, however. Finally, models 3 and 4 compute the mass lost by sublimation independently for each C_j species following Eq. (23):

$$\left(\frac{\mathrm{d}M_p}{\mathrm{d}t}\right)_{\mathrm{sub},j} = \frac{-\pi \cdot {D_{\mathrm{p}}}^2 \cdot w_j \cdot \alpha_j}{R_p \cdot T_{\mathrm{p}}} \cdot U_j \cdot B_j \tag{23}$$

where B_j is a parameter representing the influence of diffusive and convective mass and heat transfers during sublimation (Michelsen, 2003).

4.1.4. Radiation

The radiative emission from laser-heated soot is calculated in each model by integrating the Planck function over the wavelength while considering the reabsorption of background emission as done by Charwath, Michelsen or Will in Michelsen et al. (2007):

$$\dot{Q}_{\mathrm{rad}} = 8 \cdot \pi \cdot h \cdot c^2 \cdot N_{\mathrm{p}} \cdot \int_0^{\lambda_\infty} \frac{C_{\mathrm{abs,s}} + C_{\mathrm{abs,a}}}{\lambda^5} \cdot \left[\frac{1}{exp\left(h \cdot c/\lambda \cdot k_{\mathrm{B}} \cdot T_{\mathrm{p}}\right) - 1} - \frac{1}{exp\left(h \cdot c/\lambda \cdot k_{\mathrm{B}} \cdot T_{\mathrm{g}}\right) - 1}\right] \mathrm{d}\lambda \tag{24}$$

where h is the Planck constant, c stands for the speed of light, while k_B represents the Boltzmann constant.

4.1.5. Conduction

According to Liu et al. (2006b), heat conduction between soot particles and the surrounding gases is expected to occur in the free molecular regime during LII experiments conducted in flames at atmospheric pressure, as is the case herein. This statement is, moreover, corroborated by the fact the Knudsen numbers calculated based on the equations provided in Liu et al. (2006b), while integrating the parameters (particle size, thermal conductivity and heat capacity of the surrounding gases, ambient pressure and temperature) related to the experimental conditions investigated in Goulay et al. (2013) and Bejaoui et al. (2015), are significantly higher than 10 regardless of the flame locations for which LII signals are simulated in the present work. In this context, the rate of energy loss by conduction can be calculated using Eq. (25), which is especially embedded within each tested model formulation:

$$\dot{Q}_{\mathrm{cond}} = N_{\mathrm{p}} \cdot \frac{\pi \cdot D_{\mathrm{p}}^2 \cdot p_{\mathrm{g}}}{R_p \cdot T_{\mathrm{g}}} \cdot \alpha_{\mathrm{T}} \cdot \sqrt{\frac{R_m \cdot T_{\mathrm{g}}}{2 \cdot \pi \cdot \omega_{\mathrm{a}}}} \cdot \left(C_p - \frac{R}{2}\right) \cdot \left(T_{\mathrm{p}} - T_{\mathrm{g}}\right) \tag{25}$$

where T_{g} stands for the temperature of the surrounding gaseous species, ω_{a} denotes the average molecular weight of air considered as a surrogate for flame gases, and C_p is the molar heat capacity of the ambient gases at constant pressure, which is expressed as a function of T_{g} based on the expression proposed by Michelsen et al. (2007). Finally, α_{T} is the thermal accommodation coefficient which represents the probability of a surrounding gas molecule of undergoing energy exchange with a soot particle during a collision.

4.1.6. Annealing

When being laser-heated to temperatures above ~2500 K (Michelsen, 2003), soot may experience an annealing process leading to significant modifications of its structure likely to impact its intrinsic properties, and hence its LII response. According to Michelsen (2003), the rate of energy increase by annealing (embedded solely in model 3) is expressed as per Eq. (26):

$$\dot{Q}_{\mathrm{ann}} = N_{\mathrm{p}} \cdot \frac{-\Delta H_{\mathrm{imig}} \cdot k_{\mathrm{imig}} \cdot N_{\mathrm{d}} - \Delta H_{\mathrm{vmig}} \cdot k_{\mathrm{vmig}} \cdot N_{\mathrm{d}}}{N_{\mathrm{A}}} \tag{26}$$

with N_{A} being the number of Avogadro, ΔH_{imig} and ΔH_{vmig} the enthalpy for interstitial and vacancy migrations, respectively, while k_{imig} and k_{vmig} stand for the interstitial and vacancy migration rates. As for N_{d}, it stands for the number of Frenkel or Schottky defects, which can be calculated by solving the following ordinary differential equation:

$$\frac{\mathrm{d}N_d}{\mathrm{d}t} = X_{\mathrm{a}} \cdot \frac{N_{\mathrm{c}}}{2} \cdot k_{\mathrm{diss}} - k_{\mathrm{imig}} \cdot N_{\mathrm{d}} - k_{\mathrm{vmig}} \cdot N_{\mathrm{d}} \tag{27}$$

in which k_{diss} represents the rate constant of pyrolysis of annealed soot, while the annealed fraction X_{a} can be calculated based on Eq. (28):

$$X_{\mathrm{a}} = 1 - \frac{N_{\mathrm{d}}}{X_{\mathrm{d}} \cdot N_{\mathrm{c}}} \tag{28}$$

with X_{d} being the initial defect density estimated from electron spin resonance measurements on soot (Dunne et al., 1997) and N_{c} the number of atoms in primary particles (the reader is referred to Michelsen (2003) for more details regarding the implementation of the annealing flux).

4.1.7. Oxidation

The oxidation of soot induced by the oxygen molecules available in the surrounding atmosphere is considered in both models 3 and 4. According to Michelsen (2003), the enhancement in the particle energy by oxidation can be estimated using the following relation:

$$\dot{Q}_{\mathrm{ox}} = N_{\mathrm{p}} \cdot \frac{\left(\Delta H_{\mathrm{ox}} + 2 \cdot \alpha_{\mathrm{T}} \cdot C_p^{\mathrm{CO}} \cdot T_{\mathrm{p}}\right)}{2 \cdot \omega_1} \cdot \left(\frac{\mathrm{d}M_{\mathrm{p}}}{\mathrm{d}t}\right)_{\mathrm{ox}} \tag{29}$$

where ΔH_{ox} is the enthalpy of formation of CO (set to -2.215×10^5 J mol^{-1}), C_p^{CO} is the heat capacity of CO (calculated using a fitted polynomial function based on the NIST-JANAF database (Chase, 1998)) while the rate of mass loss caused by oxidation is estimated as follows:

$$\left(\frac{\mathrm{d}M_{\mathrm{p}}}{\mathrm{d}t}\right)_{\mathrm{ox}} = \frac{-2 \cdot \pi \cdot {D_{\mathrm{p}}}^2 \cdot \omega_1 \cdot \left(k_{\mathrm{ox,s}} + k_{\mathrm{ox,a}}\right)}{N_{\mathrm{A}}} \tag{30}$$

where $k_{\mathrm{ox,s}}$ and $k_{\mathrm{ox,a}}$ (set to 0 in model 4) represent the oxidation rate constants of unannealed and annealed soot, respectively, whose calculation procedure is detailed in Michelsen (2003). Although models 3 and 4 originally considered Eq. (29) in Michelsen (2003) and Michelsen et al. (2007), we still looked at the alternative formulation proposed in Michelsen et al. (2008) (see Eq. (31)) in section 5.2.2 for the purposes of a sensitivity analysis dealing with the expression of the oxidation flux:

$$\dot{Q}_{\mathrm{ox}} = N_{\mathrm{p}} \cdot \frac{1}{\omega_1} \cdot \left[\int_{T_{\mathrm{ref}}}^{T_{\mathrm{f}}^{\mathrm{CO}}} C_p^{\mathrm{CO}}(T)\mathrm{d}T - \frac{1}{2} \cdot \int_{T_{\mathrm{ref}}}^{T_{\mathrm{g}}} C_p^{\mathrm{O_2}}(T)\mathrm{d}T + \frac{R}{2} \cdot \left(T_{\mathrm{f}}^{\mathrm{CO}} - T_{\mathrm{g}}\right) + \Delta H_{\mathrm{ox}}\right] \cdot \left(\frac{\mathrm{d}M_{\mathrm{p}}}{\mathrm{d}t}\right)_{\mathrm{ox}} \tag{31}$$

with T_{ref} (0 K) and $T_{\mathrm{f}}^{\mathrm{CO}}$ (790 K) being a reference temperature and the temperature at which CO molecules exit from oxidizing particles, respectively.

4.1.8. Thermionic emission

The energy loss induced by the thermal ejection of electrons from heated soot is expressed in model 4 following Eq. (32):

$$\dot{Q}_{th} = N_p \cdot \frac{4 \cdot \phi \cdot m_{el} \cdot \left(\pi \cdot D_p \cdot k_B \cdot T_p\right)^2}{h^3} \cdot exp\left[-\frac{\phi}{k_B \cdot T_p}\right] \tag{32}$$

where ϕ represents a constant work function and m_{el} stands for the mass of an electron. As with the oxidation flux, a sensitivity analysis focusing on the formulation of the thermionic flux was conducted as part of this work (see section 5.2.1). To that end, the refined sub-model proposed by Mitrani et al. (2016) was also considered. The latter is notably based on Eq. (33), in which $\Delta\phi$ denotes the increased barrier to further electron emission due to a positive charge buildup, whose evaluation is supposed to better represent the energy loss of the soot particle:

$$\dot{Q}_{th} = N_p \cdot \frac{4 \cdot (\phi + \Delta\phi) \cdot m_{el} \cdot \left(\pi \cdot D_p \cdot k_B \cdot T_p\right)^2}{h^3} \cdot exp\left[-\frac{(\phi + \Delta\phi)}{k_B \cdot T_p}\right] \tag{33}$$

with $\Delta\phi$ being obtained by solving Eq. (34) at each time step t:

$$\Delta\phi(t) = 8 \cdot \pi \cdot m_{el} \cdot k_{el} \cdot D_p \cdot \int_0^t \frac{\left(\pi \cdot c_{el} \cdot k_B \cdot T_p\right)^2}{h^3} \cdot exp\left[-\frac{(\phi + \Delta\phi)}{k_B \cdot T_p}\right] dt \tag{34}$$

where k_{el} and c_{el} are the Coulomb constant and the charge of an electron, respectively.

4.2. Numerical procedure

The same numerical procedure was used regardless of the considered model. In short, the different terms composing Eq. (1) were expressed using the proper equations, as summarized in Table 1. Contrary to what was done in Lemaire & Menanteau (2021, 2023a), where laser sources exhibiting a non-uniform spatial distribution of the laser irradiance were used, no specific effort was expended herein on spatially discretizing the laser beams used in Goulay et al. (2013) and Bejaoui et al. (2015), since both studies considered spatially homogeneous top hat profiles. We notably proceeded as such since very few works in which this type of profiles is used, consider discretizing the spatial distribution of the energy in the laser excitation domain during LII modeling calculations, despite the existence of inhomogeneities in any laser profile (a point whose influence will be commented on in section 6). The system of coupled differential equations summarized in Eq. (1) was solved using the 'ode15s' multistep variable order solver of MATLAB® (Shampine & Reichelt, 1997). Furthermore, the 'ode45' solver was also used to determine the rate of defects and annihilation needed to obtain the annealed soot fraction in model 3 (see Eq. (27)), while the 'fsolve' function incorporating the default 'trust-region-dogleg' algorithm (MathWorks, 2013) was selected to compute $\Delta\phi$ in the thermionic flux derived from the work by Mitrani et al. (2016) (see Eq. (34)). This led to an inference of the evolution of T_p and D_p as a function of time, which was then introduced into a Planck function integrated over the spectral ranges of the detection systems used by Goulay et al. (2013) and Bejaoui et al. (2015) to generate theoretical LII signals. To conclude, the surrounding gas temperature as well as the soot aggregate and primary particle size were set as detailed in section 3.

5. Results and discussion

5.1. Assessment of the predictive capabilities of standard model formulations

5.1.1. Comparison of measured LII fluence curves with modeled ones and sensitivity analysis dealing with the expressions used to represent the density, the heat capacity and the rate of change of the internal energy of soot

Fig. 1 compares a series of fluence curves issued from the works of Goulay et al. (2013) and Bejaoui et al. (2015) with theoretical results obtained from the implementation of model 1. To obtain these plots, we reported the evolution of the maximum of the LII temporal profiles (referred to as "peak LII signal") as a function of the laser fluence. To ease the comparison between measured and computed data, the LII intensity was, moreover, normalized to 1 for fluences above which the LII responses show a relative lack of fluence dependence or undergo no further increase, as has been done in various works (see Michelsen (2003) or Lemaire & Mobtil (2015) as examples). To that end, a fluence of 0.29 J cm^{-2} was used for an EW of 1064 nm at both 50 mm HAB in the C_2H_4 flame (Fig. 1b) and 15 mm HAB in the $CH_4/O_2/N_2$ flame (Fig. 1d). Alternatively, a value of 0.40 J cm^{-2} was considered at 9 mm HAB in the $CH_4/O_2/N_2$ flame, where soot is still "young", according to Yon et al. (2015) (Fig. 1c). It is indeed well documented that the lower the soot maturity, the lower the absorption of the laser energy (which is especially due to a lower $E(m)$, as exemplified by Bladh et al.

Table 1
Summary of equations used in each LII model.

Model	dU_{int}/dt	$\dot{Q}_{abs}$	$\dot{Q}_{sub}$	$\dot{Q}_{rad}$	$\dot{Q}_{cond}$	$\dot{Q}_{ann}$	$\dot{Q}_{ox}$	$\dot{Q}_{th}$
1	Eq. (3) - $X_a = 0$	Eq. (9)	Eq. (14)	Eq. (24)	Eq. (25)	–	–	–
2	Eq. (4)	Eq. (9)	Eq. (14)	Eq. (24)	Eq. (25)	–	–	–
3	Eq. (3)	Eq. (9)	Eq. (19) - $j_{tot} = 10$	Eq. (24)	Eq. (25)	Eq. (26)	Eq. (29) or (31)	–
4	Eq. (3) - $X_a = 0$	Eq. (12)	Eq. (19) - $j_{tot} = 5$	Eq. (24)	Eq. (25)	–	Eq. (29)	Eq. (32) or (33)

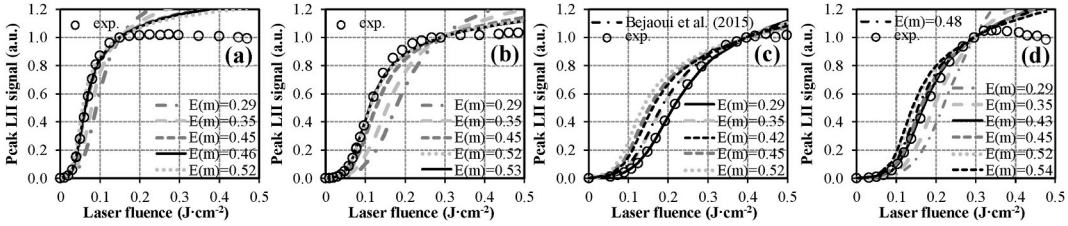

Fig. 1. Comparison of LII fluence curves simulated using model 1 with experimental results (referred to as "exp.") measured at 50 mm HAB in the C_2H_4 diffusion flame using EWs of 532 (**a**) and 1064 nm (**b**), as well as with the data collected with an EW of 1064 nm at 9 (**c**) and 15 mm HAB (**d**) in the $CH_4/O_2/N_2$ premixed flat flame.

(2011a), Bejaoui et al. (2015), or Lemaire & Menanteau (2021 and 2023a)), and the higher the fluence for which the sublimation threshold is reached. Finally, a fluence of 0.15 J cm^{-2} was set to process the data collected in the C_2H_4 flame with an EW of 532 nm (Fig. 1b), which, here again, is in line with the fact that the shorter the wavelength, the higher the absorption cross-section (Lemaire & Menanteau, 2023a), and the lower the fluence for which soot sublimes. Note also that the above-defined normalization points were retained to plot all the fluence curves reported throughout this paper. Calculations were performed considering a default α_T of 0.37, as was done by Bejaoui et al. (2015). Such a preliminary hypothesis is, however, not an issue of concern at this stage as the peak LII signals (and consequently, the shape of the fluence curves) fundamentally depend on the absorption flux. They are therefore not influenced by the value of the thermal accommodation coefficient, which drives the cooling by conduction (see section 5.1.2), and whose influence is only significant when the time t exceeds the laser pulse duration (Menanteau & Lemaire, 2020). As for the tested soot absorption functions (reported in the legends of Fig. 1a–d), they were set based on the review of recent literature by Liu et al. (2020), who reported a minimum and maximum $E(m)$ of 0.29 and 0.52 in the visible and near-infrared for freshly emitted and mature soot, respectively, with a more likely range falling between 0.35 and 0.45. In addition to these values, which were used to obtain the curves plotted in gray lines, optimized $E(m)$ were also tested. To that end, the procedure described in Lemaire & Menanteau (2021, 2023a), which is based on the use of a genetic algorithm-based optimizer (the ga function of MATLAB®), was implemented to infer soot absorption functions allowing to minimize an objective function defined as a least square sum between experimental and numerical data for fluences up to the normalization points. Doing so allowed obtaining the theoretical curves plotted in full black lines (the black dashed and dot-dash lines being for their part commented on further below in this section).

As can be seen by looking at the results obtained with the C_2H_4 flame (see Fig. 1a and b), simulated results merging on a single curve with their experimental counterparts can be obtained in the low and intermediate fluence ranges, provided $E(m)$ values around 0.50 are set ($\sim$0.46 at 532 nm versus $\sim$0.53 at 1064 nm). Although exceeding the more likely range of $E(m)$ recommended by Liu et al. (2020), these values remain globally in line with the upper range of soot absorption functions reported in the literature (i.e., $\sim$0.52). It is, moreover, noteworthy that the $\sim$15 % increase in the soot absorption function observed when the EW goes from 532 to 1064 nm contrasts with the conclusion drawn in the majority of studies, which evidence no significant variation of the $E(m)$ for excitation wavelengths between the visible and the IR (see Lemaire & Menanteau (2023a) and references therein). It is still consistent with the trend reported by Johansson et al. (2017), who observed increases of up to $\sim$8.6 % in the soot absorption function when the EW goes from the visible (i.e., 532 nm) to the IR (i.e., 1064 nm) during analyses conducted with soot exhibiting different maturity levels in an atmospheric ethylene-air diffusion flame. As far as the results relating to the $CH_4/O_2/N_2$ flame are concerned (see Fig. 1c and d), the $E(m)$ needs to be increased from 0.29 to 0.43 for an EW of 1064 nm when the HAB (and thus the soot maturation level) goes from 9 to 15 mm. These values, which allow a good match between measured and simulated fluence curves for low and intermediate fluences fall within the range of soot absorption functions reported in Liu et al. (2020). Furthermore, the $E(m)$ estimated for a HAB of 9 mm (i.e., 0.29) is identical to the value derived in Bejaoui et al. (2015) by means of an energy balance equation derived from Snelling et al. (2004) and Bladh et al. (2011a), in which sublimation was neglected while considering soot temperatures determined from spectrally resolved LII signals and local gas temperatures measured by NO-LIF thermometry. On the other hand, the simulation results from Bejaoui et al. (2015) (depicted by a black dot-dash line in Fig. 1c) diverge from measured data as well as from the fluence curve we obtained when setting the $E(m)$ to 0.29 (see the black solid line in Fig. 1c). This discrepancy is noteworthy since identical LII models and $E(m)$ values were used in both cases. Actually, this observation may be related to the selection of different soot density and heat capacity values (set to 1.90 g cm^{-3} and 2.10 J g^{-1}·K^{-1} in Bejaoui et al. (2015) versus 2.26 g cm^{-3} and 1.90 J g^{-1}·K^{-1} herein). Since the evolution of the peak soot temperatures (and consequently, of the peak LII signals) intrinsically depends on the $E(m)/(\rho_s \cdot c_s)$ ratio in the low-to-intermediate fluence regime, the thermophysical properties selected by Bejaoui et al. (2015) induce an increase in this term, which thus explains why their fluence curve overpredicts the one computed in this work. To complete the analysis of Fig. 1, one can add that even though model 1 globally allows to reproduce measured data at low and intermediate fluences (provided suitable $E(m)$ are selected as a function of the EW and soot maturity), none of the theoretical LII fluence curves, however, match their experimental counterparts for fluences above the sublimation threshold for which simulated peak LII signals keep increasing. As illustrated by Schulz et al. (2006) among others, this behavior is typical of the use of standard LII model formulations. This trend is, moreover, consistent with the temperature profiles obtained in the case of the C_2H_4 flame and depicted in Fig. 2a and b. The curves plotted therein indeed show that the peak soot temperatures computed while considering optimized $E(m)$ of 0.46 and 0.53 for EWs of 532 and 1064 nm, respectively, continuously increase to eventually exceed measured ones for fluences above 0.15 (Fig. 2a) and 0.29 J cm^{-2} (Fig. 2b). Below the sublimation threshold, calculated peak temperatures, however, merge on a single curve with experimentally monitored ones

(see Fig. 2a and b), which is consistent with the fact that the simulated and measured fluence curves depicted in Fig. 1a and b were also superimposed before the so-called plateau region. As for the $CH_4/O_2/N_2$ flame (see Fig. 2c and d), using the $E(m)$ previously identified as being the best suited to properly reproduce measured fluence curves (i.e., 0.29 and 0.43 at 9 and 15 mm HAB, respectively) leads to predicted peak temperatures profiles which underestimate their experimental counterparts, contrary to what would be anticipated. Actually, obtaining computed T_p matching measured ones in the low-to-intermediate fluence regime would require increasing the soot absorption functions to ~0.42 and ~0.54, as illustrated by the black dashed lines in Fig. 2c and d. The fluence curves issued from the use of these $E(m)$, however, diverge from measured ones, as can be seen by looking at the black dashed lines plotted in Fig. 1c and d. This unexpected trend (not observed in the case of the C_2H_4 diffusion flame) could possibly be related to the existence of uncertainties encompassing either measured temperatures, LII signals, or both. In such a situation, using an $E(m)$ of around 0.48 at 15 mm HAB could still represent an acceptable option to obtain computed fluence curves and temperature profiles, which both roughly approximate their experimental counterparts in the low-to-intermediate fluence range (see the black dotted lines in Figs. 1d and 2d). That being said, the results reported in Fig. 1 clearly show that model 1 fails to capture experimentally monitored trends above the sublimation threshold, regardless of the selected soot absorption function.

Regarding the results issued from the implementation of model 2 (which integrates different values for the soot density and heat capacity, as well as distinct expressions of dU_{int}/dt and dM_p/dt (see section 4)), they are summarized in Table 2, where the $E(m)$ allowing to obtain the best fit between measured and predicted fluence curves in the low-to-intermediate fluence range (as illustrated in Fig. 3) are listed and compared with those derived from the implementation of model 1. As can be seen from Fig. 3, the agreement between measured and predicted fluence curves is quite similar below the sublimation threshold whether considering model 1 or 2, provided the soot absorption functions listed in Table 2 are used. Of note, the $E(m)$ inferred when using model 2 exceed those previously derived from the implementation of model 1, with a mean relative difference of 7.0 %. The $E(m)$ assessed with model 2 for mature soot (i.e., at 50 mm HAB in the C_2H_4 flame and at 15 mm HAB in the $CH_4/O_2/N_2$ one) notably exceed the more likely range of values defined by Liu et al. (2020) (i.e., between 0.35 and 0.45).

Furthermore, the soot absorption function derived for an EW of 1064 nm in the case of the C_2H_4 flame is even higher than the upper limit of the extended range reported by Liu et al. (2020), based on a review of the recent literature (i.e., 0.52). The fact that higher $E(m)$ have to be set when implementing model 2 is attributable to the use of different ρ_s and c_s together with the implementation of a different expression of the rate of soot internal energy change. To illustrate this statement, in Fig. 3, we plotted the fluence curves obtained while parameterizing model 2 with the ρ_s, c_s and $E(m)$ used during the calculations performed with model 1 (see the light gray dashed line referred to as "model 2*"). One can then see that the predictions from model 1 and model 2* are identical in the low-to-intermediate fluence range, which is consistent with the fact that the $dc_s/d\,T_p$ term in Eq. (4) becomes zero due to the use of a constant heat capacity, while the dM_p/dt term is negligible below the sublimation threshold, as depicted by the temporal profiles of the soot diameter and mass reported in Fig. 4c for a fluence of 0.088 J cm^{-2}, as an example. Further noting that $\sqrt{2}\cdot\overline{\sigma}\cdot p_g\cdot D_p\cdot\alpha_M << f\cdot k_p\cdot T_p$, as verified by calculation, the right-hand side term of Eq. (16) thus becomes equal to unity, which leads Eq. (16) to be equivalent to Eq. (15) and model 2 to behave similarly to model 1. On the other hand, and although similar temperature profiles are obtained below the sublimation threshold when considering models 1 and 2* (see Fig. 5), the peak soot temperatures derived from the implementation of model 2* are higher than those computed with model 1 at high fluences. This is mainly due to the introduction of the $c_s\cdot T_p\cdot dM_p/dt$ source term in Eq. (4), which increases the internal energy, and in turn, the soot temperature. A smaller soot diameter and mass are then predicted after the laser pulse (see Fig. 4b and d) as a result of an increased sublimation rate (a point illustrated below). As shown in Fig. 5, the highest peak soot temperatures are reached in the high fluence regime when parameterizing model 2 as described in section 4 (i.e., with $\rho_s = 1.86$ g cm^{-3} and c_s computed by means of Eq. (5)). This is actually due to the fact that the $T_p\cdot dc_s/d\,T_p$ term in Eq. (4) becomes non-zero in this case thanks to the use of a temperature-dependent expression to represent the heat capacity. As a consequence, the particle internal energy increases, as does the sublimation rate, as confirmed by the lower soot diameter profile depicted in Fig. 4b. On the whole, a better agreement between measured and simulated temperature profiles can be noted (especially at high fluences) when model 1 is used in the case of the C_2H_4 flame (see Fig. 5a and b). Besides, and as was the case with model 1 (see the above analysis of the results reported in Fig. 2), model 2 fails to reproduce the temperature profiles measured in the $CH_4/O_2/N_2$ flame (see Fig. 5c and d) when using the $E(m)$, allowing to properly reproduce measured fluence curves. Finally, it is noteworthy that the theoretical fluence curves plotted in Fig. 3 with models 1 and 2 are quite similar above the sublimation threshold,

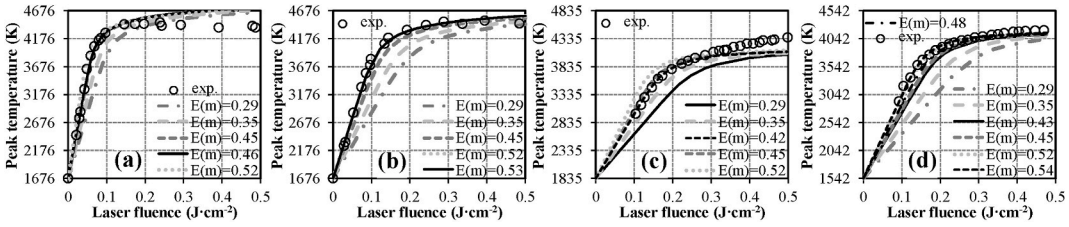

Fig. 2. Comparison of the fluence dependence of the peak soot temperature calculated using model 1 with experimental results (referred to as "exp.") obtained at 50 mm HAB in the C_2H_4 diffusion flame using EWs of 532 (**a**) and 1064 nm (**b**), as well as with the data collected with an EW of 1064 nm at 9 (**c**) and 15 mm HAB (**d**) in the $CH_4/O_2/N_2$ premixed flat flame. Of note, computed temperatures in (**c**) and (**d**) were averaged over a 10-ns period shortly after the peak of the laser pulse following the procedure detailed in Bejaoui et al. (2015) for proper comparisons with measurements.

Table 2
Comparison of $E(m)$ values allowing to obtain the best fit between measured and simulated results when implementing models 1 and 2 in order to simulate the data collected by Goulay et al. (2013) and Bejaoui et al. (2015).

Flame	EW/HAB	Model 1	Model 2	Relative difference Model 2 vs. Model 1 (%)
C_2H_4 (Goulay et al., 2013)	532 nm/50 mm	0.46	0.49	+6.5
	1064 nm/50 mm	0.53	0.57	+7.5
$CH_4/O_2/N_2$ (Bejaoui et al., 2015)	1064 nm/9 mm	0.29	0.32	+6.9
	1064 nm/15 mm	0.43	0.46	+7.0

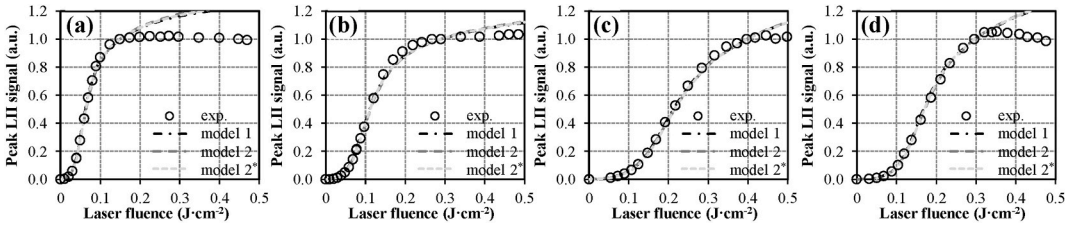

Fig. 3. Comparison of LII fluence curves simulated using models 1 and 2 with experimental results (referred to as "exp.") measured at 50 mm HAB in the C_2H_4 diffusion flame using EWs of 532 (**a**) and 1064 nm (**b**), as well as with the data collected with an EW of 1064 nm at 9 (**c**) and 15 mm HAB (**d**) in the $CH_4/O_2/N_2$ premixed flat flame. The middle and light gray dashed curves, respectively referred to as "model 2" and "model 2*", correspond to simulations performed using ρ_s of 1.86 and 2.26 g cm^{-3}, c_s calculated based on Eq. (5) and taken equal to 1.90 J g^{-1}K^{-1}, together with the $E(m)$ listed in the columns denoted "Model 2" and "Model 1" of Table 2, respectively.

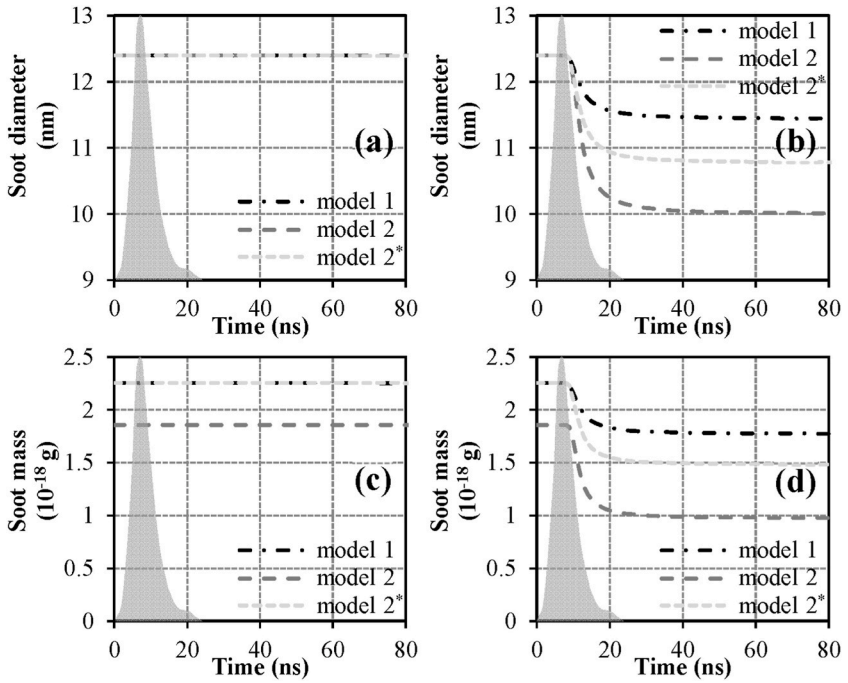

Fig. 4. Theoretical evolution of the soot diameter (**a** and **b**) and mass (**c** and **d**) as a function of time for fluences of 0.088 J cm^{-2} (**a** and **c**) and 0.340 J cm^{-2} (**b** and **d**) in the case of the $CH_4/O_2/N_2$ premixed flat flame for a HAB of 15 mm. The middle and light gray dashed curves, referred to as "model 2" and "model 2*", correspond to simulations performed using ρ_s of 1.86 and 2.26 g cm^{-3}, c_s calculated based on Eq. (5) and taken equal to 1.90 J g^{-1}K^{-1} together with the $E(m)$ listed in the columns denoted "Model 2" and "Model 1" of Table 2, respectively. Note also that the gray areas in each figure represent the temporal profile of the laser pulses used by Bejaoui et al. (2015).

despite the discrepancies highlighted in Fig. 5 as far as the temperature profiles are concerned. This observation may be related to the evolution of the soot diameter D_p which is embedded, together with T_p, within the Planck function used to generate the theoretical LII signals. As shown in Fig. 6a and b, the sublimation rate computed with model 2 is higher than that obtained with model 1. Higher D_p reductions are therefore estimated when model 2 is used, which is exemplified by Fig. 4b. These lower D_p values then compensate for

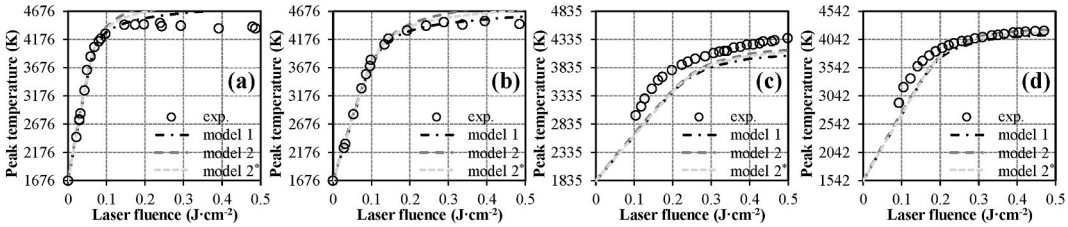

Fig. 5. Comparison of peak soot temperature profiles simulated using models 1 and 2 with experimental results (referred to as "exp.") measured at 50 mm HAB in the C_2H_4 diffusion flame using EWs of 532 (**a**) and 1064 nm (**b**), as well as with the data collected with an EW of 1064 nm at 9 (**c**) and 15 mm HAB (**d**) in the $CH_4/O_2/N_2$ premixed flat flame. The dark and light gray dashed curves, referred to as "model 2" and "model 2*", correspond to simulations performed using ρ_s of 1.86 and 2.26 g cm^{-3}, c_s calculated based on Eq. (5) and taken equal to 1.90 J g^{-1}K^{-1} together with the $E(m)$ listed in the columns denoted "Model 2" and "Model 1" of Table 2, respectively.

the higher soot temperatures predicted by model 2 (see Figs. 5, 6**c** and 6**d**), hence contributing to ultimately obtaining fluence curves quite similar, whether using model 1 or 2. When analyzing in further detail the results depicted in Fig. 6a and b, one can note that the temporal profiles of the different energy transfer rates are comparable to those previously reported by Michelsen et al. (2007) and Lemaire & Mobtil (2015), who implemented similar standard model formulations. The curves plotted in Fig. 6 especially show that the increase of the soot temperature (Fig. 6c and d) during the laser pulse duration is predominantly determined by the absorptive-heating flux (see Fig. 6a and b), which is directly correlated with $E(m)$, as per Eqs. (9) and (10). Furthermore, and as can be seen in Fig. 6a, the peak of the absorption rate is two orders of magnitude higher than that of the other fluxes in the low fluence regime. Alternatively, the curves plotted for a fluence of 0.340 J cm^{-2} show that $\dot{Q}_{abs}$ mainly controls the LII process during the first 12 ns following the beginning of the laser pulse, whereupon $\dot{Q}_{sub}$ becomes predominant. As a result of this competition between absorption and sublimation rates, the peak soot temperature in Fig. 6d is reached sooner than that in Fig. 6c. While being consistent with the simulation results previously reported by Lemaire & Mobtil (2015), this observation also agrees with the trend commonly reported in the literature indicating that the higher the fluence, the sooner the peak of the LII signal is reached (Schulz et al., 2006). As far as soot cooling is concerned, it is mainly controlled by conduction at low fluence, as shown in Fig. 6a. On the other hand, $\dot{Q}_{sub}$ prevails for the time comprised between ~12 ns and ~38 ns in Fig. 6b, while $\dot{Q}_{cond}$ predominantly drives the cooling rate afterward. These observations therefore suggest that the mass and thermal accommodation coefficients (α_M and α_T) embedded within $\dot{Q}_{sub}$ and $\dot{Q}_{cond}$, respectively (see sections 4.1.3 and **4.1.5**), will be key parameters to consider for the modeling of the LII time decays, as will be discussed in section 5.1.2. Regarding the

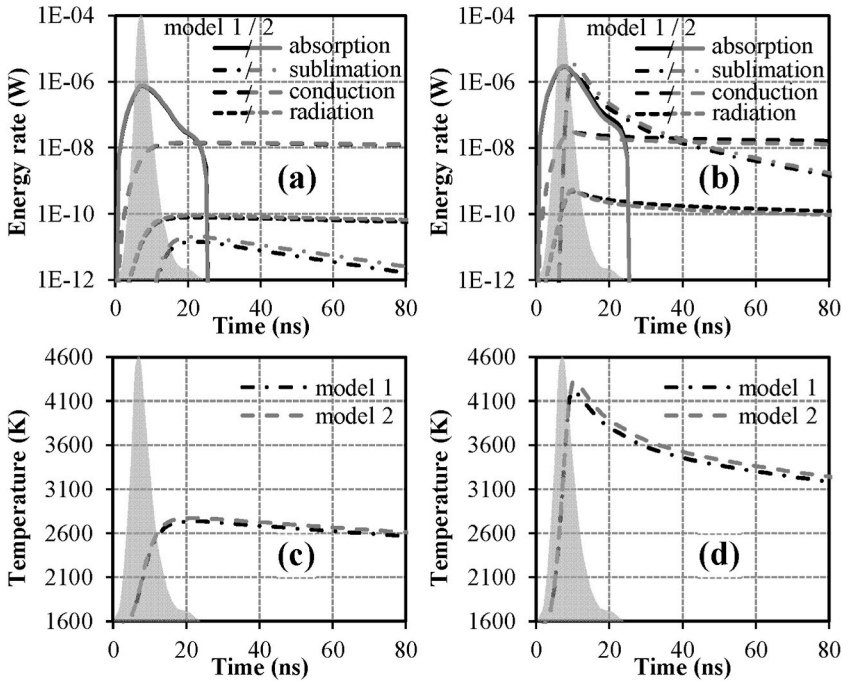

Fig. 6. Temporal evolution of the energy transfer rates (**a** and **b**) and soot temperature (**c** and **d**) computed using models 1 (black curves) and 2 (gray curves) for fluences of 0.088 J cm^{-2} (**a** and **c**) and 0.340 J cm^{-2} (**b** and **d**) in the case of the $CH_4/O_2/N_2$ premixed flat flame for a HAB of 15 mm. Note that the gray areas in each figure denote the temporal profiles of the laser pulses used by Bejaoui et al. (2015).

radiation rate, it is significantly lower than the other energy fluxes at both low and high fluences. It is thus expected to contribute negligibly to particle heat loss during LII, hence explaining why it is often neglected in modeling studies dealing with atmospheric flames (see Table A1). As for the heating stage, the parameters of interest (apart from the soot absorption function, whose relative impact on LII fluence curves has already been assessed above) comprise the values and/or empirical expressions used to represent the soot density and heat capacity, as well as the formulation of the equation used to compute the change of the particle internal energy. A sensitivity analysis dealing with these factors will therefore be conducted below to gain insights into how they may influence the LII fluence curves computed by means of models 1 and 2. To that end, different expressions of ρ_s, c_s and dU_{int}/dt from the literature will be tested to assess their relative impact on the $E(m)$ inferred by minimizing the least square sum between experimental and numerical fluence curves.

As far as the soot density and heat capacity are concerned, constant values of 2.26 g cm^{-3} and 1.90 J g^{-1}.K^{-1} issued from the work of Melton (1984) were first considered. Secondly, a ρ_s of 1.86 g cm^{-3}, together with the temperature-dependent expression of c_s depicted in Eq. (5), was considered, as suggested by Kock et al. (2006), and used by Hofmann, Kock, & Schulz (2007). Eqs. (6) and (7), issued from the work of Michelsen (2003), were then implemented to compute ρ_s and c_s, in addition to Eqs. (35) and (36) recently proposed by the same author (Michelsen, 2021).

$$\rho_s = \frac{\omega_c \cdot C/H + \omega_H}{C/H + 1} \times \frac{1}{5.91 \cdot \left[1 + 2.163 \times 10^{-5} \cdot (T_p - 298.15)\right]^3} \tag{35}$$

$$c_s = \frac{1.70 \times 10^5 \cdot T_p^{2.07}}{1 + \left(\frac{T_p}{423.44}\right)^{2.07}} + 0.12 \cdot exp\left[\frac{-(T_p - 149)}{87.4}\right]^2 \times \frac{(C/H + 1) \cdot \left\{5.91 \cdot \left[1 + 2.163 \times 10^{-5} \cdot (T_p - 298.15)\right]^3\right\}}{\omega_c \cdot C/H + \omega_H} \tag{36}$$

As can be seen, the last two expressions consider not only the effect of the temperature on the soot density and heat capacity, but also the maturation level of the particles through the carbon-to-hydrogen ratio (denoted C/H in Eqs. (35) and (36)), whose value was set to 2, 8 and 20 herein in order to simulate the behavior of incipient and more mature particles (Michelsen, 2021). Obtained results are reported in Table 3, which lists the $E(m)$ values allowing to obtain the best fit between measured and predicted fluence curves in the low-to-intermediate fluence range for each set of density and heat capacity values and/or expressions. One can then note that using the ρ_s and c_s issued from the work of Kock et al. (2006) instead of the constant values from Melton (1984) leads to a mean decrease of 10.0 % of the $E(m)$ inferred using model 1. This trend can be explained by the fact that the product of ρ_s and c_s is typically lower when considering the parameterization proposed by Kock et al. (2006) on the range of temperatures corresponding to the increasing section of the fluence curves (see Fig. 7). The peak soot temperatures (and in turn the peak LII signals) computed by means of model 1 in the low-to-intermediate fluence regime indeed depend on the $E(m)/(\rho_s \cdot c_s)$ ratio, as explained above. Obtaining identical LII responses whether considering the ρ_s and c_s from Kock et al. (2006) or Melton (1984) therefore requires lowering the $E(m)$ values when performing the calculations with the density and heat capacity taken from Kock et al. (2006) in order to obtain $E(m)/(\rho_s \cdot c_s)$ ratios similar to those derived from the implementation of the parameters proposed by Melton (1984). Conversely, the product of ρ_s and c_s is higher when using the empirical expressions proposed by Michelsen (2003) (Eq. (6) and (7)) and Michelsen (2021) (Eq. (35) and (36)) instead of the values issued from Melton (1984) (see Fig. 7). As a result, soot absorption functions between 6.5 and 7.5 % higher on average are

Table 3
Comparison of $E(m)$ values allowing to obtain the best fit between measured and computed results when implementing models 1 and 2 to simulate the data collected by Goulay et al. (2013) and Bejaoui et al. (2015) while using different values and/or empirical expressions from the literature to represent ρ_s and c_s. Note that when the inferred $E(m)$ deviate by more than 15 % from the extended range of plausible values reported by Liu et al. (2020) (i.e., between 0.29 and 0.52), only an "out-of-bounds" mention (denoted 'OOB') is provided.

Flame	EW/HAB	Model 1/Model 2 (Relative difference Model 2 vs. Model 1 (%))			
		ρ_s = 2.26 g cm^{-3} c_s = 1.90 J g^{-1}K^{-1}	ρ_s = 1.86 g cm^{-3} c_s = Eq. (5)	ρ_s = Eq. (6) c_s = Eq. (7)	ρ_s = Eq. (35) c_s = Eq. (36)
C_2H_4 (Goulay et al., 2013)	532 nm/50 mm	0.46/0.47 (+2.2 %)	0.41/0.49 (+19.5 %)	0.49/0.59 (+20.4 %)	0.49 † (1)/OOB (–)
	1064 nm/50 mm	0.53/0.54 (+1.9 %)	0.48/0.57 (+18.8 %)	0.57/OOB (–)	0.57 † (2)/OOB (–)
$CH_4/O_2/N_2$ (Bejaoui et al., 2015)	1064 nm/9 mm	0.29/0.29 (~0 %)	0.26/0.32 (+23.1 %)	0.31/0.37 (+19.4 %)	0.31 † (3)/0.40 † (4) (+29.0 %)
	1064 nm/15 mm	0.43/0.44 (+2.3 %)	0.39/0.46 (+17.9 %)	0.46/0.54 (+17.4 %)	0.46 † (5)/0.58 † (6) (+26.1 %)

† Mean value computed considering different C/H ratios/
(1) Values comprised between 0.488 and 0.493 as a function of the C/H ratio/
(2) Values comprised between 0.567 and 0.573 as a function of the C/H ratio/
(3) Values comprised between 0.312 and 0.314 as a function of the C/H ratio/
(4) Values comprised between 0.402 and 0.403 as a function of the C/H ratio/
(5) Values comprised between 0.456 and 0.459 as a function of the C/H ratio/
(6) Values comprised between 0.581 and 0.582 as a function of the C/H ratio.

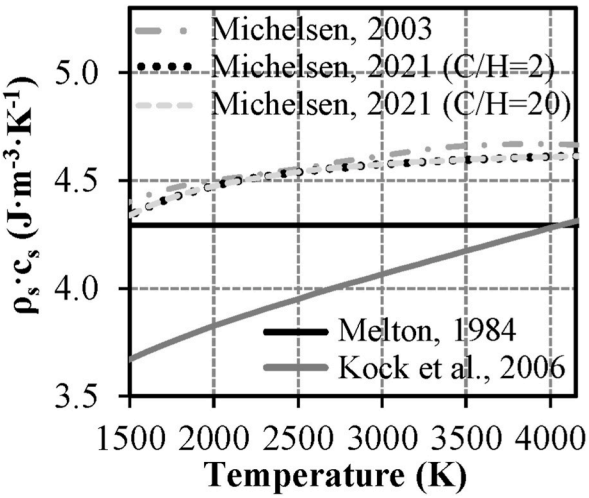

Fig. 7. Evolution of the product of ρ_s and c_s as a function of the temperature when considering the values and/or empirical expressions proposed by Melton (1984), Kock et al. (2006) and Michelsen (2003, 2021) to represent soot density and heat capacity.

inferred when selecting the parameterized equations from Michelsen (2003, 2021) as depicted in Table 3. Since the c_s values calculated by means of Eq. (5) or (7) only diverge by ~1 % on average for temperatures going from 1500 to 4500 K, as illustrated in Michelsen et al. (2007), comparing the results reported in the fourth and fifth columns of Table 3 thus allows assessing the relative impact of the values taken by the soot density on the so inferred soot absorption functions. Obtained data then show that implementing the empirical expression from Michelsen (2003) instead of the constant value taken from Kock et al. (2006) induces an increase of 18.9 % on average of the $E(m)$ estimated by means of model 1. On the other hand, using the equations recently proposed by Michelsen (2021) for ρ_s and c_s instead of those previously suggested in Michelsen (2003) does not induce any significant deviation in obtained results, as demonstrated by the relative difference between the soot absorption functions reported in the fifth and sixth columns of Table 3. Note also that increasing the C/H ratio from 2 to 20 in Eqs. (35) and (36) induces relatively minor variations (less than 0.6 % on average) in the inferred $E(m)$ values, hence explaining why solely mean data were reported in the sixth column of Table 3. As far as model 2 is concerned, the estimated soot absorption functions are found to increase by 6.2 %, 25.3 % and more than 30 % on average, when considering the soot density and heat capacity proposed by Kock et al. (2006), Michelsen (2003) and Michelsen (2021), respectively, instead of the values taken from Melton (1984). As previously explained, the inclusion of the $T_p \cdot \mathrm{d}c_s/\mathrm{d}\,T_p$ term in Eq. (4), whose value becomes non-zero when using temperature-dependent expressions for c_s, contributes to enhancing the soot internal energy computed by model 2. As a consequence, higher $E(m)$ values have to be set to increase $\dot{Q}_{abs}$ and fulfil the energy balance depicted in Eq. (1). Reiterating that the soot absorption function must be comprised between 0.29 and 0.52, and more probably between 0.35 and 0.45 according to Liu et al. (2020), one can conclude that only the ρ_s and c_s taken from Melton (1984) and Kock et al. (2006) seem to be adapted when being used in conjunction with model 1. As for model 2, suitable $E(m)$ values can be inferred solely when using the constant ρ_s and c_s proposed by Melton (1984). Concerning the empirical expressions proposed by Michelsen (2003, 2021), their use leads to soot absorption functions falling outside of the range of values recommended by Liu et al. (2020) for mature soot, especially when model 2 is used. Before drawing any conclusion regarding the validity of these correlations, one should, however, note that inferring information on the evolution of soot properties using simplified LII models must be done with caution. As explained in Lemaire & Menanteau (2023a), more comprehensive heat and mass balance equations incorporating advanced sub-model formulations together with additional physical processes (such as internal multiple scattering (MS) within soot aggregates) are indeed a must if consistent information on soot optical properties is to be derived. To illustrate how MS may influence the $E(m)$ assessment, additional calculations were performed while integrating the corrective factor from Yon et al. (2014, 2015) within the expression of the soot absorption cross-section embedded in model 1 (see Eq. (10)) so that:

$$C_{abs,s} = N_{tot} \cdot (1 - X_a) \cdot \frac{\pi^2 \cdot {D_p}^3}{\lambda_1} \cdot E(m) \cdot h_{\lambda,N_p} \cdot p(N_p) \tag{37}$$

with N_{tot} being the aggregate number density, h_{λ,N_p} the MS corrective factor whose calculation procedure is notably detailed in Lemaire & Menanteau (2021) and $p(N_p)$ the probability density function of the aggregate size. Obtained results (not detailed, for brevity) then showed that considering MS allows to reduce the $E(m)$ reported in the sixth column of Table 3 by ~12 % on average, thus leading to values falling below the upper limit of 0.52 (Liu et al., 2021). As can be seen from Table 3, higher soot absorption functions are systemically inferred when using model 2 instead of model 1 (see the relative differences reported in brackets). This trend actually stems from the formulation of the rate of change of the particle internal energy. More specifically, the fact that $E(m)$ that are 1.6 % higher on average are estimated when using model 2 instead of model 1 while setting ρ_s and c_s to 2.26 g cm^{-3} and 1.90 J g^{-1}·K^{-1} is due to the introduction of the $c_s \cdot T_p \cdot \mathrm{d}M_p/\mathrm{d}t$ source term in Eq. (4), as previously noted. The so-observed discrepancies remain moderate,

however, since the $T_p \cdot dc_s/d\,T_p$ term of Eq. (4) is zero when the heat capacity is constant. Alternatively, using temperature-dependent expressions for c_s (as is the case in the fourth, fifth and sixth columns of Table 3) induces significant increases of the inferred $E(m)$ when model 2 is implemented instead of model 1. Here again, and as previously explained, this trend ensues from the introduction of the $T_p \cdot dc_s/d\,T_p$ term in Eq. (4), which contributes to increasing the soot internal energy. Actually, there has been some debate in the LII community about which formulation of the rate of soot internal energy change should be considered (Michelsen et al., 2007). The validity of different expressions, including those proposed by Hiers (1997, 2000) and Hofmann, Kock, & Schulz (2007), was notably discussed by Liu & Snelling (2007), who derived the unsteady-state energy conservation equation of small particles based on the first law of thermodynamics applied to an open system. Doing so led the authors to conclude that the expressions suggested by Hiers (1997, 2000) and Hofmann, Kock, & Schulz (2007) were incorrect due to the introduction of a nonphysical source term in the energy equation leading to physically erroneous peak particle temperatures at high laser fluences, as also observed herein. Michelsen et al. (2008) subsequently supported this conclusion and proposed an alternative formulation (see Eq. (38)) integrating an extra term accounting for the loss of some ability to store sensible heat when the mass of soot particles is reduced.

$$\frac{dU_{int}}{dt} = N_p \cdot M_p \cdot c_s \cdot \frac{dT_p}{dt} + N_p \cdot \left[\int_{T_{ref}}^{T} c_s(T)dT\right] \cdot \frac{dM_p}{dt} \tag{38}$$

That same year, Hiers (2008) showed that a rigorous control volume approach yields to Eq. (39) (where u_p stands for the specific particle internal energy), which should be considered as the appropriate equation to represent the rate of change of the internal energy of a particle undergoing processes relevant to LII.

$$\frac{dU_{int}}{dt} = N_p \cdot M_p \cdot c_s \cdot \frac{dT_p}{dt} + N_p \cdot u_p \cdot \frac{dM_p}{dt} \tag{39}$$

When implementing this relation (which is fundamentally identical to Eq. (38)), the extra term on the right-hand side is, however, cancelled in the energy balance from Eq. (1) by extra terms introduced in similar expansions of terms embedded within the sublimation and/or oxidation fluxes (Michelsen et al., 2015). Consequently, using Eq. (38) or (39) turns out to be equivalent to implementing Eq. (3). For completeness, we still made additional calculations to assess the relative impact of the formulation of the rate of soot internal energy change on the $E(m)$ estimated by modeling. To that end, simulations were performed by integrating either Eq. (3) or (4) in model 2. Obtained results then showed that the implementation of the dU_{int}/dt expression from Hofmann, Kock, & Schulz (2007) instead of the one taken from Melton (1984) leads to an overestimation of the soot absorption functions derived from the analysis of the signals collected in both the C_2H_4 and $CH_4/O_2/N_2$ flames by 17.0 % ± 1.0 % on average. While showing that the expression considered in computing the internal energy variation rate is quite critical, the above analysis also corroborated the conclusions drawn by Liu & Snelling (2007) regarding the fact that the selection of Eq. (4) leads to the introduction of a nonphysical source term in the energy equation, which may result in erroneous evaluations of the soot temperatures and $E(m)$. Although the model formulation proposed by Hofmann, Kock, & Schulz (2007) can still be considered as acceptable when calculations are performed in the low fluence regime ($c_s \cdot T_p \cdot dM_p/dt \rightarrow 0$) and with a constant c_s ($T_p \cdot dc_s/d\,T_p = 0$), simulation results derived from its use in other conditions must, however, be addressed with caution, thus explaining why the focus will be more specifically on model 1 in section 5.1.2.

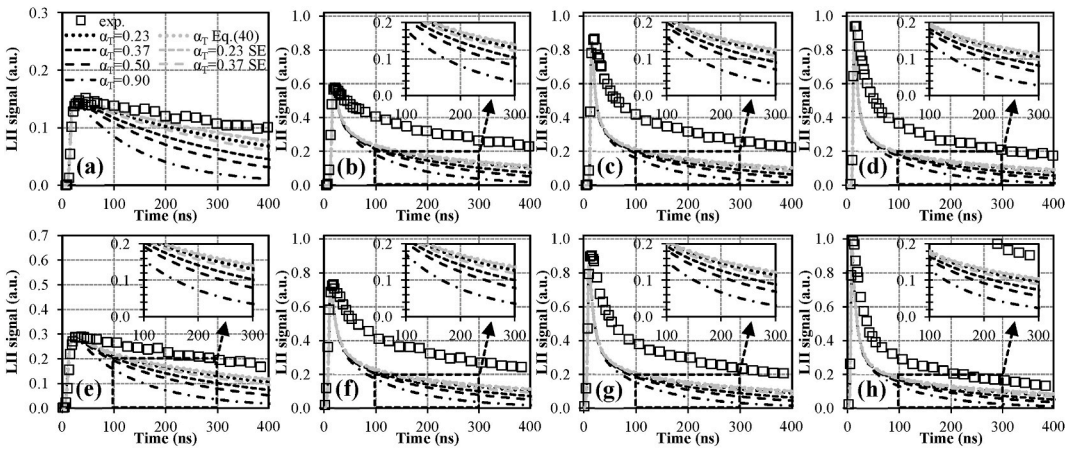

Fig. 8. Comparison of LII time decays simulated using model 1 with their experimental counterparts (referred to as "exp.") measured at 50 mm HAB in the C_2H_4 diffusion flame with EWs of 532 ((**a**), (**b**), (**c**) and (**d**)) and 1064 nm ((**e**), (**f**), (**g**) and (**h**)) and fluences of 0.040 J cm^{-2} (**a**), 0.069 J cm^{-2} (**b**), 0.100 J cm^{-2} (**c**), 0.124 J cm^{-2} (**d**), 0.088 J cm^{-2} (**e**), 0.146 J cm^{-2} (**f**), 0.194 J cm^{-2} (**g**) and 0.268 J cm^{-2} (**h**). Calculations were performed by setting the $E(m)$ to 0.46 and 0.53 at 532 and 1064 nm, respectively, while α_T was parameterized as detailed in the legend of (**a**), which also applies to the other subfigures. Note that the insets correspond to a zoom-in on the time domain extending from 100 to 300 ns to better highlight the effect of α_T on simulated LII time decays.

5.1.2. Comparison of measured LII time decays with modeled ones and sensitivity analysis dealing with the effect of radiation as well as with the values taken by the thermal and mass accommodation coefficients

LII time decays computed with model 1 while using different thermal accommodation coefficients are compared with their experimental counterparts in Figs. 8 and 9 for the C_2H_4 and $CH_4/O_2/N_2$ flames, respectively. Of note, calculations were performed using the $E(m)$ previously estimated in section 5.1.1 (i.e., those allowing to obtain the best match between measured and simulated fluence curves below the sublimation threshold). Concerning α_T, it was set to the values listed in the legends of Figs. 8 and 9 based on the range of thermal accommodation coefficients considered in the comparison analysis by Michelsen et al. (2007). This includes values between 0.23 (as estimated by Kuhlmann and Will (2005) or Liu, Snelling, & Smallwood (2005)) and 0.90 (according to the α_T used in the early work by Melton (1984)). Furthermore, we also implemented the expression proposed by Michelsen (2009) to compute a surface-temperature and gas-temperature-dependent global accommodation coefficient as per Eq. (40):

$$\alpha_T = \left[0.28 - 3.23 \times 10^{-5} \cdot T_p + 0.80 \cdot exp\left(-1.53 \times 10^{-3} \cdot T_p\right)\right] \cdot \left(0.175 + 5 \times 10^{-4} \cdot T_g\right) \quad (40)$$

As can be seen from the curves depicted in Fig. 8, model 1 fails to capture the LII time decays measured in the C_2H_4 flame regardless of the α_T considered. It indeed overestimates soot cooling, as evidenced by the fact that the theoretical signals systematically underestimate their experimental counterparts after the peak of the LII emission, which is assessed a few ns after the first photons of the laser are emitted. Furthermore, it is noteworthy that simulated time decays are significantly shorter than measured ones even when selecting a relatively low α_T of 0.23, noting that values ≥ 0.28 are more commonly considered in common LII models (Michelsen et al., 2007). The inability of model 1 to properly simulate the data from Goulay et al. (2013) is, however, consistent with the conclusions from Mansmann et al. (2018) who also implemented a Melton-based model while concluding that further data on this particular flame would be required to help distinguish whether the discrepancies observed between measured and simulated results are dependent on the specific experiment or on the implemented modeling tool. As for the simulation of the time decays collected at 9 mm HAB in the $CH_4/O_2/N_2$ flame, the curves from Fig. 9 show that modeled signals overestimate measured ones at low fluence (see Fig. 9a), except when the thermal accommodation coefficient is set to an unrealistically high value of 0.9, which is more likely to be adapted for soot at room temperature exhibiting a disordered surface fine structure (Michelsen et al., 2015). Alternatively, adjusting the thermal accommodation coefficient between 0.37 and 0.50 allows to satisfactorily reproduce the experimental data for fluences of 0.169 J cm^{-2} (see Fig. 9b) and 0.217 J cm^{-2} (see Fig. 9c). Finally, and as illustrated by the plots of Fig. 9d, mimicking the LII time decay detected for a fluence of 0.284 J cm^{-2} can be roughly achieved (especially for $t > 100$ ns) when using a α_T of 0.23. Concerning the results obtained for a HAB of 15 mm, Fig. 9e–h shows that computing theoretical time decays matching measured ones requires setting the thermal accommodation coefficient to 0.37 for a fluence of 0.088 J cm^{-2} (Fig. 9e) versus a value comprised between 0.23 and 0.37 at 0.138 J cm^{-2} (Fig. 9f). For a fluence of 0.186 J cm^{-2} (see Fig. 9g), one has to adjust the α_T to 0.23 to derive signals which roughly approximate their experimental counterparts (especially for $t > 200$ ns). None of the tested thermal accommodation coefficient, however, allows obtaining a good agreement between simulated and measured data for higher fluences, as exemplified by the curves plotted in Fig. 9h, which show that the cooling process is consistently overpredicted by the model, regardless of the α_T. Notwithstanding the inability of model 1 to reproduce the experimental data depicted in Fig. 9a and h, one can still note that the α_T identified as being the best suited to mimic the signals measured for intermediate fluences (i.e., between ~0.1 and ~0.2 J cm^{-2}) are consistent with the plausible range of α_T reported in the literature. A brief overview of past studies undertaken to evaluate this parameter indeed shows that its value typically spans a range of ~0.2 to ~0.5, comprising the above-cited value of 0.23 issued from the works of Kuhlmann and Will (2005)

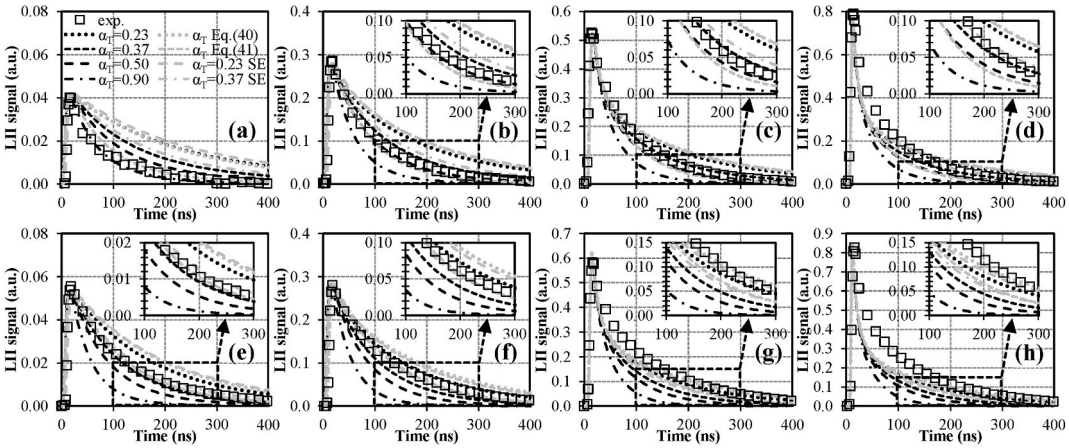

Fig. 9. Comparison of LII time decays simulated using model 1 with their experimental counterparts (referred to as "exp.") measured at 9 ((**a**), (**b**), (**c**) and (**d**)) and 15 mm HAB ((**e**), (**f**), (**g**) and (**h**)) in the $CH_4/O_2/N_2$ premixed flat flame with fluences of 0.089 J cm^{-2} (**a**), 0.169 J cm^{-2} (**b**), 0.217 J cm^{-2} (**c**), 0.284 J cm^{-2} (**d**), 0.088 J cm^{-2} (**e**), 0.138 J cm^{-2} (**f**), 0.186 J cm^{-2} (**g**) and 0.234 J cm^{-2} (**h**). Calculations were performed by setting the $E(m)$ to 0.29 and 0.43 at 9 and 15 mm HAB, respectively, while α_T was parameterized as detailed in the legend of (**a**), which also applies to the other subfigures. Note that the insets correspond to a zoom-in on the time domain extending from 100 to 300 ns to better highlight the effect of α_T on simulated LII time decays.

and Liu, Snelling, & Smallwood (2005). Prior to that, Leroy et al. (1997) proposed a α_T of 0.26 from measurements of N_2 scattered from graphite. Kuhlmann, Reimann, & Will (2006) later investigated the heat transfer behavior of a variety of carbon black samples under conditions relevant for LII and derived an extrapolated physical accommodation coefficient for isolated particles of 0.43 and an effective accommodation coefficient of 0.25, which was considered as adequately describing the "average" heat transfer behavior of the tested particles. In a subsequent LII modeling study, Snelling et al. (2009) estimated that α_T varies somewhat with the soot temperature in the 0.36 to 0.46 range. Higher values close to 0.50 were, moreover, also estimated by Häger et al. (1997) based on measurements of NO scattered from graphite surfaces, as well as by Eremin et al. (2006) or Menanteau & Lemaire (2020), through the modeling of time-resolved LII signals. Although the α_T values in common use in LII models more particularly span the relatively narrow range of 0.23–0.37 (Michelsen et al., 2007), the thermal accommodation coefficients inferred herein when modeling the data from Bejaoui et al. (2015) still agree with the limit values of ~0.2 and ~0.5 identified above, based on a brief review of the literature. A more detailed analysis of the results depicted in Fig. 9, moreover, tends to suggest that the thermal accommodation coefficient decreases when the fluence (and hence the soot temperature) increases, which agrees with the conclusions drawn by Michelsen (2009) based on state-to-state measurements of NO scattered from graphite surfaces, as a function of the surface temperature and incidence energy. The results we obtained further suggest that the lower the ambient gas temperature, the lower the thermal accommodation coefficient as observed when comparing the α_T inferred at 9 and 15 mm HAB, for which T_g values of 1835 ± 100 K and 1542 ± 100 K were estimated by Bejaoui et al. (2015) (see section 3). Here again, this trend agrees with the surface scattering measurements from Michelsen (2009), but with the conclusions from Daun (2009) and the observations from Bladh et al. (2011a) as well. That being said, and although Eq. (40) proposed by Michelsen (2009) takes into account the surface-temperature and gas-temperature-dependencies of the thermal accommodation coefficient, its use, however, leads to unsatisfactory results, as illustrated in Fig. 9. The soot cooling is indeed underpredicted at low and intermediate fluences when calculating α_T from Eq. (40), while the contrary is observed for higher fluences, as exemplified by the black dot-dash curves plotted in Fig. 9. In an attempt to derive an alternative temperature-dependent expression whose use would allow inferring α_T values more suitable for properly simulating the data from Bejaoui et al. (2015), we implemented an optimization procedure based on the use of a genetic algorithm-based solver (the ga function of MATLAB® (MathWorks, 2013)), as was previously done in Lemaire & Menanteau (2021, 2023a). Actually, this procedure was intended to derive empirical coefficients whose use in a polynomial equation involving T_p and T_g would lead to α_T allowing to minimize an objective function built upon the sum of the least square errors between 100 equidistant samples issued from the decreasing section of simulated and measured LII time decays for fluences between ~0.09 and ~0.25 J cm^{-2} and HAB of 9 and 15 mm HAB in the $CH_4/O_2/N_2$ flame. In doing so, we derived the following relation valid for T_g and T_p comprised in the ~1500-~1800 K and ~1900-~4000 K ranges, respectively, based on the temperatures characterizing the data processed to perform the optimization:

$$\alpha_T = \left(-1.916 - 1.588 \times 10^{-3} \cdot T_p + 4.463 \times 10^{-7} \cdot T_p^2 \right) \cdot \left(4.609 \times 10^{-1} - 4.012 \times 10^{-4} \cdot T_g + 2.010 \times 10^{-8} \cdot T_g^2 \right) \quad (41)$$

The results obtained while using Eq. (41) are plotted using full gray lines in Fig. 9. One can then see that although the model predictions keep overestimating the soot cooling at high fluences (especially above ~0.20 J cm^{-2}), the agreement between simulated and experimentally monitored time decays is significantly improved for fluences below ~0.15 J cm^{-2} (see Fig. 9a, **b**, **e** and **f**). Although this is somewhat encouraging, caution should nonetheless be exercised when drawing clear-cut conclusions regarding the validity of Eq. (41). The optimization work we did indeed does not claim to infer a α_T formulation that should be considered as universally valid, especially since the proposed fitting procedure was conducted based on a relatively small sample of LII signals collected within the same flame, hence making the validity domain of the correlation depicted in Eq. (41) quite narrow. Furthermore, uncertainties associated with the potential temperature dependence of α_T are considerable in the literature. In fact, while some works concluded that the thermal accommodation depends on T_p (Michelsen, 2009), the contrary was alternatively reported in other studies, including the one by Daun (2009) who estimated that α_T may be modeled as constant since laser-heated particles cool back to T_g. Furthermore, a lack of consistent experimental data also makes it difficult to properly assess the evolution of α_T as a function of T_g, hence explaining why a majority of LII modelers consider constant thermal accommodation coefficients when performing their calculations (Michelsen et al., 2007). Finally, it is fundamental to emphasize that even though inferring α_T values by means of LII modeling is quite common (Maffi et al., 2011; Menanteau & Lemaire, 2020; Snelling et al., 2009), this type of procedure implicitly assumes that the model implemented is accurate and that there are no ill-defined factors likely to influence simulated signals. The fact, however, is that there are various phenomena which, when neglected, may lead to significant biases in computed LII decay rates. This notably includes the so-called shielding effect (SE) resulting from the presence of several primary particles within aggregates (Snelling et al., 2004). As demonstrated by Kuhlmann, Reimann, & Will (2006) or Menanteau & Lemaire (2020) as examples, taking into account soot aggregate properties may indeed drastically impact the values of the thermal accommodation coefficient evaluated by inverse calculations. Although we examined in detail the influence of the shielding effect on the modeling of the rate of energy loss by conduction in Menanteau & Lemaire (2020), we still performed additional calculations by suppressing N_p in Eq. (25) while replacing D_p with the equivalent heat conduction diameter (D_{HC}) proposed by Liu et al. (2006a):

$$D_{HC} = \begin{cases} D_p \text{ , if } N_p = 1 \\ D_p \cdot \left(\frac{N_p}{k_h} \right)^{1/D_h} \text{, if } N_p > 1 \end{cases} \quad (42)$$

with k_h and D_h being scaling factors whose expressions are provided in Appendix 2. As can be seen by looking at the gray curves

denoted SE in Figs. 8 and 9, which were obtained by setting α_T to values of 0.23 and 0.37 as examples, integrating the shielding effect leads to the obtention of time decays which are longer than those computed using the same thermal accommodation coefficients, but while neglecting SE. This trend is actually consistent with the effect of the shielding process, which tends to reduce the rate of energy dissipation by conduction per primary particle contained in the aggregates as compared to the conduction flux calculated when neglecting this phenomenon. As a result, integrating the SE in the modeling of the conduction flux to compute time decays matching their counterparts issued from calculations performed while neglecting this process requires increasing the values of the thermal accommodation coefficient. For instance, α_T should be set to 0.30 to obtain LII time decays in the ethylene flame matching those computed when neglecting the SE, and considering an α_T of 0.23 (corresponding curves not plotted in the graphs for clarity due to superimposition issues). Similarly, to simulate the data acquired at 9 mm HAB in the methane flame with intermediate fluences, the thermal accommodation coefficient should be increased to values ranging from 0.44 to 0.62 when considering SE versus values between 0.37 and 0.50 when neglecting it. At 15 mm HAB in the same flame, α_T needs to be set to values going from 0.27 to 0.48 for fluences ranging from 0.088 to 0.186 J cm^{-2} instead of values between 0.23 and 0.37 when neglecting the SE. Since for a given conductive cooling rate, integrating the shielding effect intrinsically leads to inferring higher α_T values as exemplified above, thermal accommodation coefficients falling outside of the classical range of values (i.e., between ~0.2 to ~0.5) can thus be assessed, as is the case at 9 mm HAB in the methane flame, where a $\alpha_T > 0.9$ should be considered for a fluence of 0.088 J cm^{-2}. To conclude this short discussion on the shielding effect, the above results clearly showed that this phenomenon is likely to significantly influence the modeling of LII time decays, as previously illustrated in Menanteau & Lemaire (2020). Considering an equivalent heat conduction diameter in the calculation of the conduction flux is, however, not sufficient to explain the discrepancies observed between measured and simulated data in Figs. 8 and 9. Considering the SE, moreover, does not truly help to improve the agreement between experimental and computed results herein since high thermal accommodation coefficients, likely to fall outside of the range of values commonly considered in the literature, must be set in this case. Nevertheless, and in addition to the effect of SE, phenomena such as soot annealing and oxidation (Michelsen, 2003), which are often neglected in LII models (see Table A1), can also influence the signal decay rates, thus making it challenging to derive physically meaningful α_T from the simulation of pulsed-LII-temporal profiles. Since the equations representing the above-listed phenomena (i.e., shielding, annealing and oxidation, among others) are not embedded within the initial formulation of model 1, Eq. (42) may thus have integrated the effect of these complementary processes through the fitting procedure between measured and simulated time decays. This is why it is reiterated that the calculations proposed above only aimed at providing insights into how to parameterize a standard model in order to improve its predictive ability under certain conditions. Furthermore, and since simulated LII time decays are strongly influenced by the formulation and/or parameterization of the different heat transfer sub-models implemented, the focus will be on the radiation and sublimation fluxes and on their relative impact on computed signals in the following. Doing so is especially relevant as the inability of model 1 to reproduce the data from Goulay et al. (2013) could indicate that a too-simplistic treatment of some cooling mechanisms, such as sublimation, is considered, as previously suggested in Lemaire & Mobtil (2015). Before that, we still compared in Fig. 10 the signals simulated by means of model 2, with the time decays measured at 50 mm HAB in the C_2H_4 flame with an EW of 532 nm (data obtained at 1064 nm in the C_2H_4 and $CH_4/O_2/N_2$ flames not reported for brevity). Actually, we did not expend too much effort on trying to reproduce the LII time decays measured by Goulay et al. (2013) and Bejaoui et al. (2015) with model 2 since we demonstrated in section 5.1.1 that the latter integrates an ill-adapted formulation of the rate of change of the particle internal energy. That being said, and while confirming the main trends previously highlighted with model 1 as far as the effect of α_T on the decay rates is concerned, the curves plotted in Fig. 10 also demonstrate that model 2 fails to reproduce measured signals, regardless of the selected thermal accommodation coefficient.

As far as the influence of $\dot{Q}_{rad}$ on modeled LII time decays is concerned, it is quite low due to the marginal contribution of the radiation flux to the energy balance equation (see Fig. 6). This notably explains why $\dot{Q}_{rad}$ is often neglected in LII models, as previously mentioned in section 5.1.1 and exemplified in Table A1. The actual effect of $\dot{Q}_{rad}$ on computed signals has, however, seldom been quantified in modeling studies in which this flux is neglected. As a consequence, and in a bid to draw a clear-cut conclusion regarding the relative importance of the radiation flux, we estimated the mean relative deviation (MRD) between LII signals simulated with model 1 while considering or neglecting the radiation flux. To that end, simulations were conducted for each investigated EW and HAB of the C_2H_4 and $CH_4/O_2/N_2$ flames while considering the different fluences reported in the captions of Figs. 8 and 9. For calculation purposes, the $E(m)$ estimated in section 5.1.1 were considered together with the surface-temperature and gas-temperature-dependent

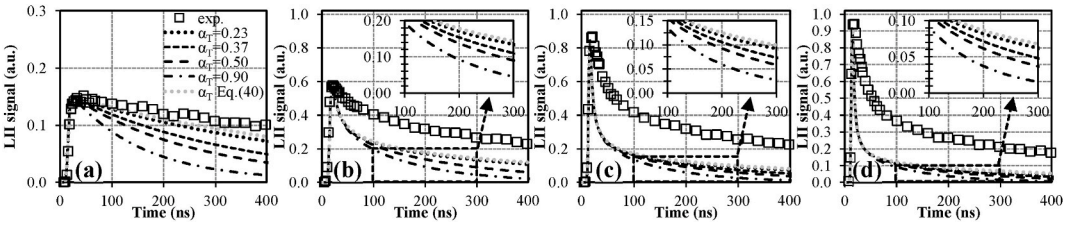

Fig. 10. Comparison of LII time decays simulated using model 2 with their experimental counterparts (referred to as "exp.") measured at 50 mm HAB in the C_2H_4 diffusion flame with an EW of 532 with fluences of 0.040 J cm^{-2} (**a**), 0.069 J cm^{-2} (**b**), 0.100 J cm^{-2} (**c**), 0.124 J cm^{-2} (**d**). Calculations were performed by setting the $E(m)$ to 0.49, while α_T was parameterized as detailed in the legend of (**a**), which also applies to the other subfigures. Note that the insets correspond to a zoom-in on the time domain extending from 100 to 300 ns to better highlight the effect of α_T on simulated LII time decays.

α_T derived from Eq. (40) (similar trends being obtained regardless of the selected α_T anyway, as verified by complementary calculations not detailed herein). Finally, the differences between the time decays simulated considering or neglecting $\dot{Q}_{rad}$ were estimated every ns for 0 ns $< t <$ 500 ns, before being averaged. Doing so led to the conclusion that neglecting the radiation flux induces a mean relative deviation in simulated LII time decays of less than 1.5 %. It is further noteworthy that repeating the same procedure with model 2 led to a very similar result with an MRD of 1.6 %. Although not being completely negligible, these low deviations still confirm that the contribution of $\dot{Q}_{rad}$ to heat loss is relatively limited in the conditions investigated herein (i.e., atmospheric flames). Caution should nonetheless be exercised when implementing standard model formulations with a view to evaluating the soot size by TiRe-LII. The non-inclusion of the radiation flux in this context can indeed induce non-negligible errors in the inferred soot diameters. To exemplify this statement, we simulated the LII time decay measured at 50 mm HAB in the C_2H_4 flame by means of model 1 while integrating or suppressing $\dot{Q}_{rad}$ from the energy balance equation. The calculations were performed considering a fluence of 0.04 J cm^{-2} and an EW of 532 nm, as these conditions were found to lead to the highest deviation between the theoretical signals computed with or without considering radiation ($\sim$3.1 % on average). In doing so, we found that D_p should be set to $\sim$30.5 nm when neglecting $\dot{Q}_{rad}$ to obtain a time decay identical to the one issued from the calculation performed while integrating the radiation flux and setting D_p to 33 nm as suggested by Goulay et al. (2013). This hence shows that suppressing the radiation flux from the energy balance equation may lead to an error of 7.6 % in the inferred soot diameter (as against 8.3 % when considering model 2). Although the least favorable conditions were considered in performing this test, the results obtained still show that deriving soot diameters from the implementation of simplified LII models in which $\dot{Q}_{rad}$ is neglected should be done with caution (especially at low fluences), depending on the operating conditions.

Finally, the influence of the mass accommodation coefficient on LII fluence curves and time decays simulated by means of models 1 and 2 is illustrated in Fig. 11. To obtain the plots reported therein, the α_M was set to values comprised between 0.1 as done by Bejaoui et al. (2015), and 1, which corresponds to the value selected by Melton (1984) and Hofmann, Kock, & Schulz (2007). An intermediate α_M of 0.50, notably considered by Hadef in Michelsen et al. (2007), was, moreover, also tested in addition to the default value of 0.8 defined in section 4.1.3. Of note, only the results obtained for a HAB of 15 mm in the $CH_4/O_2/N_2$ are depicted in Fig. 11 as an example. Similar trends can, however, be observed when processing the data obtained at 9 mm HAB in the same flame or at 50 mm HAB in the C_2H_4 flame. As can be seen from Fig. 11c and f, decreasing the mass accommodation coefficient while setting the $E(m)$ to the values previously inferred in section 5.1.1 (i.e., $\sim$0.43 for model 1 and $\sim$0.46 for model 2) induces a reduction of the sublimation flux, which in turn leads to the computation of longer decay times. Although it would be beneficial to slightly improve the agreement between simulated and measured signals for 50 ns $< t <$ 250 ns, the reduction of α_M alternatively worsens the ability of the models to reproduce the experimental fluence curves at lower fluences, as exemplified in Fig. 11a and d. This notably explains why the peak of the LII signals are not correctly captured by the models in Fig. 11b and e when α_M is set to 0.1. Properly mimicking the fluence dependence of the peak signals with model 1 then requires increasing the soot absorption function to 0.44 and 0.55 for α_M of 0.5 and 0.1 versus 0.47 and 0.53 when considering model 2. One can, however, note that the time decays computed while integrating these alternative soot absorption functions match the curves issued from calculations performed with a mass accommodation coefficient of 0.8 and $E(m)$ of 0.43 (see Fig. 11b and c) and 0.46 (see Fig. 11e and f). Reducing the α_M value while adjusting the $E(m)$ with a view to properly reproducing the increasing section of the fluence curves does not thus allow to improve the agreement between measured and simulated LII time decays. Doing so only leads to infer soot absorption functions $\geq$0.44, which is physically inconsistent as the $E(m)$ of

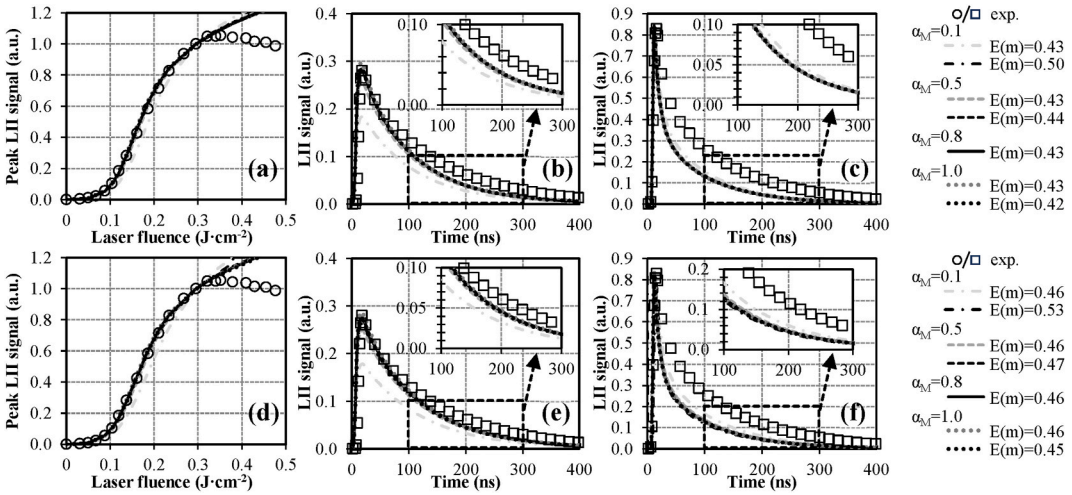

Fig. 11. Comparison of LII fluence curves ((**a**) and (**d**)) and time decays ((**b**), (**c**), (**e**) and (**f**)) simulated using models 1 ((**a**), (**b**) and (**c**)) and 2 ((**d**), (**e**) and (**f**)) with their experimental counterparts (referred to as "exp.") measured at 15 mm HAB in the $CH_4/O_2/N_2$ premixed flat flame. Fluences of 0.138 J cm^{-2} ((**b**) and (**c**)) and 0.234 J cm^{-2} ((**e**) and (**f**)) were considered in plotting the LII time decays. Furthermore, calculations were carried out using $E(m)$ values of 0.43 ((**a**), (**b**) and (**c**)) and 0.46 ((**d**), (**e**) and (**f**)), α_T set to 0.37 and α_M parameterized as detailed in the graph legends.

freshly emitted and mature soot is expected to fall between 0.35 and 0.45 according to Liu et al. (2020) (see section 5.1.1). Finally, increasing the α_M from 0.8 to 1 has a very limited impact on obtained results as can be seen by looking at the fluence curves and time decays plotted in dashed lines in Fig. 11. It nevertheless still allows to estimate somewhat lower $E(m)$ of 0.42 and 0.45 for models 1 and 2, respectively, although the agreement between measured and simulated peak soot temperature profiles is slightly worsened in this case due to an underprediction of T_p by the models (corresponding plots not reported for brevity).

5.1.3. Summary of highlighted trends and discussion

As illustrated above, standard LII models are relatively straightforward to implement as they integrate a relatively limited number of mechanisms representing heating by absorption and cooling by radiation, sublimation and conduction. In turn, their use only invovles defining a few input parameters, mainly including ρ_s, c_s, $E(m)$, α_T and α_M. This thus makes them "easy-to-tune" simulation tools for reproducing experimentally monitored LII signals. Furthermore, they can be easily refined by integrating corrective factors to account for the shielding effect (Snelling et al., 2004) and/or multiple scattering (MS) within aggregates (Yon et al., 2014, 2015), as examples. These attractive features particularly explain why this type of model formulation has been widely employed in the past decades, as illustrated in Table A1, noting that the open-source software proposed by Mansmann et al. (2018) (LIISim) is especially built upon standard heat transfer models from the literature. That said, the relatively poor predictive capability of standard models can be isolated as representing a major issue needing to be addressed. In this context, the results detailed in sections 5.1.1 and **5.1.2** mainly show that neither one of the model formulations tested was able to properly simulate the experimental datasets from Goulay et al. (2013) and Bejaoui et al. (2015) on extended ranges of operating conditions. More specifically, and although adequately reproducing the measured fluence curves in the low-to-intermediate fluence regime when being properly parameterized, models 1 and 2 still failed to simulate the fluence dependence of the peak LII signals above the sublimation threshold. Furthermore, the detailed sensitivity analyses proposed in the present work showed that none of the considered parameterizations truly allow to obtain modeled signals matching measured ones for fluences between 0 and 0.5 J cm^{-2}, which is in line with the conclusion previously drawn by Lemaire & Mobtil (2015), who used inverse techniques to analyze the predictive capability of a Melton-based model.

That being said, and in a more general perspective, it is noteworthy that the inability of standard models to properly simulate LII signals at relatively high fluences may prevent them from being used to gain insights into the effects of factors, such as the polydispersity of primary particles, for instance, on the variations observed when performing LII-assisted soot volume fraction measurements at high fluences. Actually, the underlying reason for the approximate proportionality between peak LII signals and soot volume fractions is that soot particles behave like volume absorbers and emitters. As a consequence, if all the particles reach the maximum signal for the same peak temperature (corresponding to the sublimation point), the peak signal will then correlate with the volume of the particles. This notably explains why high laser fluences (for which pulsed-LII signals appear independent of the laser fluence) are often used to assess soot volume fractions in practical combustion media (Michelsen et al., 2015), although the implementation of the low-fluence auto-compensating approach proposed by Snelling et al. (2005) can still be regarded as a more convenient option. That said, the inability of standard models to capture the physics at play during LII measurements carried out at high fluences thus represents a limitation when information on soot is to be derived from the modeling of LII signals collected using operating conditions typically set for soot volume fraction assessment in practical situations where laser attenuation is substantial and/or difficult to assess due to strong spatial fluctuations of the soot distribution. On the other hand, the models tested in the present comparison analysis were found to correctly reproduce measured fluence curves below the sublimation threshold. This can thus be of interest for TiRe-LII applications for which low fluences are preferable to avoid the complications of sublimation and large changes in particle size during the laser pulse. Nevertheless, and here again, predicted time decays significantly diverging from their experimental counterparts were computed, especially in the case of the C_2H_4 flame. The implementation of an optimization procedure aimed at reducing the least square error between the time decays measured in the $CH_4/O_2/N_2$ flame and the predictions from model 1 still led to infer a surface-temperature and gas-temperature-dependent expression of α_T (see Eq. (41)) whose use allowed to improve the agreement between theoretical and experimental signals for fluences between $\sim$0.1 and $\sim$0.2 J cm^{-2}. It is, however, reiterated that such a procedure should be considered with caution as it intrinsically treats the thermal accommodation coefficient as a free-floating calibration parameter somewhat detached from its original physical meaning. Furthermore, the validity of Eq. (41) may have been biased by the too-simplistic treatment of some cooling mechanisms (e.g., sublimation) as well as by the existence of ill-defined factors likely to influence simulated signals. As for model 2, which globally behaves similarly to model 1 at low fluences, the incorrect formulation of the rate of soot internal energy change proposed by Hofmann, Kock, & Schulz (2007) induces physically erroneous peak particle temperatures at high laser fluences, thus showing why this model should be definitively avoided. Finally, no specific recommendation regarding the values and/or expressions of ρ_s and c_s which ought to be preferentially considered truly emerged from the results reported in section 5.1.1. Actually, $E(m)$ values globally in line with the extended range of plausible values given in Liu et al. (2020) were obtained whether implementing the soot density and heat capacity proposed by Melton (1984), Kock et al. (2006) or by Michelsen (2003, 2021) in model 1. Although higher soot absorption functions were derived from the use of the temperature-dependent expressions proposed by Michelsen (2003, 2021), the integration of the MS corrective factor from Yon et al. (2014, 2015) in $\dot{Q}_{abs}$ allowed reducing the inferred $E(m)$ below the upper limit of 0.52 reported by Liu et al. (2020). This thus suggests that it would be beneficial to explore a more refined treatment of the processes at play during LII (as will be done in section 5.2) to avoid inferring potentially erroneous soot properties.

5.2. Analysis of results obtained with refined model formulations

5.2.1. Comparison of measured LII fluence curves with modeled ones and sensitivity analysis dealing with the values taken by physical parameters driving the absorption, annealing, photodesorption and thermionic emission processes

Fig. 12 compares a series of measured fluence curves with theoretical ones issued from the implementation of model 3. Note that Eq. (29) was selected to compute the oxidation flux (a sensitivity analysis dealing with the influence of this term on modeled signals being proposed in section 5.2.2) while α_T was taken equal to 0.37 as was done in section 5.1.1. It is indeed reiterated that hypotheses regarding cooling mechanisms such as conduction are not of concern at this stage since the peak LII signals fundamentally depend on fluxes whose influence is significant at the very beginning of the LII process (i.e., essentially during the laser pulse duration), which is not the case with $\dot{Q}_{cond}$ or $\dot{Q}_{ox}$. As for the parameters influencing fluence curves, they mainly comprise the soot absorption functions of unannealed and annealed soot fractions ($E(m)$ and $E_a(m)$, set to 0.286 and 0.238, respectively, in Michelsen (2003)). Furthermore, and although contributing to soot cooling, sublimation can still compete with absorption over the laser pulse duration when high laser fluences are used (a point further illustrated below). The values taken by the cross-sections for the photodesorption of carbon clusters and the enthalpy of formation of C_j clusters by photodesorption from unannealed and annealed soot fractions thus also influence the shape of the fluence curves. In her 2003 work, Michelsen (2003) considered that the cross-section for removal of C_2 clusters from annealed soot ($\sigma_{\lambda a}$) and C_1–C_3 clusters from unannealed particles ($\sigma_{\lambda s}$) were identical. They were empirically adjusted to 1×10^{16} cm^{-1} s^{-1} for best agreement with the LII signals collected in a laminar ethene diffusion flame over a wide range of laser fluences at 532 nm (Michelsen et al., 2003). Similarly, the energy required to remove C_2 from the annealed ($\Delta H_{\lambda a}$) and unannealed ($\Delta H_{\lambda s}$) soot fractions by nonthermal photodesorption (estimated from carbon cluster binding energies inferred from Ne ion sputtering of graphite) were set so that $\Delta H_{\lambda i} = \Delta H_{\lambda a} = \Delta H_{\lambda s} = 3.4 \times 10^5$ J mol^{-1}. These parameters, however, fail to properly reproduce the fluence curve measured by Goulay et al. (2013) using an identical EW of 532 nm, as exemplified by the light gray curve plotted in Fig. 12a. Computed data indeed underpredicts the LII response for fluences below 0.15 J cm^{-2} while conversely overpredicting it above that level. Even while increasing the $E(m)$ to 0.42 to minimize the least square sum between measured and simulated results below 0.15 J cm^{-2} (data not reported in Fig. 12a for clarity), the model still predicts continuously increasingly peak LII signals that significantly overpredict measured data at higher fluences. Adjusted values for $E(m)$, $E_a(m)$, $\sigma_{\lambda i}$ and $\Delta H_{\lambda i}$ were therefore proposed by implementing the optimization procedure previously described in section 5.1. This led to obtaining the results reported in Table 4, where $\sigma_{\lambda i}$ stands for both $\sigma_{\lambda a}$ and $\sigma_{\lambda s}$, which are taken equal as stated above, as is the case of $\Delta H_{\lambda i}$, which represents the energy required to remove C_2 from both annealed ($\Delta H_{\lambda a}$) and unannealed ($\Delta H_{\lambda s}$) soot. Note also that since Michelsen then considered that only C_2 was produced by photolysis (Michelsen et al., 2007), no effort was thus expended on trying to adjust the $\Delta H_{\lambda s}$ values corresponding to C_1 and C_3 clusters, which were hence set as proposed in Michelsen (2003). One should therefore note that the $\Delta H_{\lambda i}$ values which are varied below only relate to C_2 clusters. Finally, and to better highlight the impact of the above parameters on the variations of the peak LII signals as a function of the laser fluence, the $E(m)$, $E_a(m)$, $\sigma_{\lambda i}$ and $\Delta H_{\lambda i}$ values were varied as detailed in the legends of Figs. 12 and 16. To that end, $E(m)$ comprised between 0.29 and 0.52 were considered according to the likely range of values recommended by Liu et al. (2020). Regarding $E_a(m)$, a lower limit of 0.13 was selected, which corresponds to the soot absorption function that can be inferred by extrapolating the line-of-sight attenuation-based results from Saffaripour et al. (2015) for a 1064 nm EW (see Fig. 4 in Sipkens et al. (2019)). Finally, the lower and upper bounds for $\sigma_{\lambda i}$ and $\Delta H_{\lambda i}$ were defined by dividing or multiplying the optimized values from Table 4 by a given factor (set to 2 in the case of $\Delta H_{\lambda i}$ in Fig. 16, for instance) to obtain limit values allowing to clearly exemplify the effect of these parameters on peak LII signals.

As can be seen by looking at the full black lines plotted in Fig. 12, using the parameters listed in Table 4 allows obtaining computed signals which closely match their experimental counterparts. Contrary to what was observed with the standard model formulations tested in section 5.1, model 3 clearly captures the lack of fluence dependence in peak LII signals above the sublimation threshold. Slight deviations between measured and simulated results can still be observed above 0.35 J cm^{-2} in Fig. 12d, although it is rather difficult to distinguish the extent to which such discrepancies stand from improper model predictions or experimental uncertainties. As for the

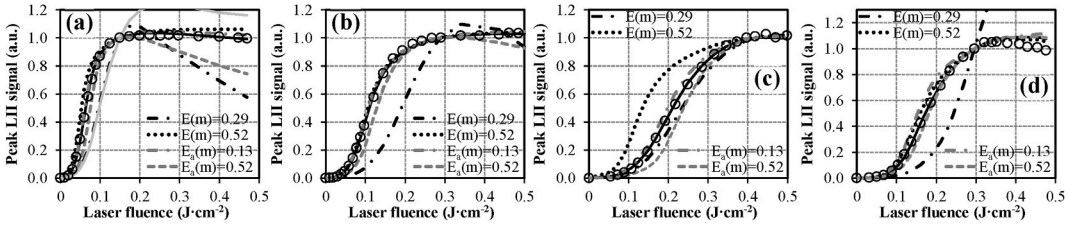

Fig. 12. Comparison of LII fluence curves simulated using model 3 (lines) with experimental results (depicted via circles) measured at 50 mm HAB in the C_2H_4 diffusion flame using EWs of 532 (**a**) and 1064 nm (**b**), as well as with the data collected with an EW of 1064 nm at 9 (**c**) and 15 mm HAB (**d**) in the $CH_4/O_2/N_2$ premixed flat flame. Calculations were performed using the optimized parameters listed in Table 4, setting the α_T to 0.37, while computing the oxidation term using Eq. (29) (corresponding results being plotted with a full black line). The light gray full line in (**a**) represents the simulated results obtained while parameterizing $E(m)$, $E_a(m)$, $\sigma_{\lambda i}$ and $\Delta H_{\lambda i}$ in model 3 as proposed by Michelsen (2003). For their part, the other curves correspond to simulated results obtained while varying the absorption properties of soot as detailed in the legend of each subfigure. Note that when $E(m)$ or $E_a(m)$ values are specified in the chart legends, this indicates that these specific soot absorption functions were used instead of those reported in Table 4, while the other parameters were kept as detailed therein.

Table 4
$E(m)$, $E_a(m)$, $\sigma_{\lambda i}$ and $\Delta H_{\lambda i}$ values allowing to obtain the best fit between experimental fluence curves issued from the works of Goulay et al. (2013) and Bejaoui et al. (2015) and simulation results obtained from model 3.

Flame	EW/HAB	$E(m)$ (−)	$E_a(m)$ (−)	$\sigma_{\lambda i}$ (cm^{-1} s^{-1})	$\Delta H_{\lambda i}$ (J mol^{-1})
C_2H_4 (Goulay et al., 2013)	532 nm/50 mm	0.43	0.21	$10^{16.50}$	2.90×10^5
	1064 nm/50 mm	0.50	0.23	$10^{16.20}$	2.00×10^5
$CH_4/O_2/N_2$ (Bejaoui et al., 2015)	1064 nm/9 mm	0.32	0.20	$10^{16.40}$	2.00×10^5
	1064 nm/15 mm	0.48	0.34	$10^{16.44}$	2.00×10^5

effect of $E(m)$, increasing its value to 0.52 takes the fluence above which the peak LII signals tend to plateau to be shifted to lower values. This is actually in line with expectations, since the higher the $E(m)$, the greater the absorption of the laser energy, and the sooner the sublimation temperature is reached. This leads to the intensity of the peak LII signals becoming relatively constant, notably

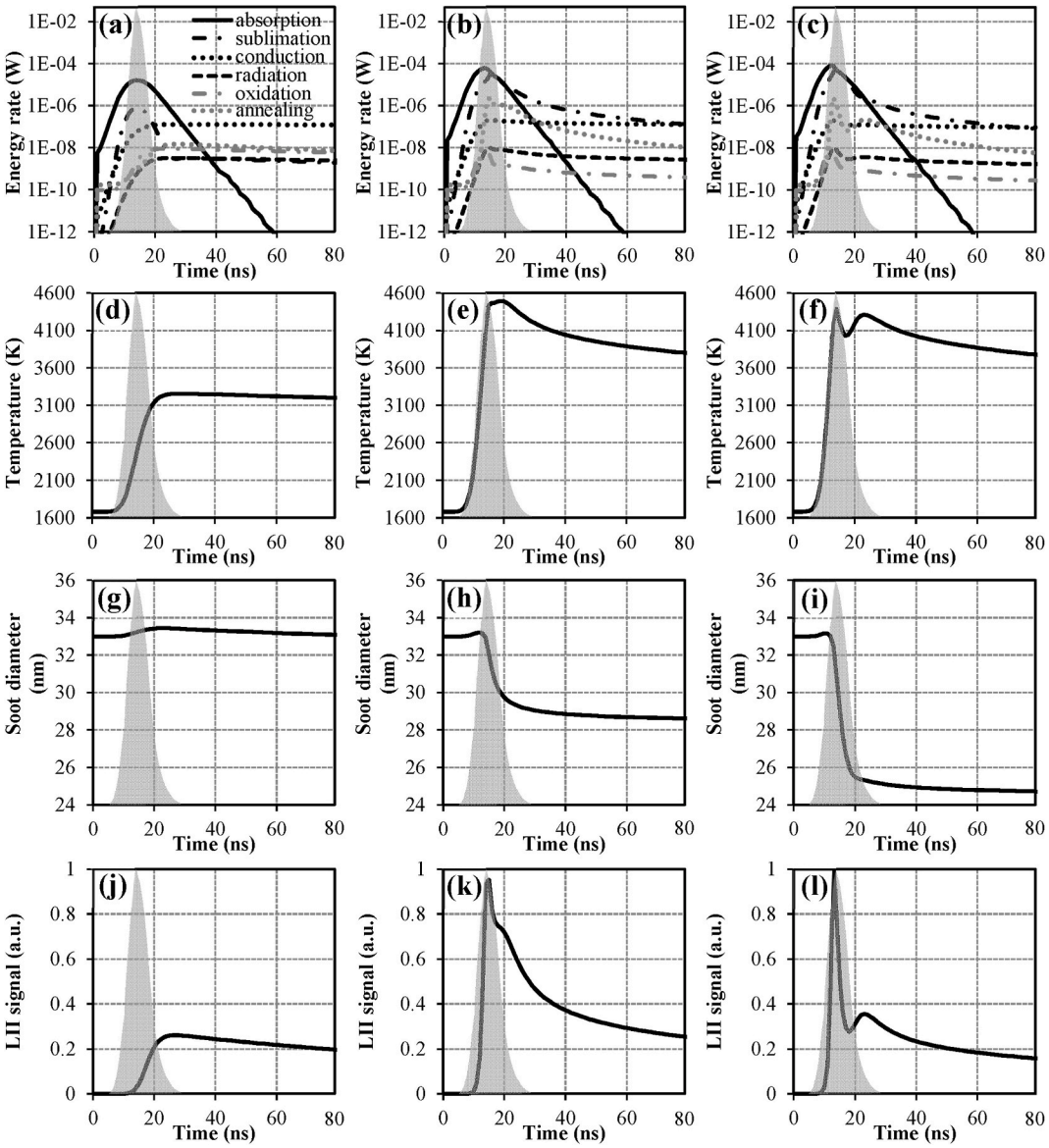

Fig. 13. Temporal evolution of the energy transfer rates ((**a**), (**b**) and (**c**)), soot temperatures ((**d**), (**e**) and (**f**)), soot diameters ((**g**), (**h**) and (**i**)) and LII time decays ((**j**), (**k**) and (**l**)) computed using model 3 to simulate the data collected by Goulay et al. (2013) at 50 mm HAB in the C_2H_4 diffusion flame, using an EW of 532 nm. Note that calculations were performed using the optimized parameters listed in Table 4, considering fluences of 0.05 J cm^{-2} ((**a**), (**d**), (**g**) and (**j**)), 0.20 J cm^{-2} ((**b**), (**e**), (**h**) and (**k**)) and 0.30 J cm^{-2} ((**c**), (**f**), (**i**) and (**l**)). Note also that the gray areas in each figure denote the temporal profiles of the laser pulses used by Goulay et al. (2013).

due to a competition between $\dot{Q}_{abs}$ and $\dot{Q}_{sub}$, as further discussed below. On the other hand, and as can be seen by looking at Fig. 12a as an example, the increasing section of the peak LII profile is shifted to higher fluences when the $E(m)$ is set to 0.29. The signal intensity then decreases significantly after reaching a maximum value at around 0.19 J cm^{-2}. This specific behavior can be explained by analyzing and comparing the temporal evolution of the energy fluxes computed while decreasing the $E(m)$ from 0.43 (see Fig. 13) to 0.29 (see Fig. 14). Fig. 13a indeed shows that the rise of the soot temperature is predominantly controlled by the absorptive-heating flux during the laser pulse duration when a low laser fluence of 0.05 J cm^{-2} is considered. $\dot{Q}_{sub}$ is then much smaller than $\dot{Q}_{abs}$, which leads to T_p (see Fig. 13d) staying well below the sublimation threshold (around 4400 K, according to Goulay et al. (2013)). Consequently, D_p (see Fig. 13g) does not decrease, and even rises slightly during the laser pulse due to the use of the temperature-dependent expression of ρ_s depicted in Eq. (6). Alternatively, $\dot{Q}_{abs}$ exceeds $\dot{Q}_{sub}$ only during the first 16 ns and 14 ns following the beginning of the laser excitation when higher fluences of 0.20 (see Fig. 13b, **e**, **h** and **k**) and 0.30 J cm^{-2} (see Fig. 13c, **f**, **i** and **l**) are used, respectively, whereupon $\dot{Q}_{sub}$ becomes the predominant energy flux. The peak temperature is thus reached after the laser pulse at 0.20 J cm^{-2} (see

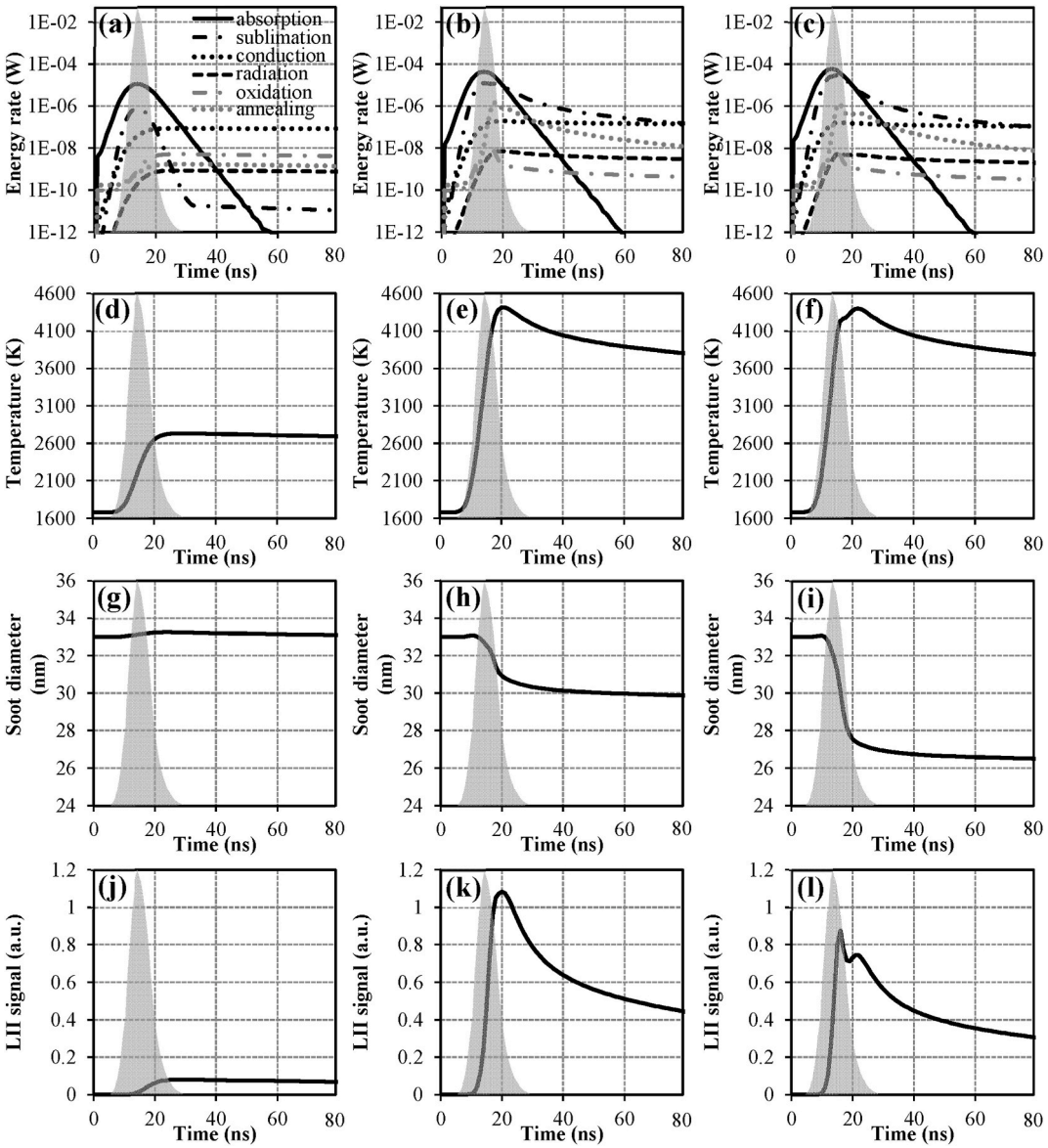

Fig. 14. Temporal evolution of the energy transfer rates ((**a**), (**b**) and (**c**)), soot temperatures ((**d**), (**e**) and (**f**)), soot diameters ((**g**), (**h**) and (**i**)) and LII time decays ((**j**), (**k**) and (**l**)) computed with model 3 to simulate the data collected by Goulay et al. (2013) at 50 mm HAB in the C_2H_4 diffusion flame, using an EW of 532 nm. Note that calculations were performed using the optimized parameters listed in Table 4, with the exception of $E(m)$, which was set to 0.29, considering fluences of 0.05 J cm^{-2} ((**a**), (**d**), (**g**) and (**j**)), 0.20 J cm^{-2} ((**b**), (**e**), (**h**) and (**k**)) and 0.30 J cm^{-2} ((**c**), (**f**), (**i**) and (**l**)). Note also that the gray areas in each figure denote the temporal profiles of the laser pulses used by Goulay et al. (2013).

Fig. 13e) when D_p already decreased significantly (see Fig. 13h). Conversely, the peak of T_p, which is slightly lower at 0.30 J cm^{-2}, is reached immediately after the first photons of the laser are emitted, the decrease of D_p then being insignificant (see Fig. 13f and i). As a result of this competition between absorption and sublimation, the peak intensity of the LII signals (which fundamentally depends on D_p and T_p, whose variations as a function of time tend to compensate each other) undergoes no further significant change above 0.12 J cm^{-2} (see Figs. 12 and 13k and l), although it is recorded earlier as the laser fluence increases. Note also that the signal time decays become much faster when the fluence passes from 0.05 to 0.30 J cm^{-2} due to the sublimation of the particles, which becomes much more intense while being shifted to shorter times. The specific formulation of $\dot{Q}_{sub}$ proposed by Michelsen (2003) and the above-described competition between absorption and sublimation thus explain why model 3 allows to reproduce the so-called plateau region of the fluence curves, whereas models 1 and 2 clearly failed to do so (see section 5.1.1). Besides, it is noteworthy that the predicted temperature and LII signal profiles in Fig. 13f and l exhibit two distinct peaks when high laser fluences are used. This specific phenomenon, also reported in Michelsen (2003), stems from the formulation of the annealing flux (see section 4.1.6), whose temporal evolution (see Fig. 13c) is characterized by a first peak occurring during the laser pulse duration and a second one observed ~10 ns later, which can be traced to the contribution of vacancy migration, as suggested by the fact that neglecting this mechanism leads to the disappearance of the second peak. Regarding the plots of Fig. 14, they mainly show that decreasing the $E(m)$ to 0.29 reduces the absorption rate while shifting the peak of $\dot{Q}_{abs}$ to longer times (see Fig. 14a, **b** and **c**) as compared to the results reported in Fig. 13. At high fluences (see Fig. 14e and f), the peak of T_p is especially reached after the laser pulse duration when D_p already significantly decreased due to sublimation (see Fig. 14h and i). As a consequence, while reaching relatively similar peak T_p values at 0.20 (see Fig. 14e) and 0.30 J cm^{-2} (see Fig. 14f), D_p is significantly lower in the latter case, which results in a lower peak LII signal, as can be seen by looking at Fig. 14k and l. All these observations thus allow explaining the impact of the soot absorption function on the shape of the fluence curves reported in Fig. 12, noting that, although not detailed by means of additional graphs, the above analysis, of course, also applies to the interpretation of the results observed at 1064 nm in both the C_2H_4 and $CH_4/O_2/N_2$ flames.

As for $E_a(m)$, the analysis of the temporal evolution of the energy transfer rates (not reported for brevity) indicates that increasing $E_a(m)$ logically increases the amount of energy absorbed by the annealed fraction of soot, which translates into higher peak T_p values. At the same time, the particles sublime more readily as a result of this higher heating, which induces stronger D_p reductions, and consequently, lower peak LII signals, as shown in Fig. 12. This trend is, however, opposite to that observed when increasing $E(m)$, which can be partly traced to the fact that soot annealing takes place over a certain period of time, as illustrated in Michelsen (2003). The annealed fraction notably starts to increase rapidly a few ns after the beginning of the laser pulse (~8 ns for a fluence of 0.30 J cm^{-2} at 532 nm, considering a $E_a(m)$ of 0.52 as an example). Since annealing is exothermic, the peak temperature of the particles is thus computed for longer durations (for which D_p already significantly decreased) when the contribution of the annealing process is enhanced. This thus explains why increasing $E_a(m)$ reduces the peak LII response, contrary to what was observed when increasing $E(m)$, which conversely shifted the peak soot temperature to shorter times for which the D_p reduction was still limited. Ultimately, the very subtle balance between the contributions of $\dot{Q}_{abs}$, $\dot{Q}_{sub}$ and $\dot{Q}_{ann}$, whose variations as a function of time and fluence are quite distinct, here again, evidence the significance of parameterizing LII models through the implementation of optimization procedures aimed at minimizing the deviation between experimental and numerical data over the whole duration of the soot heating and cooling stages, considering wide varying laser fluences, as proposed in Lemaire & Menanteau (2021, 2023a). When further examining the soot absorption functions reported in Table 4, it is noteworthy that $E_a(m)$ lower than $E(m)$ were derived although it could have been expected that the more annealed (and thus the more graphitized) the soot, the higher its absorption function would be. Vander Wal et al. (1998) indeed showed that the intensity of LII signals issued from soot preheated by laser pulses at 1064 nm, and having fluences around ~0.1 J cm^{-2}, was enhanced, thus possibly indicating that graphitized particles exhibit higher absorption and emission features. They alternatively observed the opposite at higher fluences, thus illustrating how difficult it is to draw a clear-cut conclusion on the matter. More recently, López-Yglesias, Schrader, & Michelsen (2014) modeled a series of LII signals collected in co-flow diffusion flames of ethylene. To that end, they implemented a refined model integrating a soot absorption function defined by $E(m) = \lambda^{1-\xi} \cdot \beta / 6 \cdot \pi$, where the dispersion exponent ξ accounts for the maturity of both unannealed and annealed soot. Using this expression, $E(m)$ and $E_a(m)$ values of 0.43 and 0.45, respectively, can be computed for an EW of 532 nm and a temperature of 1676 K, which corresponds to the one measured by Goulay et al. (2013) at 50 mm HAB in the ethylene flame studied herein (see section 3). Obtained values thus tend to corroborate the fact that the more graphitized the particles, the higher their absorption properties. In a subsequent work, Saffaripour et al. (2015) reported a rapid enhancement of the extinction coefficient of soot during laser heating in premixed and diffusion flames of ethylene. This trend was notably traced to an increase of the temperature-dependent optical properties of soot due to laser-induced thermal annealing. A similar observation was finally drawn by Cenker & Roberts (2017) during two-pulse LII experiments, although the modeling of the results they obtained (considering the equations proposed by Michelsen (2003) to account for the annealing process) conversely suggested that the graphitization of laser-heated particles induced a reduction of their absorption and emissivity characteristics. This latter observation still agrees with the early work by Michelsen (2003), who developed the first known annealing sub-model used by the LII community, in which it was considered that $E_a(m) < E(m)$, based on a review of past studies from the literature dealing with soot and graphite. Furthermore, the modeling results from Cenker & Roberts (2017) also confirm the validity of the calculations made herein, as evidenced by the fact that implementing the same annealing model leads to similar conclusions regarding the higher absorption properties of unannealed soot over annealed ones. That $E_a(m)$ lower than $E(m)$ are derived when using model 3, contrary to the experimental observations by Saffaripour et al. (2015) and Cenker & Roberts (2017), however, prompts the need for commentary analyses to rule on the overall consistency of the annealing sub-model proposed by Michelsen (2003). This is further validated by the fact that the implementation of the equations detailed in section 4.1.6 leads to the computation of temperature and LII signal profiles exhibiting two peaks at high fluences (see Fig. 13f and l, for instance), which are probably

nonphysical since they were not experimentally observed by Goulay et al. (2013) and Bejaoui et al. (2015) on the range of fluences considered in this work. Alternative formulations of $\dot{Q}_{ann}$ will therefore be explored in section 5.2.3 for completeness. On the other hand, and contrary to the $E(m)$ inferred in the case of the C_2H_4 flame when implementing Eqs. (6) and (7) in models 1 and 2 (see Table 3), which mainly fell outside of the more likely range of values from Liu et al. (2020), the soot absorption functions derived from the calculations performed with model 3 (see Table 4) allows to obtain more consistent optical properties (i.e., below 0.52), which thus represents an interesting feature of this refined simulation tool. Besides, and although still being comprised within the more likely range of values, higher $E(m)$ are alternatively estimated when processing the data from Bejaoui et al. (2015) using the refined model from Michelsen (2003) instead of standard ones. A quick analysis of the different fluxes integrated in the energy and mass balance equations of model 3 actually shows that for a given LII response, and quite similar soot temperature levels, higher X_a values are computed when considering the small diameter particles formed in the methane flame. This hence leads to the optimizer increasing the absorption function of the unannealed soot fraction to compensate for the low absorption propensity of the annealed one while still fulfilling the energy and mass balances leading to the computation of simulated signals reproducing their experimental counterparts. Finally, in Fig. 15, we plot the temperature profiles computed while parameterizing model 3, as we did to obtain the graphs reported in Fig. 12. The results obtained then show that the optimized parameters summarized in Table 4 (previously shown to be adapted to simulate the fluence curves reported in Fig. 12) also allow to reproduce the temperature profiles reported Fig. 15a and b. They however fail to capture the fluence dependence of the peak T_p values measured by Bejaoui et al. (2015), especially below ~ 0.30 J cm^{-2} at 9 mm HAB (see Fig. 15c) and above ~ 0.20 J cm^{-2} at 15 mm HAB (see Fig. 15d). Nevertheless, setting the $E(m)$ value to ~ 0.36 at 9 mm HAB, as an example, could still represent an acceptable option in order to roughly reproduce both the LII fluence curve and soot temperature profile, reiterating that the existence of uncertainties encompassing either measured temperatures, LII signals, or both, cannot be fully excluded (see section 5.1.1). As for the light gray full line depicted in Fig. 15a, it confirms that the parameters initially proposed in Michelsen (2003) do not allow reproducing the experimental data from Goulay et al. (2013), while the other curves reported in Fig. 15a–d shows, in line with expectations, that the higher the $E(m)$ and $E_a(m)$, the greater the absorption of the laser energy and the higher the peak particle temperatures.

To conclude the analysis of the results obtained with model 3, Fig. 16 reports the fluence curves computed using the optimized absorption functions reported in Table 4 while varying $\sigma_{\lambda i}$ and $\Delta H_{\lambda i}$, as depicted in the chart legends. Contrary to what was observed for the soot absorption function, whose impact was significant over the whole range of fluences considered to plot the graphs in Fig. 12, the values taken by the energy required to remove C_2 clusters by nonthermal photodesorption mainly influence the plateau region of the fluence curves, which is consistent with the fact that this parameter acts on the sublimation flux. Furthermore, a quick analysis of the temporal evolution of the energy transfer rates (not reported for brevity) globally shows that increasing $\sigma_{\lambda i}$ tends to shift the peak T_p values to times t for which D_p already decreased significantly, hence resulting in lower LII signals at high fluences, as exemplified in Fig. 16. As for $\Delta H_{\lambda i}$, reducing its value translates into higher T_p and lower D_p for the laser pulse duration. Nevertheless, the above-discussed competition between $\dot{Q}_{abs}$, $\dot{Q}_{sub}$ and $\dot{Q}_{ann}$ leads to the peak temperature being reached sooner, while the D_p reduction is still limited. This thus explains why higher LII responses are computed when $\Delta H_{\lambda i}$ is decreased, as can be seen when comparing the gray dotted and gray dot-dash lines in Fig. 16.

Regarding model 4, we already conducted sensitivity analyses focusing on the main parameters influencing the theoretical signals issued from its implementation in Menanteau & Lemaire (2021) and Lemaire & Menanteau (2023b). Only a brief summary of the main conclusions drawn therein will thus be given below. To that end, Fig. 17 compares the fluence curves measured at 50 mm in the C_2H_4 flame (Fig. 17a–d) and 15 mm HAB in the $CH_4/O_2/N_2$ one (Fig. 17e–h) using EWs of 532-nm and 1064 nm, respectively, with simulated data obtained while varying the soot absorption function $E(m)$ (Fig. 17a and e), the cross-section for removal of C_2 clusters by photodesorption $\sigma_{\lambda n}$ (Fig. 17b and f), the saturation coefficient for multi-photon absorption $B_{\lambda n}$ (Fig. 17c and g) and the enthalpy required to photodesorb carbon clusters from unannealed soot $\Delta H_{\lambda s}$ (Fig. 17d and h). As was done for models 1 to 3, optimized parameters, whose values are summarized in Table 5, were inferred using the procedure described in section 5.1. The corresponding results, which are plotted with full black lines in Fig. 17, show that model 4, when being parameterized as detailed in Table 5, allows to

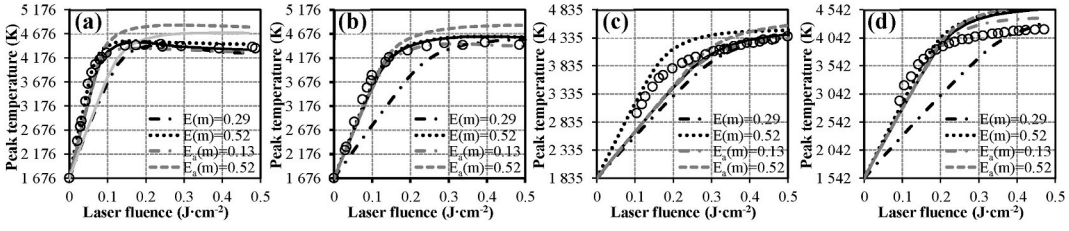

Fig. 15. Comparison of the fluence dependence of the peak soot temperature calculated using model 3 (lines) with experimental results (depicted by means of circles) measured at 50 mm HAB in the C_2H_4 diffusion flame using EWs of 532 (**a**) and 1064 nm (**b**), as well as with the data collected with an EW of 1064 nm at 9 (**c**) and 15 mm HAB (**d**) in the $CH_4/O_2/N_2$ premixed flat flame. Calculations were performed using the optimized parameters listed in Table 4, setting the α_T to 0.37, while computing the oxidation term using Eq. (29) (corresponding results being plotted with a full black line). The light gray full line in (**a**) represents the simulated results obtained when parameterizing $E(m)$, $E_a(m)$, $\sigma_{\lambda i}$ and $\Delta H_{\lambda i}$ in model 3 as proposed by Michelsen (2003). The other curves correspond for their part to simulated results obtained while varying the absorption properties of soot as detailed in the legend of each subfigure. Note that when $E(m)$ or $E_a(m)$ values are specified in the chart legends, this indicates that these specific soot absorption functions were used instead of those reported in Table 4 and that the other parameters were kept as detailed therein.

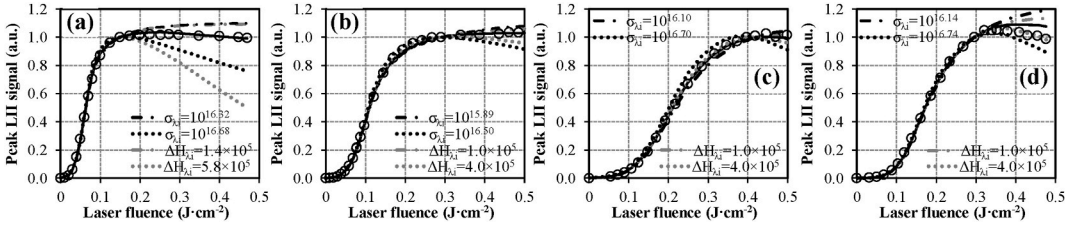

Fig. 16. Comparison of LII fluence curves simulated using model 3 (lines) with experimental results (depicted via circles) measured at 50 mm HAB in the C_2H_4 diffusion flame using EWs of 532 (**a**) and 1064 nm (**b**), as well as with the data collected with an EW of 1064 nm at 9 (**c**) and 15 mm HAB (**d**) in the $CH_4/O_2/N_2$ premixed flat flame. Calculations were performed using the optimized parameters listed in Table 4, setting the α_T to 0.37, while computing the oxidation term using Eq. (29) (corresponding results being plotted with a full black line). The other curves correspond to simulated results obtained while varying $\sigma_{\lambda i}$ and $\Delta H_{\lambda i}$ as detailed in the legend of each subfigure.

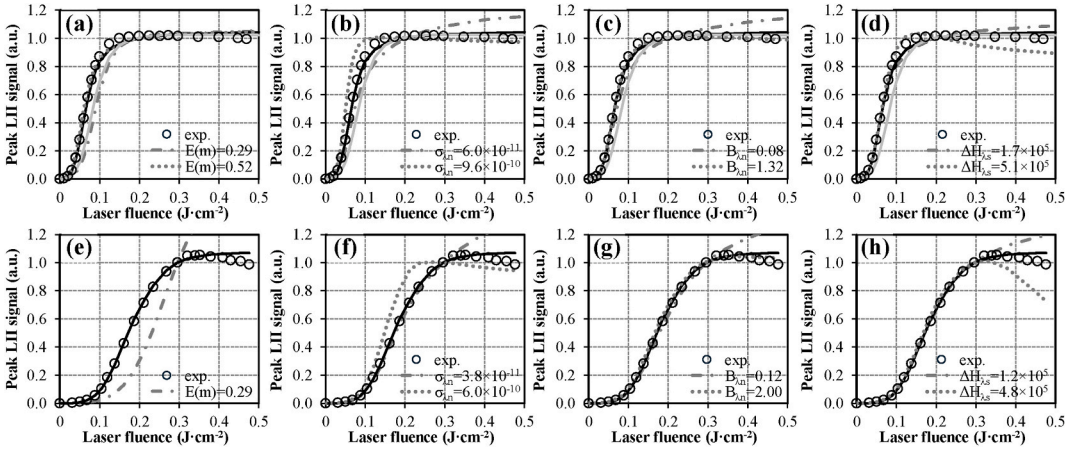

Fig. 17. Comparison of LII fluence curves simulated using model 4 (lines) with experimental results (depicted via circles) measured at 50 mm HAB in the C_2H_4 diffusion flame using an EW of 532 nm ((**a**), (**b**), (**c**) and (**d**)), as well as with the data collected with an EW of 1064 nm at 15 mm HAB ((**e**), (**f**), (**g**) and (**h**)) in the $CH_4/O_2/N_2$ premixed flat flame. Calculations were performed using the optimized parameters listed in Table 5 with $B_{\lambda 1}$ values of 0.58 and 1.15 for EWs of 532 and 1064 nm (Lemaire & Menanteau, 2023a), while computing the thermionic emission flux using Eq. (32) (corresponding results being plotted with a full black line). The light gray full lines in (**a**), (**b**), (**c**) and (**d**) represent the simulated results obtained when parameterizing model 4 exactly as proposed in Michelsen et al. (2007). The other curves correspond to simulated results obtained while varying the $E(m)$, $B_{\lambda n}$, $\sigma_{\lambda n}$ and $\Delta H_{\lambda n}$ values as detailed in the legend of each subfigure. Note that since the optimized $E(m)$ in (**e**) is 0.52 (see Table 5), one has thus to refer to the full black line to see the fluence curve obtained when setting the absorption function to such an upper limit value.

properly reproduce the experimental fluence curves, except at very high fluences, for which it tends to slightly overpredict measured data, especially in the case of the methane flame.

As shown in Fig. 18a, **b** and **c**, which depict the temporal evolution of the energy fluxes computed with model 4 for fluences between 0.05 and 0.30 J cm^{-2}, the influence of $\dot{Q}_{cond}$, $\dot{Q}_{rad}$, $\dot{Q}_{ox}$ and $\dot{Q}_{th}$ only becomes significant after the laser pulse duration in the low-to-intermediate fluence regime, while the increasing section of the LII signals is governed by the competition between $\dot{Q}_{abs}$ and $\dot{Q}_{sub}$, as was the case for the other models. Of note, the contribution of $\dot{Q}_{th}$ becomes far from negligible at high fluences (see Fig. 18b and c), and is thus likely to influence the plateau region of the fluence curves as further discussed below. The plots of Fig. 18, moreover, show that the higher the laser fluence, the higher the absorption and sublimation rates, the higher the peak soot temperature (see Fig. 18d, **e** and **f**) and the greater the shift of the absorption flux to shorter times for which D_p has not yet significantly decreased (see Fig. 18g, **h** and **i**), which therefore leads to the computation of more intense LII signals, as can be seen by comparing the plots of

Table 5
$E(m)$, $B_{\lambda n}$, $\sigma_{\lambda n}$ and $\Delta H_{\lambda n}$ values allowing to obtain the best fit between measured and computed results when implementing model 4 to simulate the data collected by Goulay et al. (2013) and Bejaoui et al. (2015).

Flame	EW/HAB	$E(m)$ (−)	$\sigma_{\lambda n}$ (cm^{2n-1} J^{1-n})	$B_{\lambda n}$ (J cm^{-2})	$\Delta H_{\lambda s}$ (J mol^{-1})
C_2H_4 (Goulay et al., 2013)	532 nm/50 mm	0.47	2.40×10^{-10}	0.33	3.40×10^5
	1064 nm/50 mm	0.55	2.00×10^{-10}	0.50	2.40×10^5
$CH_4/O_2/N_2$ (Bejaoui et al., 2015)	1064 nm/9 mm	0.37	1.10×10^{-10}	0.50	2.40×10^5
	1064 nm/15 mm	0.52	1.50×10^{-10}	0.50	2.40×10^5

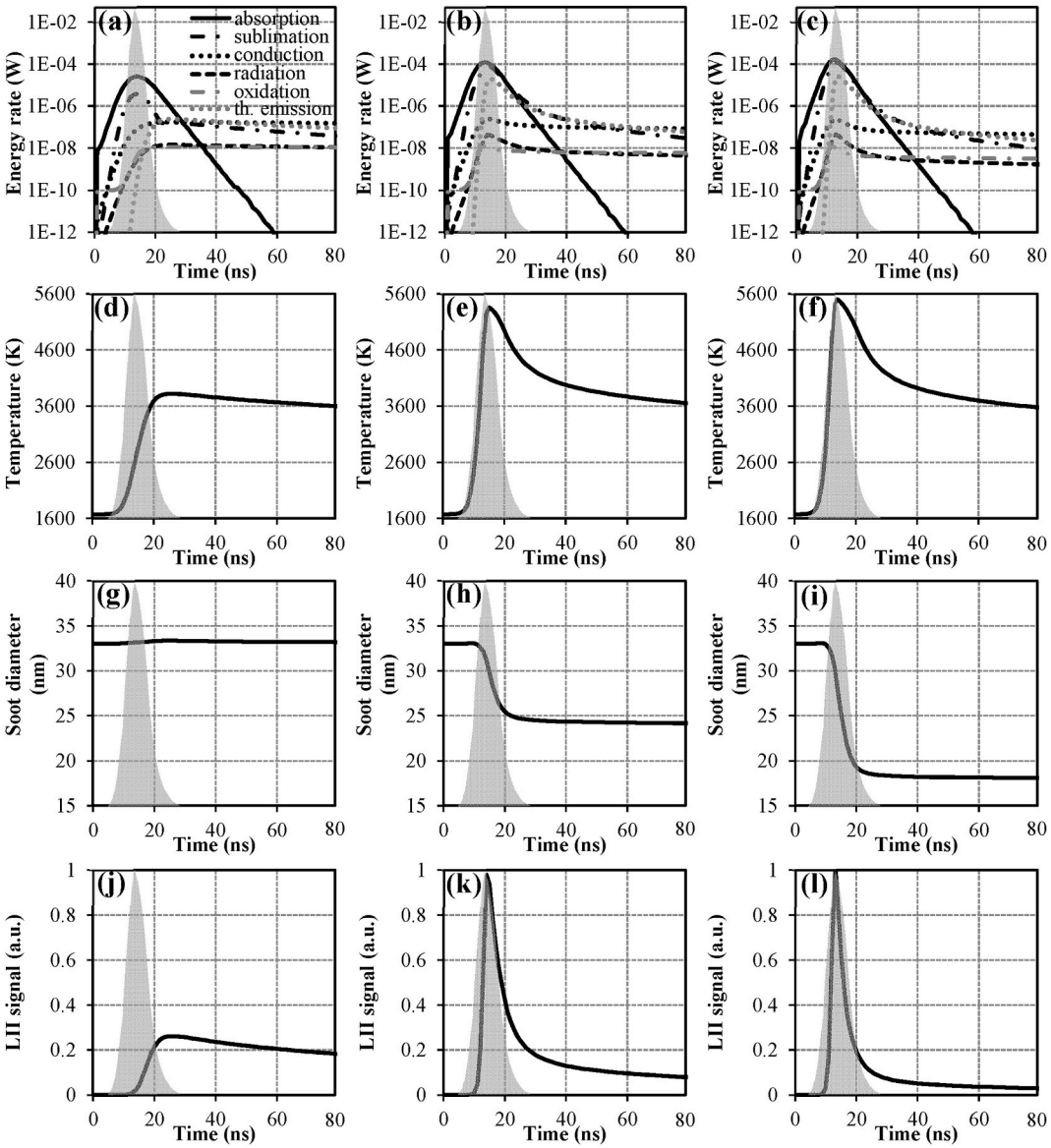

Fig. 18. Temporal evolution of the energy transfer rates ((**a**), (**b**) and (**c**)), soot temperatures ((**d**), (**e**) and (**f**)), soot diameters ((**g**), (**h**) and (**i**)) and LII time decays ((**j**), (**k**) and (**l**)) computed using model 4 to simulate the data collected by Goulay et al. (2013) at 50 mm HAB in the C_2H_4 diffusion flame, using an EW of 532 nm. Note that calculations were performed using the optimized parameters listed in Table 5, considering fluences of 0.05 J cm^{-2} ((**a**), (**d**), (**g**) and (**j**)), 0.20 J cm^{-2} ((**b**), (**e**), (**h**) and (**k**)) and 0.30 J cm^{-2} ((**c**), (**f**), (**i**) and (**l**)). Note also that the gray areas in each figure denote the temporal profiles of the laser pulses used by Goulay et al. (2013).

Fig. 18j, **k** and **l**. This notably explains why a continuous increase of the LII response above the sublimation threshold can be observed in Fig. 17, hence inducing somewhat significant deviations between the experimental and simulation results, depending on the considered dataset. Regarding the gray full line plotted in Fig. 17a–d, it shows that the parameters initially proposed in Michelsen et al. (2007) for an EW of 532 nm do not allow reproducing the fluence curve measured by Goulay et al. (2013). Besides, and in line with the observations reported in Menanteau & Lemaire (2021) and Lemaire & Menanteau (2023b), $B_{\lambda n}$ and $\Delta H_{\lambda s}$ (see Fig. 17c, **d**, **g** and **h**) mainly impact the peak LII response near and above the sublimation threshold (i.e., above ~0.10 (at 532 nm) and ~0.30 (at 1064 nm) J·cm^{-2} in the ethylene and methane flames, respectively) contrary to $E(m)$ and $\sigma_{\lambda n}$, which influence both the increasing and plateau regions of the fluence curves (see Fig. 17a, **b**, **e** and **f**). That LII signals do not exhibit the same sensitivity towards changes in the values of these parameters was already reported by Lemaire & Menanteau (2021, 2023a) and identified as an interesting feature in order to identify local optimum values when parameterizing refined LII models using the optimization procedure detailed in Lemaire & Menanteau (2021), to which the reader is referred for more details. Regarding the influence of the soot absorption function on the modeled fluence curves, Fig. 17a and e show that the higher the $E(m)$, the lower the fluence above which the peak LII signals tend to

plateau (or at least no longer increases significantly), which is in line with expectations. It is, moreover, noteworthy that, although being slightly greater than the $E(m)$ reported in Table 4, the soot absorption functions inferred using model 4 (see Table 5) are still comprised within the more likely range of values defined by Liu et al. (2020). As for Fig. 17b and f, they show that the effect of $\sigma_{\lambda n}$ on computed fluence curves is globally similar to that of $\sigma_{\lambda i}$ in model 3, as is the case for $\Delta H_{\lambda s}$, which behaves similarly to $\Delta H_{\lambda i}$ (see Fig. 17d and h). No further comments will therefore be proffered regarding the effect associated with these parameters. Finally, the plots of Fig. 17c and g evidence that the greater the saturation coefficient for multi-photon absorption, the lower the peak LII signals above the sublimation threshold. According to an analysis of the temporal evolution of the energy transfer rates computed for fluences between 0.2 and 0.4 J cm^{-2}, increasing $B_{\lambda n}$ translates into more absorption, hence leading to more sublimation and a lower D_p, thus explaining why reduced peak LII signals are computed at such high fluences. Overall, and in line with the observations by Lemaire & Mobtil (2015), integrating photolytic mechanisms such as multi-photon absorption and photodesorption of carbon clusters in the formulations of $\dot{Q}_{abs}$ and $\dot{Q}_{sub}$ allows reproducing the relative lack of fluence dependence of the peak LII signals at high fluences. Nevertheless, and as exemplified in Fig. 19, model 4, which was shown to overpredict measured LII signals on the plateau region of the fluence curves, also significantly overpredicts the temperatures measured by Goulay et al. (2013) (as previously noted by Lemaire & Mobtil (2015)) and Bejaoui et al. (2015) at high fluences, thus making it less efficient than model 3 in properly capturing experimental data.

To conclude, and as mentioned in section 4.1.8, a sensitivity analysis focusing on the expression used to account for the thermionic flux was also conducted, and is proposed in Fig. 20. To that end, the variations of the peak LII signals and soot temperatures as a function of the fluence were computed both while neglecting $\dot{Q}_{th}$ and computing it using the equation proposed by Michelsen (2003) (see Eq. (32)) or the one issued from the work by Mitrani et al. (2016) (see Eq. (33)). Furthermore, we additionally analyzed the extent to which the value set for the work function ϕ embedded within $\dot{Q}_{th}$ was likely to influence simulated results. In agreement with the observation made when commenting on Fig. 18, $\dot{Q}_{th}$ does not truly influence the intensity of peak LII signals, except at very high fluences, where very slight deviations can be observed, whether considering or neglecting this flux and whether selecting Eq. (32) or Eq. (33). On the other hand, the effect of $\dot{Q}_{th}$ on the peak temperature profiles is more pronounced, especially for fluences near and above ~0.1 J cm^{-2}, depending on the considered EW. More specifically, neglecting the cooling by thermionic emission (see the light gray dot-dash lines) or using the expression proposed by Mitrani et al. (2016) (see the dark gray dashed lines) leads to predicted T_p values higher than those computed using the sub-model formulation initially proposed by Michelsen (2003) (see the full back lines). Since the updated formulation of the thermionic flux from Mitrani et al. (2016) is believed to be more adapted as it allows to correct the values of emitted current due to the positive charge buildup in laser-heated nanoparticles that increase the energy barrier for further emission of electrons, it is thus noteworthy that its use leads to an increase in the deviation between measured and simulated temperatures, hence suggesting an improper formulation of model 4 and/or of the expressions used to account for the different fluxes embedded within this model. This observation is further strengthened by the fact that improving the agreement between measured and simulated temperature profiles while still reproducing the LII fluence curves in the case of the C_2H_4 diffusion flame would require reducing the value of ϕ to ~5.5×10^{-19} J (see the dark gray dot-dash lines), which would in turn reduce the barrier to further electron emission, contrary to the conclusions by Mitrani et al. (2016). Trying to improve the predictive capability of model 4 by considering the work function as a free-floating parameter is thus not physically consistent.

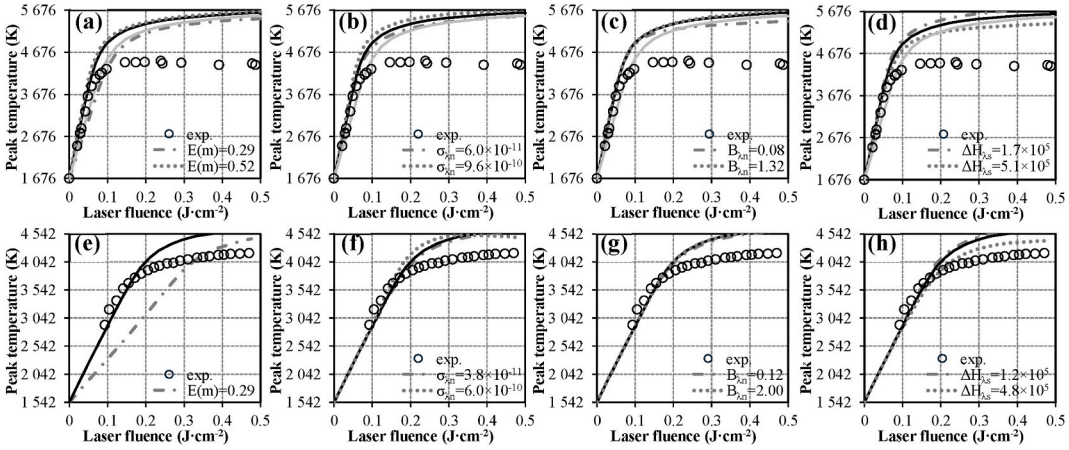

Fig. 19. Comparison of the fluence dependence of the peak soot temperature calculated using model 4 (lines) with experimental results (depicted via circles) measured at 50 mm HAB in the C_2H_4 diffusion flame using an EW of 532 nm ((**a**), (**b**), (**c**) and (**d**)), as well as with the data collected with an EW of 1064 nm at 15 mm HAB ((**e**), (**f**), (**g**) and (**h**)) in the $CH_4/O_2/N_2$ premixed flat flame. Calculations were performed using the optimized parameters listed in Table 5 with $B_{\lambda 1}$ values of 0.58 and 1.15 for EWs of 532 and 1064 nm (Lemaire & Menanteau, 2023a), while computing the thermionic emission flux using Eq. (32) (corresponding results being plotted with a full black line). The light gray full lines in (**a**), (**b**), (**c**) and (**d**) represent the simulated results obtained when parameterizing model 4 exactly as proposed in Michelsen et al. (2007). The other curves correspond to simulated results obtained while varying the $E(m)$, $B_{\lambda n}$, $\sigma_{\lambda n}$ and $\Delta H_{\lambda n}$ values as detailed in the legend of each subfigure.

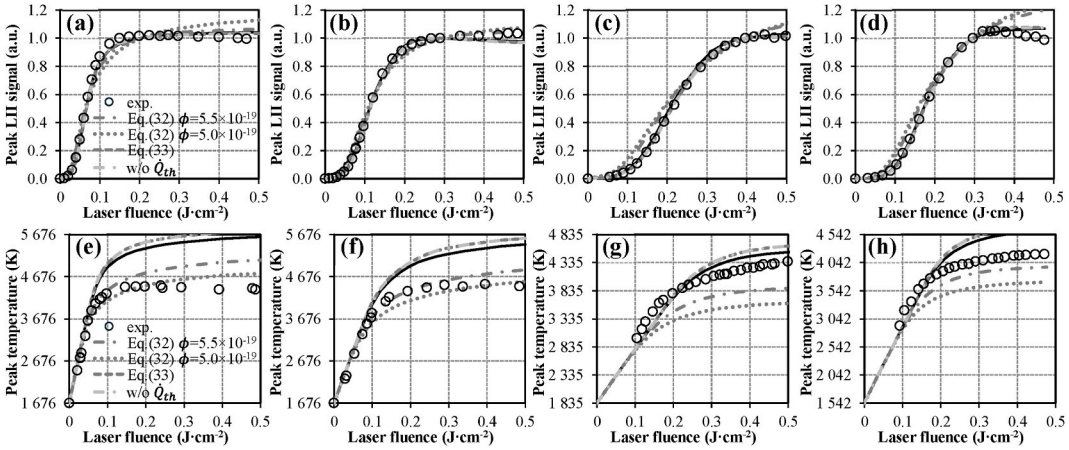

Fig. 20. Comparison of LII fluence curves ((**a**), (**b**), (**c**) and (**d**)) and peak soot temperature profiles ((**e**), (**f**), (**g**) and (**h**)) simulated using model 4 (lines) with experimental results (depicted via circles) measured at 50 mm HAB in the C_2H_4 diffusion flame using EWs of 532 ((**a**) and (**e**)) and 1064 nm ((**b**) and (**f**)), as well as with the data collected with an EW of 1064 nm at 9 ((**c**) and (**g**)) and 15 mm HAB ((**d**) and (**h**)) in the $CH_4/O_2/N_2$ premixed flat flame. Calculations were performed using the optimized parameters listed in Table 5, while computing the thermionic emission flux using Eq. (32) with $\phi = 7.37 \times 10^{-19}$ J (corresponding results being plotted with a full black line). The other curves correspond to simulated results obtained whether considering or neglecting $\dot{Q}_{th}$, using different formulations for this term as well as different work function values as detailed in the legend of each subfigure. Note that the legend in (**a**) and (**e**) also applies to (**b**), (**c**) and (**d**) and (**f**), (**g**) and (**h**), respectively.

5.2.2. *Comparison of measured LII time decays with modeled ones and sensitivity analysis dealing with the formulation and/or parameterization of the sublimation, oxidation and thermionic fluxes*

Fig. 21 compares the LII time decays measured by Goulay et al. (2013) at 50 mm HAB in the C_2H_4 flame using EWs of 532 and 1064 nm, with simulated signals issued from the implementation of model 3. Plotted curves were obtained using the parameters detailed in Table 4 while varying the α_T value as depicted in the chart legends. Furthermore, calculations were also carried out while changing the $\Delta H_{\lambda i}$ value, neglecting $\dot{Q}_{ox}$ or using the alternative expression proposed by Michelsen et al. (2008) as per Eq. (31). The results obtained first show that computed signal intensities are systematically lower than their experimental counterparts after the laser pulse duration. This thus indicates that the soot cooling is overpredicted by the model, regardless of the value selected for the thermal accommodation coefficient. That said, a relatively good agreement can still be noted for fluences of 0.124 and 0.268 J cm^{-2} with EWs of 532 and 1064 nm, respectively, provided α_T is set to a relatively low value of 0.23. Of note, such an agreement, which was not observed in the case of standard models (see section 5.1.2), can be traced to the formulation of the sublimation flux embedded within model 3 as well as to the

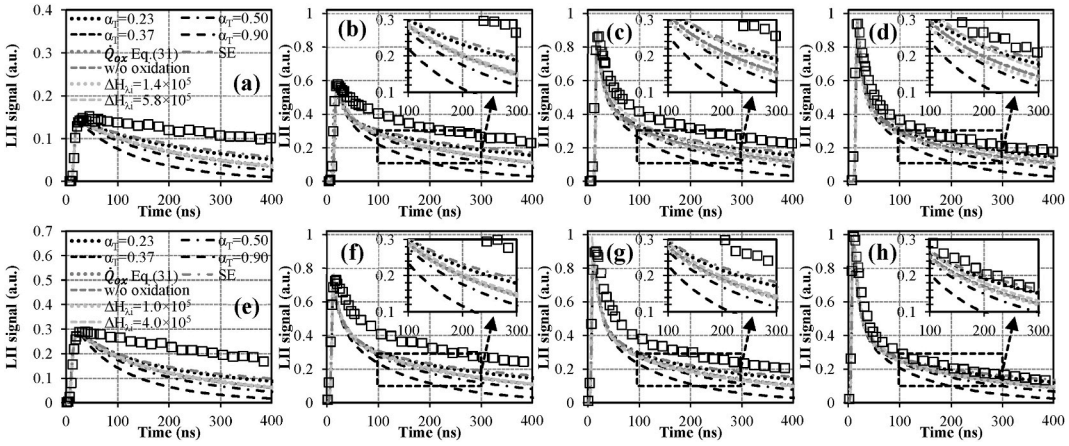

Fig. 21. Comparison of LII time decays simulated using model 3 (lines) with their experimental counterparts (depicted via squares) measured at 50 mm HAB in the C_2H_4 diffusion flame using EWs of 532 nm ((**a**), (**b**), (**c**) and (**d**)) and 1064 nm ((**e**), (**f**), (**g**) and (**h**)) with fluences of 0.040 J cm^{-2} (**a**), 0.069 J cm^{-2} (**b**), 0.100 J cm^{-2} (**c**), 0.124 J cm^{-2} (**d**), 0.088 J cm^{-2} (**e**), 0.146 J cm^{-2} (**f**), 0.194 J cm^{-2} (**g**) and 0.268 J cm^{-2} (**h**). Calculations were performed using the optimized parameters listed in Table 4 and a α_T of 0.37, while computing the oxidation term using Eq. (29). The other curves correspond to simulated results obtained while modifying the model parameterization as detailed in the legend of (**a**) and (**b**), which also applies to (**b**), (**c**) and (**d**) and (**f**), (**g**) and (**h**), respectively. Note that the gray dot-dash lines referred to as "SE" depict the results obtained when considering the shielding effect, with α_T set to 0.23.

inclusion of the annealing flux. As far as $\dot{Q}_{ox}$ is concerned, neglecting its contribution or implementing the alternative expression proposed by Michelsen et al. (2008) does not truly influence the obtained results, which points to the rather negligible impact this term has on the energy and mass balances, as further discussed in section 5.3.1. Finally, dividing or multiplying the $\Delta H_{\lambda i}$ value from Table 4 by a factor of 2 is shown to influence the time decays only at high fluences (see Fig. 21c, **d**, **g** and **h**), which is consistent with the specific role played by this parameter on $\dot{Q}_{sub}$ as per Eq. (19). Reducing the value of the energy required to remove C_2 clusters by nonthermal photodesorption actually translates into more sublimation, thus leading to faster time decays, as depicted in Fig. 21. As for the results in Fig. 22, they show that the above observations regarding the impact of $\dot{Q}_{ox}$ and $\Delta H_{\lambda i}$ on LII time decays also apply to the modeling of the signals collected in the $CH_4/O_2/N_2$ premixed flat flame. The obtained plots, moreover, show that model 3 better reproduces the signals measured by Bejaoui et al. (2015). Specifically, computed time decays globally matching their experimental counterparts at 9 mm HAB can be obtained by setting α_T to a very high value of 0.90 at 0.089 J cm^{-2} (see Fig. 22a) versus 0.50 between 0.169 and 0.217 J cm^{-2} (see Fig. 22a and b) and 0.37 at 0.284 J cm^{-2} (see Fig. 22d). Regarding the time decays measured at 15 mm HAB, they can be roughly mimicked by model 3, provided α_T is set to 0.50 at 0.138 J cm^{-2} (see Fig. 22e) and 0.23 for the other fluences (see Fig. 22f to **h**). That reducing α_T as a function of the fluence and HAB (i.e., as a function of T_p and of the soot maturity) is necessary to improve the agreement between simulated and measured LII time decays tends to corroborate the observations by Bladh, Johnsson, & Bengtsson (2009), Bladh et al. (2011a) and López-Yglesias, Schrader, & Michelsen (2014). According to Michelsen et al. (2015), the soot maturity dependence of α_T would be consistent with a series of theoretical and experimental analyses (including those by Rettner et al. (1996), Sha & Jackson (2002), Zecho et al. (2002), Miura et al. (2003) or Güttler, Zecho & Küppers (2004), as examples), indicating a surface roughening and an enhanced gas surface energy transfer at graphite surfaces when hydrogen is bound to the surface. Nevertheless, additional calculations performed using the α_T expression proposed by López-Yglesias, Schrader, & Michelsen (2014), which is supposed to depend on the surface maturity of the particle (see Eq. (40)), still led to obtaining simulated time decays (not reported in Figs. 21 and 22 for clarity) significantly diverging from experimental ones. Additional work aimed at formulating α_T expressions integrating the H/C ratio and/or other properties depicting the fine structure of particle surface would thus be required in an attempt to better account for the potential dependence of the thermal accommodation coefficient on the soot maturation stage. To conclude, and since the plots of Fig. 21 show that none of the tested parameterizations allow to reproduce measured data on the range of fluences considered, we performed a series of complementary calculations using the equivalent heat conduction diameter proposed by Liu et al. (2006a), instead of D_p, to take into account the shielding effect (SE) induced by the presence of several primary particles within aggregates. The obtained curves (referred to as "SE" in the legends of Figs. 21 and 22) show that integrating the D_{HC} formulation from Eq. (42) in model 3 allows computing LII time decays which are slightly closer to measured ones in the ethylene flame, provided α_T is set to the lower bound defined in section 5.1.2 (i.e., 0.23). The agreement is still far from satisfactory, however. As for the results obtained in the methane flame, mimicking measured signals while considering the shielding effect leads to inferring a very high α_T between 0.49 and 0.90 (this latter value corresponding to the upper bound set during the optimization process) at 9 mm HAB versus more common values comprised between 0.23 and 0.44 at 15 mm HAB. Although these results, here again, exemplify how integrating aggregate properties may significantly influence modeled signals, they also show that the formulation of model 3 and/or of the sub-models embedded within its heat and mass balance equations seem inappropriate to properly capture the physics at play during the laser-induced incandescence of the soot produced in the ethylene flame characterized by Goulay et al. (2013).

To conclude, in Fig. 23, we report the results obtained with model 4. Of note, only the signals issued from the analysis of the C_2H_4

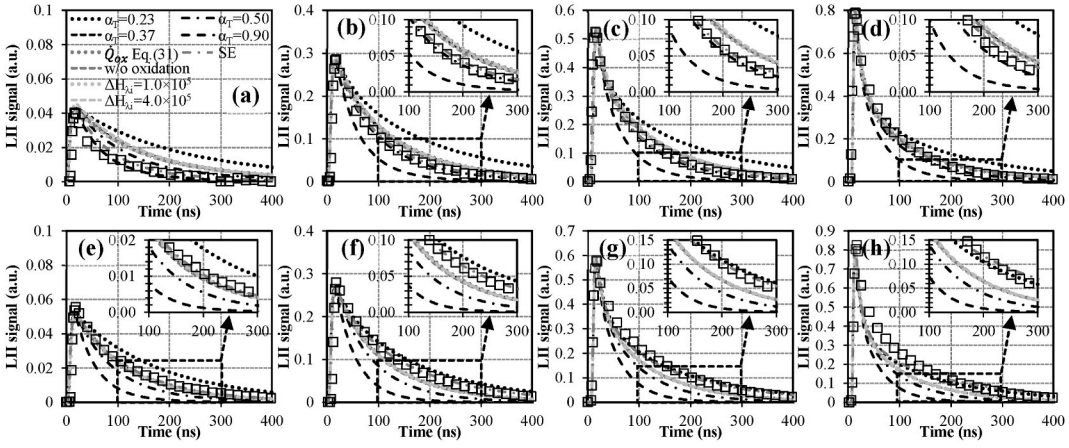

Fig. 22. Comparison of LII time decays simulated using model 3 (lines) with their experimental counterparts (depicted via squares) measured at 9 (**a**), (**b**), (**c**) and (**d**)) and 15 mm HAB ((**e**), (**f**), (**g**) and (**h**)) in the $CH_4/O_2/N_2$ premixed flat flame with fluences of 0.089 J cm^{-2} (**a**), 0.169 J cm^{-2} (**b**), 0.217 J cm^{-2} (**c**), 0.284 J cm^{-2} (**d**), 0.088 J cm^{-2} (**e**), 0.138 J cm^{-2} (**f**), 0.186 J cm^{-2} (**g**) and 0.234 J cm^{-2} (**h**). Calculations were performed using the optimized parameters listed in Table 4 and a α_T of 0.37, while computing the oxidation term using Eq. (29). The other curves correspond to simulated results obtained while modifying the parameterization of the model as detailed in the legend of (**a**), which also applies to the other subfigures. Note that the gray dot-dash lines referred to as "SE" depict the results obtained when considering the shielding effect, with α_T set to 0.90 (**a**), 0.56 (**b**), 0.54 (**c**), 0.49 (**d**), 0.44 (**e**), 0.33 (**f**), 0.30 (**g**) and 0.23 (**h**).

flame using an EW of 532 nm and those obtained at 15 mm HAB in the $CH_4/O_2/N_2$ flame using an EW of 1064 nm are depicted therein, for brevity. The plots of Fig. 23a, **b**, **c** and **d** first show that model 4 fails to reproduce the data measured by Goulay et al. (2013) regardless of the α_T selected. More specifically, the simulated time decays are much faster than their experimental counterparts, which can be traced to the excessively high temperatures computed by this model above $\sim$0.05 J cm^{-2} (see Fig. 20e), hence leading D_p to rapidly decrease due to a too high sublimation rate. A similar observation can, moreover, be made when analyzing the results relating to the methane flame as exemplified in Fig. 23g and h, depicting the LII temporal profiles corresponding to fluences of 0.186 J cm^{-2} and 0.234 J cm^{-2}, for which the predicted peak T_p exceed the measured ones, as illustrated by Fig. 20h. Note that Fig. 23 also reports the results issued from a quick sensitivity analysis focusing on the impact of $\dot{Q}_{th}$ on modeled signals. This flux was notably neglected (corresponding curves being referred to as "w/o $\dot{Q}_{th}$") or computed using Eq. (33) issued from the work of Mitrani et al. (2016) and Eq. (32) taken from Michelsen et al. (2007) with ϕ set to $\sim 5.5 \times 10^{-19}$ J instead of 7.37×10^{-19} J, which is the default value used to derive the other signals. As can be seen by looking at Fig. 23, neglecting $\dot{Q}_{th}$ or using Eq. (33) has no significant impact on simulated LII time decays. On the other hand, reducing the value of the work function implemented in the thermionic sub-model proposed by Michelsen (Eq. (32)) translates into theoretical LII responses whose intensities for short times t overpredict measured ones at relatively low fluences (see Fig. 23a, **b**, **e** and **f**), which is in line with the observations made when commenting on the fluence curves of Fig. 20. Alternatively, reducing ϕ to $\sim 5.5 \times 10^{-19}$ J promotes soot cooling by the thermal ejection of electrons and increases the gap between simulated and measured signals when higher fluences are used (see Fig. 23c, **d**, **g** and **h**.), despite the better agreement between theoretical and experimental temperature profiles previously observed from Fig. 20e and h. All these observations thus confirm the conclusion that reducing ϕ in order to improve the predictive capability of model 4 is not a good option, in addition to being physically inconsistent, as explained in section 5.2.1 by referring to the work by Mitrani et al. (2016). Finally, integrating the equivalent heat conduction diameter from Liu et al. (2006a) to account for the shielding effect does not allow to significantly improve the predictions of model 4. Indeed, and although selecting α_T of 0.43 and 0.30 (versus values of 0.50 and 0.23 when neglecting SE) allows to properly reproduce the signals measured at 15 mm HAB in the methane flame for fluences of 0.088 J cm^{-2} and 0.138 J cm^{-2}, the other middle gray dotted lines in Fig. 23 still show that model 4 tends to largely overpredict the time decays of the LII signals, even while selecting a very low α_T of 0.23 (see Fig. 23a, **b**, **c**, **d**, **g** and **h**).

5.2.3. *Summary of highlighted trends and discussion*

In comparison with standard model formulations, the refined treatment of the soot energy- and mass-balance equations integrated within models 3 and 4 makes them more complex to implement and parameterize. This is especially due to the inclusion of additional mechanisms (e.g., oxidation and annealing in model 3 and multi-photon absorption and cooling by thermionic emission in model 4), whose expressions involve various factors (e.g., saturation coefficient related to the removal of carbon clusters by photodesorption, saturation coefficient for multi-photon absorption, cross-section for the photodesorption of carbon clusters, etc.) needing to be empirically assessed. This intrinsic complexity can be considered as a source of uncertainties due to the large degrees of freedom associated with the inference of unknown parameters and to possible over-tuning issues (Sipkens et al., 2018a). The inclusion of photolytic mechanisms such as those embedded within models 3 and 4 was still shown by Lemaire & Mobtil (2015) to be required if simulated signals matching measured ones on an extended range of fluences are to be derived. This was further exemplified by the results reported in section 5.2.1, which showed that properly mimicking the relative lack of fluence dependence of the LII signals above

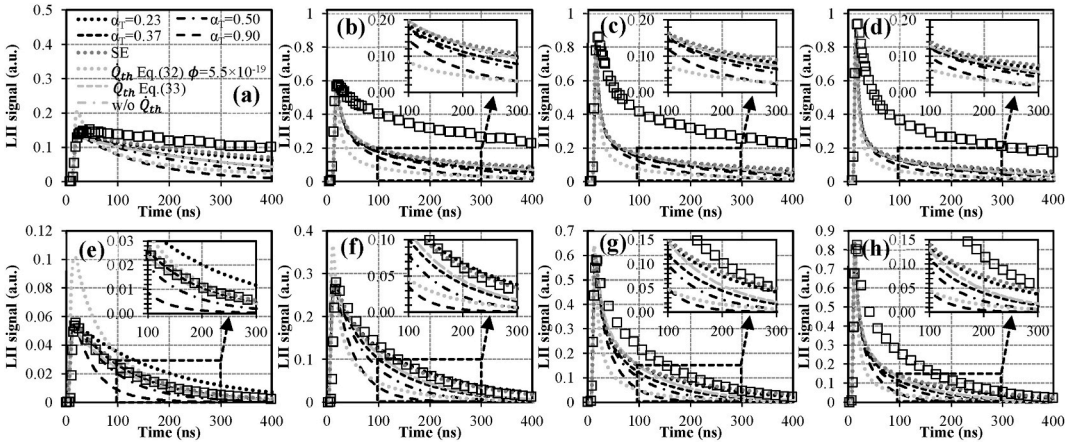

Fig. 23. Comparison of LII time decays simulated using model 4 (lines) with their experimental counterparts (depicted via squares) measured at 50 mm HAB in the C_2H_4 diffusion flame with an EW of 532 nm and fluences of 0.040 J cm^{-2} (**a**), 0.069 J cm^{-2} (**b**), 0.100 J cm^{-2} (**c**), 0.124 J cm^{-2} (**d**) as well as at 15 mm HAB in the $CH_4/O_2/N_2$ premixed flat flame with fluences of 0.088 J cm^{-2} (**e**), 0.138 J cm^{-2} (**f**), 0.186 J cm^{-2} (**g**) and 0.234 J cm^{-2} (**h**). Calculations were performed using the optimized parameters listed in Table 5 and a α_T of 0.37, while computing the thermionic emission flux using Eq. (32). The other curves correspond to simulated results obtained while modifying the parameterization of the model as detailed in the legend of (**a**), which also applies to the other subfigures. Note that the gray dot-dash lines referred to as "SE" depict the results obtained when considering the shielding effect, with α_T set to 0.23 ((**a**) **to** (**d**) and (**g**) and (**h**)), 0.43 (**e**) and 0.30 (**f**).

the sublimation threshold requires implementing expressions for the sublimation flux that account for the nonthermal photodesorption of carbon clusters in both models 3 and 4. In agreement with the observations in Lemaire & Menanteau (2021, 2023a), the sensitivity analyses conducted in sections 5.2.1 and 5.2.2 showed that the empirical factors (whose values need to be set) do not influence the LII response in the same way, all depending on the excitation wavelength, the laser fluence and the time. Parameterizing refined models by implementing an optimization procedure aimed at reducing the mean square deviation between measured and computed signals while considering the whole lifetime of the LII signals for a wide range of fluences can thus allow to identify unique sets of parameters as noted during the parameterization conducted in the present work, and as illustrated by the existence of local optimums in the DoE response surfaces reported in Menanteau & Lemaire (2020, 2022) and (Lemaire & Menanteau, 2021, 2023a). The values of the inferred parameters are, however, subject to more or large uncertainties, as discussed in Lemaire & Menanteau (2021, 2023a) where the influence of measurement noise and errors in the estimation of the flame temperature and soot initial diameter, among others, were analyzed. Notwithstanding their ability to reproduce the so-called plateau region of the fluence curves (contrary to models 1 and 2, which failed to do so), models 3 and 4 are still unable to predict LII time decays matching those measured in the C_2H_4 and $CH_4/O_2/N_2$ flames over an extended range of fluences up to 0.5 J cm^{-2}. The results obtained, moreover, showed that model 3 globally performs better than model 4, which tends to predict soot temperatures by far exceeding those of its experimental counterparts. Among the sources of uncertainties associated with the expressions used to account for the energy fluxes embedded within models 3 and 4 that could explain the discrepancies noted between measured and simulated data, one can cite the formulation of $\dot{Q}_{ann}$, whose governing equation, as proposed by Michelsen (2003), leads to predicting an onset of annealing at temperatures as low as that of the flame, whereas the experiments by Cenker & Roberts (2017) showed that annealing starts above ~4000 K (see section 5.2.1). These observations notably led Sipkens et al. (2019) to propose an alternative empirical sub-model inspired by the reducing sphere model proposed by Butenko et al. (2000) for the annealing of diamond in carbon nanoparticles. This formulation, whose integration in model 3 is explored below for completeness, follows an equation of type:

$$\frac{dX_a}{dt} = 6 \cdot A_0 \cdot \frac{(1 - X_a)^{2/3}}{D_p} \cdot exp\left(\frac{-E_A}{R \cdot T_p}\right) \tag{43}$$

where A_0 and E_A are respectively the pre-exponential factor and the activation energy of the Arrhenius-based relation allowing to account for the progression of the soot annealed fraction (see Sipkens et al. (2019) for more details). By substituting Eq. (28) in model 3 by Eq. (43) while using the MATLAB® 'ode45' solver to compute X_a, one obtains the light gray curves in Fig. 24, which are compared with the results from the implementation of the annealing sub-model from Michelsen (2003) (see black lines). The obtained curves are also compared therein with the data obtained from calculations performed considering an updated version of the model developed by Sipkens et al. (2019), recently introduced by Liu (2024) during the 10th International Workshop on Laser-Induced Incandescence (see gray lines). This alternative formulation integrates the contributions of both thermal-induced and photon-induced annealing such that the variation of X_a as a function of time expresses as per Eq. (44):

$$\frac{dX_a}{dt} = 3 \cdot \frac{(1 - X_a)^{\frac{2}{3}}}{D_p} \cdot \left[2 \cdot A_0 \cdot exp\left(\frac{-E_A}{R \cdot T_p}\right) + 8 \times 10^{-19} \cdot \frac{E(m) \cdot F \cdot q_{exp}(t)}{\lambda}\right] \tag{44}$$

Note that although the calculations presented in Liu (2024) were carried out considering alternative A_0 and E_A values, we still used the parameters initially proposed in Sipkens et al. (2019) to represent the thermal-induced annealing in order to better highlight the impact of the right-hand term of Eq. (44). Besides, and as was done in Sipkens et al. (2019), X_a was set to 0 as an initial condition to compute dX_a/dt using Eqs. (43) and (44). Although being subject to large uncertainties, such an initial value was nonetheless selected to implement the above-described sub-models as proposed by their respective authors. In line with the observations by Sipkens et al. (2019), the plots in Fig. 24c show that the annealed fractions computed at relatively low fluences using Eq. (43) are significantly lower than those resulting from the implementation of Eq. (28) (see the black curves in Fig. 24c), while the contrary is observed at higher

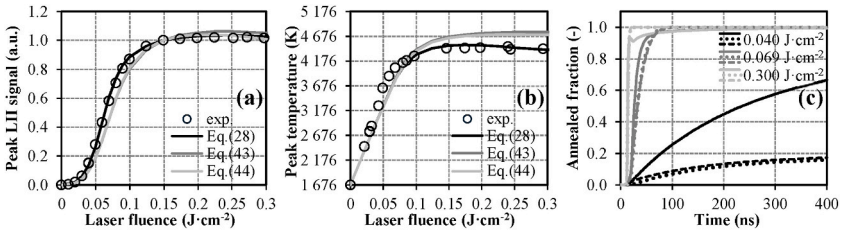

Fig. 24. Comparison of the fluence dependence of the peak LII signals (**a**) and soot temperatures (**b**) computed using model 3 integrating the annealing sub-models proposed by Michelsen (2003) (Eq. (28)), Sipkens et al. (2019) (Eq. (43)) and Liu (2024) (Eq. (44)) (lines) with experimental results (depicted by means of circles) measured at 50 mm HAB in the C_2H_4 diffusion flame using an EW of 532 nm as an example. Calculations were performed using the optimized parameters listed in Table 4, while computing the oxidation term using Eq. (29). As for (**c**), it depicts the simulated changes in the annealed fraction, X_a, as a function of time for fluences of 0.040, 0.069 and 0.300 J cm^{-2}. Note that the full, dotted and dashed lines correspond to the results obtained when implementing the annealing sub-models proposed by Michelsen (2003), Sipkens et al. (2019) and Liu (2024), respectively.

fluences (see the light and dark gray curves in Fig. 24c). As for the modeling approach proposed by Liu (2024), it tends to predict X_a values very close to those obtained when considering the sub-model from Sipkens et al. (2019) (see Fig. 24c), thus indicating that the photon-induced contribution in Eq. (44) is marginal in the conditions investigated herein. Nevertheless, the formulation proposed by Liu (2024), which is part of a work in progress, and is therefore intended to be refined, still has the merit of considering the potential impact of non-thermal annealing on modifications of the soot structure when high laser fluences are used. This hence justifies the interest in pursuing these preliminary developments, as was recently done by Liu, Sipkens & Corbin (2025) who proposed an alternative parameterization of Eq. (44). The implementation of this updated annealing sub-model, however, led to simulated results that significantly diverged from measured ones (especially for fluences above 0.15 J cm^{-2}), regardless of the considered soot absorption function values. This explains why corresponding results were not reported in Fig. 24, and further amplifies the need for complementary works to be undertaken. On the other hand, that lower X_a are predicted when using Eqs. (43) and (44) instead of Eq. (28) at low fluences (for which T_p is relatively low) is consistent with the experimental observations by Cenker & Roberts (2017). The results depicted in Fig. 24a and b, however, show that replacing the equation initially proposed by Michelsen (2003) to compute X_a with those developed by Sipkens et al. (2019) and Liu (2024) does not allow improving the agreement between measured and simulated data. Similarly, the results in sections 5.2.1 and **5.2.2** led to conclude that integrating the thermionic emission sub-model proposed by Mitrani et al. (2016) instead of that proposed by Michelsen (2003) does not result in an improvement of the predictive capability of

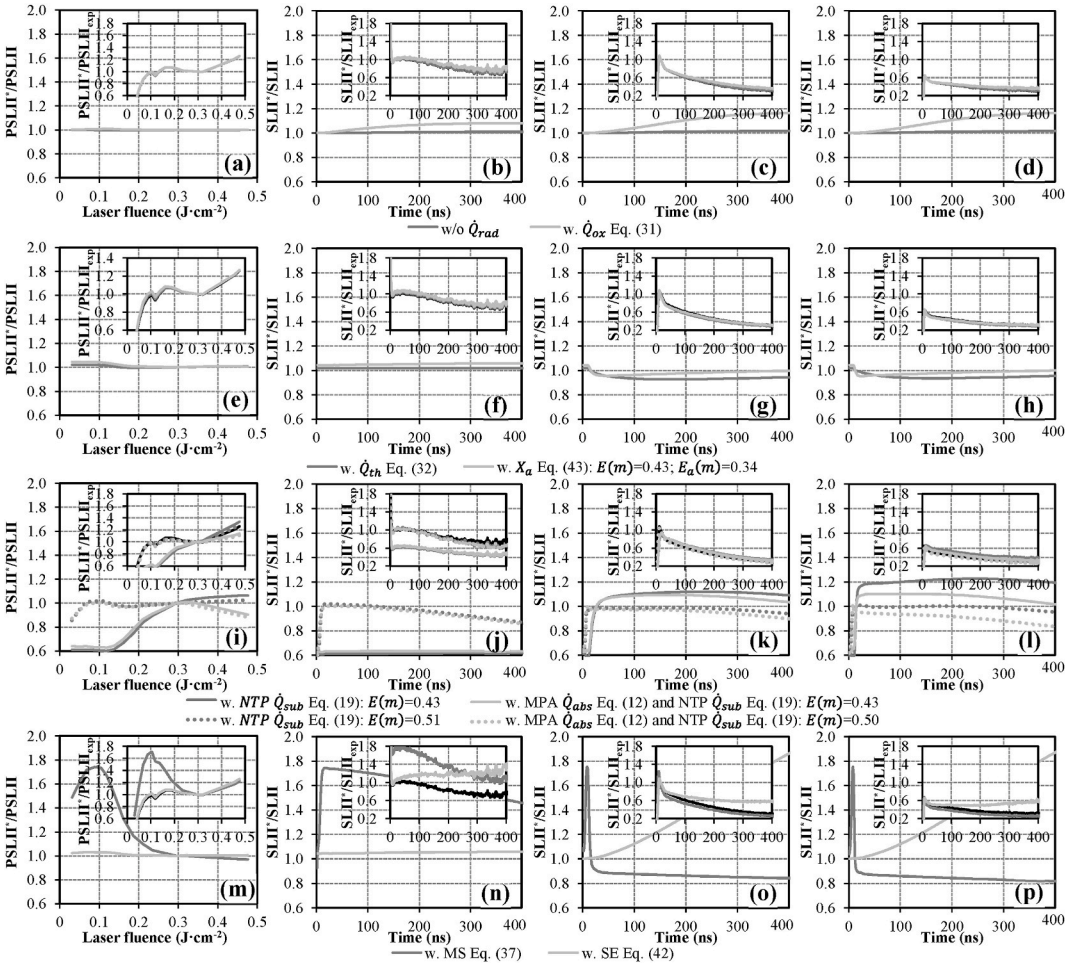

Fig. 25. Evolution of the ratios between peak and time-dependent LII responses computed using model 1 (denoted PSLII and SLII) and LII signals (denoted PSLII* and SLII*) derived when neglecting (w/o) or adding (w.) $\dot{Q}_{rad}$, $\dot{Q}_{ox}$, $\dot{Q}_{th}$, soot annealing, NTP, MPA, SE and MS as a function of the fluence (**a**, **e**, **i**, **m**) and time at 0.088 J cm^{-2} (**b**, **f**, **j**, **n**), 0.186 J cm^{-2} (**c**, **g**, **k**, **o**) and 0.234 J cm^{-2} (**d**, **h**, **l**, **p**). The inset in each subfigure represents the ratio between simulated and measured signals (denoted 'SLII$_{exp}$'), noting that the results obtained herein are issued from calculations aimed at simulating the data collected at 15 mm HAB in the $CH_4/O_2/N_2$ premixed flat flame from Bejaoui et al. (2015). Note also that model 1 was parameterized as detailed in section 4 setting the $E(m)$ and α_T to 0.43 and 0.37, respectively (see section 5.1), while the sub-models used to represent $\dot{Q}_{ox}$, $\dot{Q}_{th}$, X_a, NTP, MPA, SE and MS were implemented using the equations detailed in the chart legends. As for the dotted lines reported in **m** to **p**, they represent results obtained after optimizing the soot absorption function to reduce the mean square deviation between measurement and simulation. To conclude, the full black lines in the insets represent the PSLII/PSLII$_{exp}$ and SLII/SLII$_{exp}$ ratios used as reference plots to help figure out whether or not the exclusion or the inclusion of the above-listed terms allows to improve the agreement between measurement and simulation.

model 4, although the expression of $\dot{Q}_{th}$ from Mitrani et al. (2016) is believed to be more consistent as it allows to account for the effects of the positive charge buildup in laser-heated nanoparticles increasing the energy barrier for further emission of electrons. Finally, and as exemplified by the results depicted in section 5.2.2, the influence of $\dot{Q}_{ox}$ on simulated signals is rather negligible regardless of the equation used to account for this flux. Complementary works are obviously more than ever required to refine the formulation of models 3 and 4 as no parameterization and/or sub-model expression allowed them to properly capture the LII time decays measured by Goulay et al. (2013) and Bejaoui et al. (2015). To help identify the energy fluxes that need to be considered and/or further described in greater detail, section 5.3.1 proposes a sensitivity analysis of the relative impact of radiation, oxidation, thermionic emission, annealing, nonthermal photodesorption, multi-photon absorption, SE and MS.

5.3. *Complementary analyses and perspectives on the development of LII modeling tools*

5.3.1. *Sensitivity analyses focusing on the relative importance of various terms embedded within current LII models*

To assess the sensitivity of LII model predictions to the removal and/or integration of some sub-models and corrective factors, in Fig. 25, we plotted the variations of the ratio between the signals obtained using a standard Melton-based model (i.e., model 1) and those computed when neglecting or adding some specific terms as a function of the fluence and time. Of note, the results presented therein are issued from calculations aimed at simulating the data collected at 15 mm HAB in the methane flame studied by Bejaoui et al. (2015). The results obtained when attempting to reproduce the results from the other datasets are not reported for brevity, noting that similar trends were obtained. Besides, and as mentioned at the end of section 5.2.3, the focus of the present sensitivity analysis is especially on $\dot{Q}_{rad}$, $\dot{Q}_{ox}$, $\dot{Q}_{th}$, soot annealing, as well as nonthermal photodesorption (referred to as 'NTP' in the following, for simplicity) and multi-photon absorption (noted 'MPA' below), which influence $\dot{Q}_{abs}$ and $\dot{Q}_{sub}$, in addition to SE and MS, which act on $\dot{Q}_{cond}$ and $\dot{Q}_{abs}$, respectively. As for the first column of Fig. 25 (i.e., Fig. 25a, **e**, **i**, **m**), it represents the fluence dependence of the ratio of the peak LII signals, denoted PSLII*/PSLII, with 'P' referring to 'peak', 'SLII' representing the signals obtained using model 1, and 'SLII*' standing for the LII responses computed when neglecting or integrating the above-listed processes or corrective factors. As for the other subfigures, they depict the variation of the SLII*/SLII ratios as a function of time for fluences of 0.088 J cm^{-2} (Fig. 25b, **f**, **j**, **n**), 0.186 J cm^{-2} (Fig. 25c, **g**, **k**, **o**) and 0.234 J cm^{-2} (Fig. 25d, **h**, **l**, **p**), as examples. Regarding the insets, they report the fluence and time dependencies of the PSLII*/PSLII$_{exp}$ (first column in Fig. 25) and SLII*/SLII$_{exp}$ ratios (second, third and fourth columns in Fig. 25), where SLII$_{exp}$ denotes measured signals. These complementary curves were notably plotted to allow to highlight whether or not the exclusion or the inclusion of the terms listed in the chart legends leads to an improvement of the agreement between experimental and simulated data (noting that the farther the ratio values are from 1, the higher the discrepancy between simulated and measured data). To conclude, we also reported in the insets of Fig. 25 the ratio between the LII responses simulated using model 1 and the measured signals (i.e., PSLII/PSLII$_{exp}$ and SLII/SLII$_{exp}$). These specific curves, which are depicted by means of black full lines, were plotted to help identify the energy fluxes and corrective factors whose addition and/or exclusion allows to improve the predictive capability of the implemented model (computed PSLII*/PSLII$_{exp}$ and SLII*/SLII$_{exp}$ ratios which are closer to 1 than those represented by the black curves indeed indicating that the removed and/or added terms improve the agreement between experimental and computed signals).

In line with expectations, the plots of Fig. 25a and e confirm that $\dot{Q}_{rad}$, $\dot{Q}_{ox}$, $\dot{Q}_{th}$, which only become significant after the laser pulse duration, do not influence the fluence dependence of the peak LII signals. Obtained results still show that as opposed to radiation (see Fig. 25b–d), whose effect on simulated LII signals is marginal regardless of the considered fluence (a point previously discussed in section 5.1.2), soot oxidation, as well as thermionic emission, are likely to slightly influence the LII time decays, as exemplified by the plots of Fig. 25b–d and f to h, respectively. As depicted in the insets of these figures, the inclusion of $\dot{Q}_{ox}$ and $\dot{Q}_{th}$, however, has a negligible impact on the relative agreement between simulated and measured data (the curves depicting the evolution of SLII*/SLII$_{exp}$ being indeed almost superimposed with the black curves representing the variation of SLII/SLII$_{exp}$). As for the effects of soot annealing, the integration of the equation proposed by Sipkens et al. (2019) to compute the variation of X_a as a function of time is shown to slightly influence the LII responses, especially for fluences of 0.186 J cm^{-2} and 0.234 J cm^{-2}. Furthermore, the curves in Fig. 25f–h also illustrate that annealing mainly influences the LII process during the first ns following the beginning of the laser pulse, which could have been expected since this time frame corresponds to the soot heating stage, which is predominantly controlled by the absorptive-heating flux. That being said, and as exemplified by the insets of Fig. 25e–h, adding the expression proposed by Sipkens et al. (2019) to account for soot annealing in the formulation of model 1 does not enhance its predictive capability, which suggests that further developments are required, as noted by Liu (2024), to better capture this specific mechanism likely to modify the soot structure, and hence, its optical properties. Besides, and as can be seen by looking at Fig. 25i–l, both the nonthermal and multi-photon absorption processes significantly influence the LII fluence curves and time decays. While decreasing the peak LII intensities at low fluences as compared to the results obtained when using model 1, the inclusion of these mechanisms conversely increases the peak LII responses for fluences above 0.3 J cm^{-2} (see Fig. 25i). The curves reported in Fig. 25k and l, moreover, show that slower soot heating and cooling are predicted when integrating Eq. (12) and/or (19) in model 1, which is notably related to the fact that higher soot absorption functions need to be considered when the effect of NTP and MPA is taken into account, as detailed in section 5.2.1. This is especially exemplified by the dotted lines in Fig. 25i–l, which illustrate that optimizing the $E(m)$ values to better reproduce experimental results leads to computing PSLII*/PSLII. and SLII*/SLII. ratios close to 1, but however, with no significant improvement of the agreement between measured and simulated data, (see the insets of Fig. 25j–l). Finally, the plots in Fig. 25m–p allow to illustrate the major influences of MS and SE on the fluence and time dependencies of the LII responses, respectively. Considering the shielding effect is, moreover, shown to improve the predictive capability of model 1 (see the light gray curves in the insets of Fig. 25n–p). On the other hand, and as discussed in section 5.1.1 as well as in Yon et al. (2014, 2015) and Lemaire & Menanteau (2021, 2023a), integrating the

generalized structure factor function from Eq. (37) to represent MS requires decreasing the soot absorption functions to account for the effect of aggregation on the absorption capability of soot. Consequently, while the agreement between measured and simulated data is shown to be worsened when integrating the MS sub-model (see the insets of Fig. 25n–p), selecting an $E(m)$ of 0.36 instead of 0.43 alternatively leads to computing identical PSLII*/PSLII$_{exp}$ and PSLII/PSLII$_{exp}$ ratios (data not reported for brevity).

Although far from comprehensive, this brief sensitivity analysis allowed to corroborate the conclusions drawn in the inverse technique-based study by Lemaire & Mobtil (2015) regarding the significant impact the nonthermal photodesorption and multi-photon absorption mechanisms may have on the modeling of LII signals. The above results, moreover, evidenced the importance of considering MS and SE when information on $E(m)$ and α_T are to be derived through the modeling of experimentally monitored data. Furthermore, and although exhibiting a relatively limited effect on the computed LII responses, the influence of the oxidation, thermionic emissions and annealing processes was still shown to become non-negligible as the laser fluence increases. It is finally noteworthy that none of the energy fluxes and corrective factors investigated herein truly led to improving the predictive capability of model 1 when being individually integrated within its formulation. This notably explains why comprehensive modeling tools coupling a series of sub-models which account for the different processes likely to influence soot LII were recently proposed in the literature, as will be illustrated in section 5.3.2. To conclude, note that more refined statistical analyses, including the implementation of a Bayesian model selection approach (Sipkens et al., 2018a, 2018b) as an example, could be of high interest in order to better rule on the specific energy flux and/or mechanisms that would need to be considered, depending on various factors (e.g., the input parameter uncertainty, measurement noise, goodness-of-fit, etc.). It should nonetheless be borne in mind that while implementing such an approach can be more or less straightforward, with formulating standard LII models, the complexity of more refined formulations such as those proposed by Michelsen in Michelsen (2003) and Michelsen et al. (2007) or by Lemaire & Menanteau (2021, 2023a) would render such an analysis more difficult, thus making complementary developments a must.

5.3.2. *Analysis of the predictive capability of a recently developed comprehensive LII model*

To conclude this benchmarking analysis, it is proposed to assess the predictive ability of a refined LII model (referred to as model 5 hereafter) recently proposed by Lemaire & Menanteau (2023a) against three experimental databases, including those from Goulay et al. (2013) and Bejaoui et al. (2015) previously considered in sections 5.1 and **5.2**, to which the set of LII signals collected by Lemaire et al. in a turbulent spray flame of Diesel is added (Bejaoui, Lemaire, & Therssen, 2015; Lemaire, Bejaoui, & Therssen, 2013; Lemaire & Menanteau, 2021, 2023a). This comprehensive version of the laser-irradiated soot heat and mass balance equations integrates terms representing the saturation of linear, single- and multiphoton absorption processes, cooling by sublimation, conduction, radiation and thermionic emission, as well as mechanisms depicting soot oxidation and annealing, non-thermal photodesorption of carbon clusters and corrective factors accounting for SE and MS. In detail, Eqs. (3), (19), (24), (26), (31) and (33) are used to represent dU_{int}/dt, $\dot{Q}_{sub}$, $\dot{Q}_{rad}$, $\dot{Q}_{ann}$, $\dot{Q}_{ox}$ and $\dot{Q}_{th}$. As for $\dot{Q}_{abs}$, it is expressed as the sum of the contributions of unannealed and annealed soot fractions while considering the saturation of linear, single-photon and multi-photon absorption processes, as well as the effect of multiple scattering within aggregates such that:

$$\dot{Q}_{abs} = N_p \cdot C_{abs,s}^{multi} \cdot \frac{f_{1,s} \cdot B_{\lambda 1,s}}{\int_0^{t_l} q_{exp} dt} \cdot \left\{ 1 - exp\left[- \frac{F \cdot q_{exp}}{B_{\lambda 1,s}} \right] \right\} + N_p \cdot C_{abs,a}^{multi} \cdot \frac{f_{1,a} \cdot B_{\lambda 1,a}}{\int_0^{t_l} q_{exp} dt} \cdot \left\{ 1 - exp\left[- \frac{F \cdot q_{exp}}{B_{\lambda 1,a}} \right] \right\} + N_p \cdot \frac{n \cdot h \cdot c}{\lambda_1} \cdot \left(k_{\lambda n,s} + k_{\lambda n,a} \right) \tag{45}$$

where the subscripts ‘s’ and ‘a’ refer to unannealed and annealed soot fractions. The meaning of the different parameters embedded in Eq. (45) was previously detailed in section 4.1.2, except for the absorption cross-sections of unannealed and annealed soot fractions ($C_{abs,s}^{multi}$ and $C_{abs,a}^{multi}$), which are computed in the present case by integrating the MS corrective factor from Yon et al. (2014) as per Eqs. (46) and (47):

$$C_{abs,s}^{multi} = N_{tot} \cdot (1 - X_a) \cdot \frac{\pi^2 \cdot {D_p}^3}{\lambda_1} \cdot E(m) \cdot h_{\lambda,N_p} \cdot p(N_p) \tag{46}$$

$$C_{abs,a}^{multi} = N_{tot} \cdot X_a \cdot \frac{\pi^2 \cdot {D_p}^3}{\lambda_1} \cdot f_a \cdot E_a(m) \cdot h_{\lambda,N_p} \cdot p(N_p) \tag{47}$$

further noting that the rate constants related to the photodesorption of C_2 clusters from unannealed and annealed soot fractions are expressed as follows:

$$k_{\lambda n,s} = (1 - X_a) \cdot \frac{\lambda_1}{n \cdot h \cdot c} \cdot \frac{\sigma_{\lambda n,s} \cdot \pi \cdot {D_p}^3 \cdot N_{ss}}{6} \cdot \frac{(B_{\lambda n,s})^n}{\int_0^{t_l} (q_{exp})^n dt} \cdot \left\{ 1 - exp\left[- \left(\frac{F \cdot q_{exp}}{B_{\lambda n,s}} \right)^n \right] \right\} \tag{48}$$

and

$$k_{\lambda n,a} = X_a \cdot \frac{\lambda_l}{n \cdot h \cdot c} \cdot \frac{\sigma_{\lambda n,a} \cdot \pi \cdot {D_p}^3 \cdot N_{sa}}{6} \cdot \frac{(B_{\lambda n,a})^n}{\int_0^{t_l} (q_{exp})^n dt} \cdot \left\{ 1 - exp\left[- \left(\frac{F \cdot q_{exp}}{B_{\lambda n,a}} \right)^n \right] \right\} \quad (49)$$

Regarding the energy loss at the surface of soot particles through collisions with surrounding gas molecules, it is calculated considering a Fuchs equivalent sphere modeling approach (Fuchs, 1934, 1959) so that the conduction rates in the free molecular (FM) and continuum (C) regimes follow Eqs. (50) and (51), respectively:

$$\dot{Q}_{cond,FM} = \frac{1}{8} \cdot \pi \cdot N_p \cdot \alpha_T \cdot {D_{HC}}^2 \cdot P_g \cdot \sqrt{\frac{8 \cdot k_B \cdot T_\delta}{\pi \cdot M_g}} \cdot \frac{\gamma^* + 1}{\gamma^* - 1} \cdot \left(\frac{T_p}{T_\delta} - 1 \right) \quad (50)$$

$$\dot{Q}_{cond,C} = 4 \cdot \pi \cdot N_p \cdot \left(\frac{D_{HC}}{2} + \delta \right) \cdot \int_{T_g}^{T_\delta} k_g(T) dT \quad (51)$$

where γ^* denotes the mean value of the heat capacity ratio, δ and T_δ correspond to the distance and temperature related to the limiting sphere separating the free molecular regime from the continuum one, while k_g stands for the heat conduction coefficient of the surrounding gas. Of note, as the data issued from the analysis of the Diesel flame studied by Lemaire et al. was obtained using a near-Gaussian laser beams, the experimentally monitored spatial distribution of the laser irradiance was numerically reproduced and discretized using 17 × 17 elements in this case, as validated through a grid sensitivity analysis. Theoretical signals calculated over all the dimensions of the laser beam were subsequently integrated over a 300 μm height corresponding to the dimension of the slit placed in front of the detector used during experiments (see Lemaire & Menanteau (2021, 2023a) for more details). Note that while Eqs. (6) and (7) were considered in Lemaire & Menanteau (2021, 2023a) in computing ρ_s and c_s, the updated expressions proposed by Michelsen (2021) to account for the dependence of the soot density and heat capacity on its temperature and maturation level (see Eqs. (35) and (36)) were chosen instead (see section 5.1.1). Furthermore, we did not adjust the empirical scaling factors for the linear absorption of annealed and unannealed soot depending on the considered dataset. Rather, we used constant values derived from those proposed in Michelsen (2003) and Michelsen et al. (2007). Since the above-listed changes are likely to modify the values that must be set for some input parameters (e.g., the soot absorption function) in order to properly reproduce measured data when using model 5, the latter was thus fully reparametrized. To that end, we implemented the optimization procedure coupling a design of experiments with a genetic algorithm-based solver previously used in Menanteau & Lemaire (2020, 2022) and Lemaire & Menanteau (2021, 2023a), to which the reader is referred for more details. Nonetheless, and contrary to what was done in these specific works, where

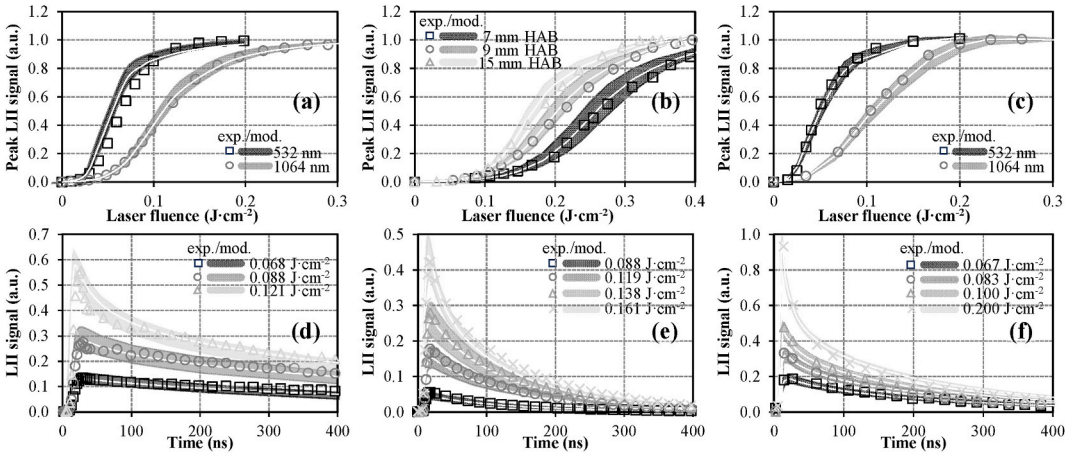

Fig. 26. Comparison of LII fluence curves (**a**, **b**, **c**) and time decays (**d**, **e**, **f**) simulated using model 5 (lines) with experimental data (symbols) measured by Goulay et al. (2013) at 50 mm HAB in the C_2H_4 diffusion flame with EWs of 532 (**a**) and 1064 nm (**a**, **d**), Bejaoui et al. (2015) at 7, 9 (**b**) and 15 (**b**, **e**) mm HAB in the $CH_4/O_2/N_2$ premixed flat flame with an EW of 1064 nm, and Lemaire & Menanteau (2021, 2023a) at 110 mm HAB in the turbulent spray flame of Diesel using EWs of 532 (**c**) and 1064 (**c**, **f**) nm. Simulations were carried out using the following optimized parameters: $\sigma_{\lambda n,s} = 8.1 \times 10^{-10}$ and 4.8×10^{-10} cm^{2n-1} J^{1-n}, $B_{\lambda 1,s} = 0.57$ and 1.08 J cm^{-2}, $B_{\lambda n} = 0.39$ and 0.47 J cm^{-2} and $\Delta H_{\lambda n,s} = 2.33 \times 10^5$ and 1.60×10^5 J mol^{-1} at 532 and 1064 nm, respectively (except at low HAB in the methane flame, where $\sigma_{\lambda n,s}$ for young particles was found to be lower (i.e., 2.0×10^{-10} cm^{2n-1} J^{1-n}), in agreement with the explanations provided in Lemaire & Menanteau (2021)). As for the soot absorption function, the optimization procedure led to infer values of 0.32 in the C_2H_4 flame at 532 and 1064 nm, 0.16, 0.22 and 0.28 at 7, 9 and 15 mm HAB in the $CH_4/O_2/N_2$ flame, respectively, versus 0.42 in the Diesel flame for both considered EWs. Finally, α_T of 0.23, 0.31 and 0.49 were identified as leading to the best fit between measured and simulated LII time decays. Note, to conclude, that the gray domains surrounding the white curves depicting computed LII signals were drawn based on the uncertainty ranges related to each optimized parameter (see Lemaire & Menanteau (2023a) for more details).

only the data collected in the Diesel spray flame were considered for parameterization, we performed a global optimization aimed at reducing the mean square deviation between the signals computed by model 5 and those measured by Goulay et al. (2013), Bejaoui et al. (2015) and Lemaire & Menanteau (2023a) simultaneously. The values of $\sigma_{\lambda n,s}$, $B_{\lambda 1,s}$, $B_{\lambda n,s}$ and $\Delta H_{\lambda n,s}$ detailed in the caption of Fig. 26 were then obtained, noting that the latter are quite close to those previously reported in Lemaire & Menanteau (2023a). Using these parameters, the implementation of model 5 allows to obtain the fluence curves and LII time decays reported in Fig. 26a–c and 26d to f, respectively, which show that the model properly captures the fluence dependence of the peak LII signals experimentally monitored by Goulay et al. (2013), Bejaoui et al. (2015) and Lemaire & Menanteau (2021, 2023a), contrary to models 1 and 2, which failed to do so (see section 5.1). Of note, the $E(m)$ values listed in the caption of Fig. 26 differ slightly from those previously estimated in Lemaire & Menanteau (2021, 2023a), which can be traced to the use of different input parameters and datasets to perform the optimization calculations, as explained above. It is still noteworthy that the $E(m)$ found herein for mature soot (i.e., for high HAB in each studied flames) are in keeping with the more likely range of values recommended by Liu et al. (2020). As for the plots reported in Fig. 26d–f, they show that the LII time decays measured in the different flames with fluences comprised in the low-to-intermediate fluence ranges are correctly simulated, which was not the case when models 1 to 4 were used (see sections 5.1 and 5.2). While confirming the ability of the model formulation proposed by Lemaire & Menanteau (2023a) to reproduce LII signals collected in atmospheric flames burning different types of fuels, model 5 still failed to reproduce the time decays measured by Goulay et al. (2013) for fluences $\geq$0.121 J cm^{-2} (the corresponding signals are thus not depicted in Fig. 26d). Similarly, the plots in Fig. 27, which compares the temperature profiles measured by Goulay et al. (2013) with EWs of 532 and 1064 nm with those simulated by means of model 5, clearly show that, although a good fit can be obtained in the low-to-intermediate fluence regime, predicted temperatures tend to overestimate their experimental counterparts above the sublimation threshold (this behavior being also observed when simulating the results issued from the other datasets). In addition to strengthening the need to refine and/or further parameterize model 5 against data obtained with high laser fluences as concluded in Lemaire & Menanteau (2023a), this observation also supports the need for further data on the C_2H_4 diffusion flame studied by Goulay et al. (2013) to help elucidate whether the discrepancies observed between measured and simulated results are dependent on the specific experiment conducted or on the implemented modeling tool, as was previously pointed out by Mansmann et al. (2018).

To conclude, and to further assess the predictive capability of model 5 against signals collected in widely varying environments, we performed a series of calculations aimed at simulating the LII time decays collected by Mi et al. (2021) in laminar premixed ethylene/air flames stabilized under pressure of 5 and 10 bar and by Zheng et al. (2023) in a jet-A flame stabilized in a pressurized combustor functioning at pressure between 1, 2.4 and 3.8 bar. Here again, and as illustrated by the results reported in Fig. 28, a good agreement between measured and computed data is obtained, which can notably be traced to the use of a Fuchs equivalent sphere modeling approach to compute the conduction flux. It is, moreover, noteworthy that although we did not expend too much effort on trying to optimize the model parameters, the $E(m)$ values we estimated are still included within the more likely range of values recommended by Liu et al. (2020), further noting that the $E(m)$ of 0.46 inferred in the case of the ethylene/air flames is consistent with the value reported by Bladh et al. (2011a). Although encouraging, these results need to be further validated in future works, with larger sets of experimental data used, especially to formulate predictive tools that are valid over an extended range of operating conditions (e.g., low and high pressures, wide varying laser EWs and fluences, etc.).

6. Discussion regarding the limitations of the present work and considerations requiring special attention for future modeling studies

Reiterating first and foremost that this benchmarking analysis does not intend to refine current LII model formulations and/or

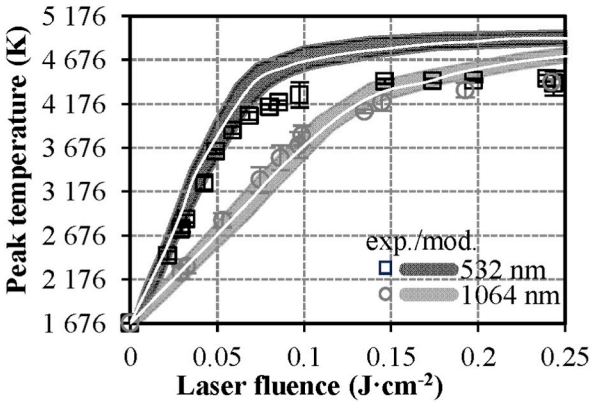

Fig. 27. Comparison of peak soot temperature profiles simulated using model 5 (lines) with experimental results (referred to as "exp.") measured at 50 mm HAB in the C_2H_4 diffusion flame using EWs of 532 (black square) and 1064 nm (gray circles). Note that model 5 was parameterized as detailed in the caption of Fig. 26. Note also that the gray domains surrounding the white curves depicting computed temperatures were drawn based on the uncertainty ranges related to each optimized parameter (see Lemaire & Menanteau (2023a) for more details) while the error bars associated with symbols denote the experimental uncertainties reported in Goulay et al. (2013).

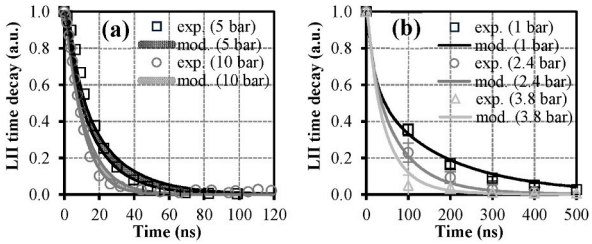

Fig. 28. Comparison of LII time decays simulated using model 5 (lines) and an EW of 1064 nm, with experimental data (symbols and corresponding error bars) measured by (a) Mi et al. (2021) at 15 mm HAB in C_2H_4 premixed laminar flames at pressures of 5 and 10 bar, and (b) Zheng et al. (2023) at 35 mm HAB in a jet-A flame stabilized at pressures of 1, 2.4 and 3.8 bar. Simulations were carried out using the optimized parameters listed in the caption of Fig. 26, except for the thermal accommodation coefficients, which were adjusted to 0.49 as was done to simulate the data collected in the Diesel spray flame from Lemaire & Menanteau (2021, 2023a). As for the soot absorption function, its value was set to 0.46 in (a) and 0.40 in (b), respectively. Finally, the N_p and D_p values reported by Mi et al. (2021) and Zheng et al. (2023) were considered, noting that the gray domains depicted in (a) were drawn based on the uncertainty ranges related to D_p values in (Mi et al., 2021) while the error bars in (b) denote variations in the measured LII intensity.

provide parameter sets which should be imperatively considered for properly simulating LII signals, it is still essential to review the sources of uncertainties and possible statistical issues needing to be considered to correctly rule on the intrinsic validity of the results we obtained while paving the way for future modeling works.

It was previously suggested in sections 5.1.1 and 5.1.2 that measured data could be subject to inaccuracy and/or systematic errors, when commenting on the discrepancies observed between the signals simulated herein and the fluence curves and time decays recorded by Bejaoui et al. (2015) and Goulay et al. (2013), respectively. It should thus be emphasized that different sources of experimental errors, as well as systematic flaws in measurements, in addition to explicit and/or implicit assumptions made during calculations, are likely to more or less significantly affect the validity of the results we obtained. First, and although not being specific to the experimental arrangements which allowed to obtain the measured data used as references herein, it is noteworthy that limitations in detection systems may induce biases in collected signals, as extensively discussed in different reviews, such as those by Schulz et al. (2006) or Michelsen et al. (2015). For instance, when photomultiplier tubes (PMTs) are subjected to continuous high illumination, a photocathode depletion issue can translate into non-linear responses, especially when high-intensity signals (i.e., at the peak of the LII time decays) are recorded. Besides, and although not of major concern herein, since the temperatures considered were derived from the processing of spectrally-resolved LII radiation collected using gated ICCD cameras, the above depletion issue can still influence the intensity calibration of PMTs, leading to systematic deviations in some channels when multi-color systems are used to assess T_p. Furthermore, collection systems comprising PMTs and oscilloscopes may lack the temporal resolution needed to capture the rapid increase of the LII intensity during the soot heating stage. Typical PMTs indeed have rise times of the order of 1–2 ns, and thus cannot properly follow the rapid rise of the LII signals occurring during the laser pulse duration. Consequently, the peak intensity used to plot the fluence curves may be underestimated by an unknown amount. Fitting procedures aimed at tuning model parameters in order to mimic the fluence dependence of the peak LII signals can therefore lead to erroneous results, which must therefore be considered with caution. Due to the possible influence of these sources of errors and to the significant effort required to integrate them out, inferring model parameters by inverse calculations based on measured data is thus quite challenging (Sipkens et al., 2017, 2018a). That being said, this observation does not truly challenge the consistency of the main trends discussed in this paper, since inferring model parameters was clearly out of the scope of the proposed benchmarking analysis. As stated before, the basic optimization calculations conducted in section 5 only aimed at helping to better understand the impact of some soot properties and empirical factors governing the LII responses on computed signals while assessing whether or not the parameter values allowing to obtain relatively good fits between experiments and simulations were comprised within the most likely range of values reported in the literature. It is, moreover, noteworthy that while the spatial distribution of the laser irradiance was numerically discretized when simulating the data collected by Lemaire & Menanteau (2021, 2023a) in section 5.3.2, we did not do so when modeling the results by Goulay et al. (2013) and Bejaoui et al. (2015), who considered spatially homogeneous top hat profiles. It should, however, be pointed out that the laser energy distribution in LII measurements is never truly homogeneous, as can clearly be seen when looking at the spatial beam profiles reported in Goulay et al. (2013) and Bejaoui et al. (2015). The fact that homogenous distributions of the laser energy were considered in modeling the results issued from these two datasets may thus have led to erroneous signal predictions, since non-uniformity of laser profiles has been shown to significantly influence LII measurements carried out using the auto-compensating method for instance (Liu et al., 2016). Furthermore, inhomogeneities have also been identified as being possibly responsible for the so-called “anomalous cooling” (Snelling et al., 2009; Talebi Moghaddam & Daun, 2018), in which the observed pyrometric temperature decreases much faster immediately after a peak value is reached than would be expected based on calculations performed using conventional heat and mass transfer models. Although different studies have exemplified the importance of a proper discretization of the distribution of the laser energy in LII modeling when considering highly non-uniform spatial profiles (see Mobtil & Lemaire (2012), for example), no specific effort was expended herein on spatially discretizing the laser beams used in Goulay et al. (2013) and Bejaoui et al. (2015), as stated in section 4.2, since no evident “anomalous cooling” can be evidenced from the temperature profiles reported by Goulay et al. (2013), for instance. Furthermore, and even though the assumption of a homogeneous spatial distribution of laser energy could potentially alter the value of model parameters, which would be inferred through a fitting procedure (which is outside of the scope of

this work), it may not qualitatively influence the relative importance of the different processes involved in the LII process, and may thus not challenge the validity of the main trends and observations previously drawn. That said, to better rule on this latter point, we still performed additional calculations to briefly compare the results obtained when simulating the data obtained with an EW of 1064 nm at 50 mm HAB in the C_2H_4 diffusion flame and at 15 mm HAB in the $CH_4/O_2/N_2$ premixed flat flame using model 5 while discretizing or not discretizing the spatial domain of the laser beam, considering 14×14 and 19×4 elements, respectively, as examples. The results obtained then showed that the slight inhomogeneities in the spatial distribution of the laser irradiance reported by Goulay et al. (2013) and Bejaoui et al. (2015) have but a relatively limited influence on obtained results (with mean variations in predicted signals less than $\sim$5 %), and should thus not fundamentally alter the validity of the comparison work proposed. This may, however, impact the values of input parameters inferred by inverse calculations based on measured data, thus prompting the need to consider such an aspect when implementing LII models in that end (as we did in Lemaire & Menanteau (2021, 2023a) where the spatial distribution of the laser energy was properly discretized when trying to gain insights into the variation of the soot absorption function as a function of the wavelength and soot maturation stage based on LII modeling of data collected in a Diesel flame). Complementary tests conducted with widely varying laser profiles while conducting mesh sensitivity analyses should, moreover, be a must to better rule on the relative impact of laser inhomogeneities when parameterizing LII models, the above result being indeed issued from preliminary calculations. Note, to conclude, that the statistical treatment of the model parameters derived from the optimization routines we implemented to gain insight into the range of values that can be set for some soot properties also calls for clarifications. We did not dwell on this before, though, as it is not the aim of this review, as mentioned above. That said, caution should be exercised when interpreting the results we obtained even though our attempt of parameterization of model 5 in section 5.3.2 was carried out by considering multiple parameters in the meantime, multiple datasets, the whole lifetime of the LII signals for a wide range of fluences while also integrating uncertainties related to T_g ($\pm$23 K), D_p ($\pm$2.7 nm), and $SLII_{exp}$ ($\pm$5 %) (see Lemaire & Menanteau (2021)). Indeed, and as discussed above, all the experimental data contain errors and uncertainties. Although the latter may not challenge the conclusion drawn regarding the inability of standard model formulations to properly mimic the lack of fluence dependence of LII signals above the sublimation threshold, which is fundamentally related to the physical treatment of the energy fluxes embedded within such simulation tools, it should still be kept in mind that fine-tuning model parameters from noisy or imperfect data is more than challenging. The present work thus does not claim that the results obtained with the somewhat parameterized version of model 5 proposed herein should be given more weight than is warranted, as they merely represent a simple illustration of how a model can potentially simulate data issued from different datasets. As explained at the end of section 5.3.1, attempting to propose a universally valid parameterized LII model would, of course, require a more rigorous statistical approach, as proposed in recent works by Sipkens et al. (2017, 2018a), who pioneered the introduction of the Bayesian framework for LII modeling, thus paving the way for future works.

7. Conclusion

Over the last decades, LII has come to represent a reference diagnostic tool for the in situ measurement of soot volume fractions in combustion environments, and its use continues to expand into new and widely varying application areas (Michelsen et al., 2015). Despite the significant effort which has gone into developing an in-depth understanding of the physical mechanisms and parameters controlling the laser-induced incandescence phenomenon, the validity of predictions stemming from the theoretical models developed to simulate the radiative emission from laser-heated particles are still subject to more or large uncertainties. The wide variability in the results from different LII models actually prompts the need to direct efforts to determine the critical energy and mass balance mechanisms which should be implemented in models while developing adapted model validation protocols. In this context, the present work, which, to the best of the authors' knowledge, represents the most comprehensive benchmarking analysis of commonly used LII modeling approaches, contributes to addressing these issues by assessing the predictive capability of a series of standard and refined LII models against different experimental databases from the literature. Reiterating that this study was not intended to identify and/or recommend a specific model formulation and input parameters that should be imperatively selected to properly simulate LII signals, but that it instead aimed to highlight the relative strengths and weaknesses of each tested model and sub-model while proposing avenues into how to parameterize them, the following conclusions and recommendations were drawn.

- Composed of a limited number of mechanisms, standard Melton-based models are relatively straightforward to implement and parameterize while interestingly being easy to refine through the integration of additional sub-models and/or corrective factors (e.g., shielding effect, multiple scattering, etc.). Although the energy- and mass balance equations embedded within standard model formulations performed relatively well (once correctly parameterized) in the present work in capturing the fluence dependence of the peak LII responses below the sublimation threshold, their oversimplistic treatment proved to be unsuitable to properly mimic variations of the peak LII signals when fluences above $\sim$0.15 and $\sim$0.30 J cm^{-2} for EWs of 532 and 1064 nm are typically considered, respectively. Similarly, and regardless of the values set for the thermal and mass accommodation coefficients embedded within the conduction and sublimation terms, the standard model formulations tested failed to compute LII time decays matching their experimental counterparts over an extended range of laser fluences. Besides, the results obtained when attempting to reproduce the data from Bejaoui et al. (2015) led to conclude that considering a surface temperature- and gas temperature-dependent global accommodation coefficient can be considered as a good option to improve model predictions despite the significant uncertainties present in the literature respecting the potential temperature dependence of α_T.
- Even though they are more complex to implement and parameterize (especially due to the number of input parameters needing to be empirically set), refined models which include photolytic mechanisms (such as multiphoton absorption and nonthermal

photodesorption of carbon clusters, as examples) were shown to satisfactorily reproduce the relative lack of fluence dependence of the peak LII signals above the sublimation threshold. Furthermore, and despite their intrinsic complexity, parameterization of Michelsen-based models can still be attempted by implementing optimization procedures aimed at reducing the mean square deviation between measured and computed signals when the full lifetimes of the LII signals are considered for a wide range of fluences. The sensitivity analyses conducted in this work indeed confirmed that the properties and empirical factors embedded within refined models (e.g., $E(m)$, $B_{\lambda n}$, $\sigma_{\lambda n}$, etc.) influence the LII response differently as a function of the excitation wavelength, the laser fluence and the time. This feature hence allows to possibly identify unique sets of fitted parameters, provided the research area is correctly defined by setting physically relevant lower and upper boundaries. Caution should nonetheless be exercised when it comes to analyzing the validity of the soot properties and empirical factors derived using such a traditional fitting approach, since modern statistical frameworks based on Bayesian analyses is a must if proper model selection and/or parameterization are to be done. Furthermore, and notwithstanding their ability to reproduce the so-called plateau region of the fluence curves, the Michelsen-based models tested herein were alternatively found to be unsuitable to predict LII time decays matching those measured in the C_2H_4 and $CH_4/O_2/N_2$ flames over an extended range of fluences, which was notably traced to overpredicted soot heating and/or cooling, depending on the tested formulation and on the modeled dataset.

- While confirming that dU_{int}/dt must be computed as per Eq. (3), Eq. (4), whose use introduces a nonphysical source term in the energy equation, was found to lead to acceptable results when calculations are performed in the low fluence regime ($c_s \cdot T_p \cdot dM_p / dt \rightarrow 0$) while considering a constant c_s ($T_p \cdot dc_s/d T_p = 0$). It is, however, noteworthy that since physically erroneous peak particle temperatures are predicted when using Eq. (4), the latter should therefore be disregarded, as previously concluded by Liu & Snelling (2007) and Michelsen et al. (2008).
- The sensitivity analysis covering the values and/or empirical expressions proposed in the literature to represent ρ_s and c_s showed that these soot properties can significantly influence the peak soot temperatures estimated by calculation, and in turn, the simulated peak LII signals. Depending on the selected ρ_s and c_s, one can infer $E(m)$ values that vary significantly (up to ~11 % for calculations performed with the model from Melton (1984), for instance) when implementing an inverse calculation procedure aimed at fitting modeled fluence curves to measured ones. Nevertheless, and although identifying ρ_s and c_s values/expressions which should be recommended is far from trivial, it is believed that expressions taking into account the dependence of the density and heat capacity on the particle temperature and maturation level are more likely to properly account for the actual properties of soot under conditions relevant for LII applications. This hence paves the way for future works to be undertaken in order to validate and/or refine the expressions currently proposed in the literature, such as those from Michelsen (2003, 2021).
- Although often neglected in LII modeling works, aggregate properties drastically influence the LII process, hence the need to integrate corrective factors such as those accounting for SE and MS when information on α_T and $E(m)$ is to be derived from the modeling of experimentally-monitored signals. Indeed, including SE and MS typically leads to increasing α_T and decreasing $E(m)$ by ~26 % and ~12 % on average, based on the few calculations performed in this work. It should be noted that these values, which may vary more widely, depend strongly on the studied flame, the HAB, and thus, the soot maturation level, the considered EW, etc. (see Menanteau & Lemaire (2020) and Lemaire & Menanteau (2023a) for more details). It is, moreover, noteworthy that the assessment of the values taken by these key factors is fundamentally dependent on the selected model formulation and on its parametrization, as exemplified by the uncertainty ranges associated with the mean soot absorption functions derived herein, depending on the implemented model (i.e., 0.47 ± 0.13 and 0.54 ± 0.18 at 50 mm HAB in the C_2H_4 flame with EWs of 532 and 1064 nm, respectively, versus 0.32 ± 0.09 and 0.46 ± 0.15 at 9 and 15 mm HAB in the $CH_4/O_2/N_2$ flame). While evidencing the caution that must be exercised when attempting to infer soot properties and/or physical parameters governing the LII process using more or less refined modeling tools, the above results also lay bare the need to properly identify parameterized model formulations allowing to reproduce signals stemming from different databases, noting that contributing to provide insights which will help to boost trust in the validity of the properties and empirical factors estimated by calculation was one of the end-goals of this benchmarking analysis. The above observations, moreover, also support the need to further focus on measuring and/or better characterizing the temperature-, wavelength-, and particle maturity-dependent optical properties of soot while conducting complementary experimental/numerical studies to formulate expressions accounting for the variation of α_T as a function of T_p, T_g and soot H/C ratio, as well as other properties depicting the fine structure of the particle surface, in order to better represent the potential dependence of the thermal accommodation coefficient on the soot maturation stage.
- Since the mean free path typically exceeds the particle size during LII experiments conducted in flames at atmospheric pressure, heat conduction between soot particles and the surrounding gases can be consistently calculated assuming a free molecular flow regime. Modeling $\dot{Q}_{cond}$ considering a Fuchs equivalent sphere approach is still imperative when developing comprehensive simulation tools allowing to reproduce data obtained under widely varying conditions. This was notably exemplified through the modeling of the results obtained by Mi et al. (2021) and Zheng et al. (2023) in high pressure flames.
- Due to its marginal contribution to the energy balance, the radiation flux is often neglected in commonly used LII models. Neglecting $\dot{Q}_{rad}$ can, however, lead to the computation of LII time decays diverging from their counterparts issued from calculations performed while considering radiation with mean deviations globally comprised between 1 and 2 %. This observation thus indicates that caution should be exercised when attempting to evaluate the soot size by TiRe-LII at low fluences from the model-assisted processing of measured signals. Furthermore, it also supports the recommendation to consider $\dot{Q}_{rad}$ (whose corresponding sub-model is very straightforward to implement) to discard any potential issues related to the influence of this flux on the simulation of the soot cooling process.

- Although not of major concern at low fluences, the impact of annealing can become far from negligible when the temperature of laser-heated soot reaches values between ~2500 K (Michelsen, 2003) and ~4000 K (Cenker & Roberts, 2017). By modifying the structure and hence the properties (including optical ones) of the particles, annealing is likely to act on the way soot absorbs the incident light, which in turn may lead to improper simulations of the fluence dependence of the peak LII signals, among others. Despite the large uncertainties surrounding the formulation and parameterization of current annealing sub-models, the expressions recently proposed by Sipkens et al. (2019) and Liu (2024) to compute changes in the annealed fraction as a function of time were shown to be adapted to reproduce the experimental observations by Cenker and Roberts (2017). More experimental data, notably with young particles, are, however, required to pursue the preliminary works by Sipkens et al. (2019) and Liu (2024), and thus improve the predictive character of the models aimed at simulating the fine structure changes undergone by soot during heating.
- Like oxidation, thermionic emission mainly influences the LII responses at relatively high fluences. The impact of both these fluxes on modeled signals is, however, relatively marginal. The identification and recommendation of specific sub-models to account for these terms is therefore not truly a critical issue. Note that the expression of $\dot{Q}_{th}$ proposed by Mitrani et al. (2016) is still believed to be more relevant as it allows to account for the effects of the positive charge buildup in laser-heated nanoparticles increasing the energy barrier for further emission of electrons.
- Among all the model formulations tested in this work, the comprehensive simulation tool proposed by Lemaire & Menanteau (2023a) proved to be the only one capable of satisfactorily mimicking the LII signals measured by Goulay et al. (2013), Bejaoui et al. (2015), Lemaire et al. (Bejaoui, Lemaire, & Therssen, 2015; Lemaire, Bejaoui, & Therssen, 2013; Lemaire & Menanteau, 2021, 2023a), Mi et al. (2021), and Zheng et al. (2023) in laminar gaseous flames and turbulent spray flames of liquid fuels stabilized under atmospheric and high-pressure conditions, with EWs of 532 and 1064 nm. Here again, this observation tends to corroborate the conclusions by Michelsen (Michelsen, 2003; Michelsen et al., 2007) and Lemaire et al. (Lemaire & Menanteau, 2021, 2023a; Lemaire & Mobtil, 2015) regarding the relevance of integrating photolytic mechanisms such as multi-photon absorption and photodesorption of carbon clusters to properly simulate the fluence dependence of LII signals (notably above the sublimation threshold). It is, however, reiterated that this specific model should not be considered as universally valid, especially since it fails to reproduce the data from Goulay et al. (2013) at the highest fluences investigated therein. This hence strengthens the need for complementary works, including experimental ones, aimed at better characterizing the properties of young and mature soot (e.g., ρ_s, c_s, $E(m)$, $\sigma_{\lambda n}$, etc.) irradiated with high fluence laser pulses, in addition to further elucidating the processes likely to influence these properties (e.g., annealing and photolytic processes), and hence the ensuing radiative emissions from laser-heated particles.

Although the present benchmark evidences the crucial need for further research to advance the LII technique through a better prediction and/or interpretation of measured signals, it contributes to providing basic guidelines and insights into how to use current modeling tools. The comprehensive sensitivity analyses proposed throughout this paper will, moreover, likely help the reader better understand the relative importance of each energy flux and the impact of the terms embedded within the sub-models accounting for them, which should ultimately be of great interest for researchers looking to simulate and/or analyze data they measure through LII modeling.

CRediT authorship contribution statement

R. Lemaire: Writing – review & editing, Writing – original draft, Visualization, Validation, Supervision, Resources, Project administration, Methodology, Investigation, Funding acquisition, Formal analysis, Conceptualization. **S. Menanteau:** Writing – review & editing, Visualization, Validation, Resources, Investigation, Formal analysis.

Data availability

The datasets generated during and/or analyzed during the current study are available from the corresponding author on reasonable request.

Declaration of competing interest

The authors declare that they have no known competing financial interests or personal relationships that could have appeared to influence the work reported in this paper.

Acknowledgements

This research was supported by the Natural Sciences and Engineering Research Council of Canada (NSERC).

Appendix 1. Summary of the main features of a series of LII model formulations used in the literature

Table A1

Summary of the main features of a series of LII model formulations used in the literature (Melton, 1984; McCoy & Cha, 1974; Hofeldt, 1993; Smallwood et al., 2001; Snelling et al., 2000; Michelsen, 2003; Snelling et al., 2004; Bladh & Bengtsson, 2004; Dalzell & Sarofim, 1969; Liu et al., 2006a; Liu, Smallwood, & Snelling, 2005; Filippov & Rosner, 2000; Kock et al., 2006; Hofmann, Kock, & Schulz, 2007; Kock et al., 2006; Hofeldt, 1993; Hofmann et al., 2008; Hadef et al., 2010; 2013; Bladh et al., 2011a; 2011b; Bladh, Johnsson, & Bengtsson, 2008; Bladh et al., 2008; Charwath, Suntz, & Bockhorn, 2011; Bejaoui et al., 2015; Lemaire & Mobtil, 2015; Goulay et al., 2013; Mitrani et al., 2016; Chen et al., 2017; Hadwin et al., 2017; Cenker & Roberts, 2017; Hofmann et al., 2008; Betrancourt et al., 2017; Zhang et al., 2019; Bennett, Cenker, & Roberts, 2020; Lemaire & Menanteau, 2021; 2023a; Menanteau & Lemaire, 2022; Yon et al., 2015; Leider, Krikorian, & Young, 1973;Johnsson, Bladh, & Bengtsson, 2010; Török, Mannazhi, & Bengtsson, 2021; Sun et al., 2015; Desgroux, Lamoureux, & Faccinetto, 2024; Lemaire and Mobtil, 2015; Liu and Smallwood, 2013; Betrancourt et al., 2019; Cenker et al., 2015; Johnsson et al., 2013).

Ref.	dU_{int}/dt	$\dot{Q}_{abs}$	$\dot{Q}_{sub}$	$\dot{Q}_{cond}$	$\dot{Q}_{rad}$	$\dot{Q}_{ann}$	$\dot{Q}_{ox}$	$\dot{Q}_{th}$
(Melton, 1984)	$\rho_s \cdot c_s \cdot \pi/6 \cdot {D_p}^3 \cdot \mathrm{d}\,T_p/\mathrm{d}t$ with ρ_s =1900 kg m^{-3} and c_s=2260 J kg^{-1} K^{-1}	Mie equations for a spherical particle with $E(m)$=0.18 for λ_l=532 nm	$\Delta H_v/w_v \cdot \mathrm{d}M_p/\mathrm{d}t$. Only C_3 is assumed to sublime with α_M=1.00	Transition regime (McCoy & Cha, 1974), with α_T=0.90	Stefan-Boltzmann law $(\pi \cdot {D_p}^2 \cdot \sigma_{SB} \cdot (T_p^2 - T_g^2))$	Not considered	Not considered	Not considered
(Hofeldt, 1993)	$M_s \cdot \mathrm{d}(c_s \cdot T_p)/\mathrm{d}t$ with ρ_s=1000 kg m^{-3} and c_s=1500 J kg^{-1} K^{-1}	Rayleigh approximation with $E(m)$=0.24 and 0.20 for λ_l=532 and 1064 nm	Derived from Melton (1984), with α_M=0.90	Transition regime (McCoy & Cha, 1974), with α_T=0.90	$\int_0^\infty C_{abs} \cdot E_{b,\lambda}(T_p)\mathrm{d}\lambda$	Not considered	Not considered	Not considered
(Snelling et al., 2000; Smallwood et al., 2001)	Identical to Melton (1984), with ρ_s=2200 kg m^{-3} and c_s=2100 J kg^{-1} K^{-1}	Rayleigh approximation with $E(m)$=0.176 for λ_l=532 nm	Derived from Melton (1984), assuming that C_1 to C_7 (Snelling et al., 2000) and C_1 to C_5 (Smallwood et al., 2001) sublime with α_M=0.80 in Snelling et al. (2000) and 1.00 in Smallwood et al. (2001) (1)	Transition regime (McCoy & Cha, 1974), with α_T=0.90 (Smallwood et al., 2001)	Neglected (Snelling et al., 2000)	Not considered	Not considered	Not considered
(Michelsen, 2003)	$\pi/6 \cdot {D_p}^3 \cdot \mathrm{d}\,T_p/\mathrm{d}t \cdot [\rho_s \cdot c_s \cdot (1 - X_a - X_m) + \rho_a \cdot c_a \cdot X_a + \rho_m \cdot c_m \cdot X_m]$ with $\rho_s = 2303.1 - 7.3106 \times 10^{-2} \cdot T_p$, $\rho_a = 2600 - 1 \times 10^{-1} \cdot T_p$, $\rho_m = 2044.8 - 7.0809 \times 10^{-2} \cdot T_p$ while the values of the heat capacity of unannealed, annealed and melted soot fractions (i.e., $c_s = c_a$ and c_m) are expressed as a function of T_p (2)	Rayleigh approximation with $E(m) = \lambda^{1-\xi} \cdot \beta/(6 \cdot \pi)$ including specific ξ and β values for unannealed, annealed and melted soot fractions	Sub-model integrating thermal and nonthermal contributions from the unannealed and annealed particles, assuming that C_1 to C_{10} sublime with α_M=0.50 for C_1 and C_2, 0.10 for C_3 and 10^{-4} for C_4 to C_{10}	Transition regime (McCoy & Cha, 1974), with α_T=0.30	Planck function integrated over all wavelengths using the Rayleigh approximation $(199 \cdot \pi^5 \cdot {D_p}^3 \cdot (k_B \cdot T_p)^5 \cdot E(m)/(h \cdot (h \cdot c)^3))$	$(-\Delta H_{imig} \cdot k_{imig} \cdot N_d - \Delta H_{vmig} \cdot k_{vmig} \cdot N_d)/N_A$	$(\Delta H_{ox} + 2 \cdot \alpha_T \cdot C_p^{CO} \cdot T_p)/(2 \cdot w_1) \cdot (\mathrm{d}M_p/\mathrm{d}t)_{ox}$ assuming that CO is produced exclusively	Not considered
(Snelling et al., 2004)	$N_p \cdot \rho_s \cdot c_s \cdot \pi/6 \cdot {D_p}^3 \cdot \mathrm{d}\,T_p/\mathrm{d}t$ with ρ_s =1900 kg m^{-3} and c_s=2100 J kg^{-1} K^{-1}	Rayleigh approximation with $E(m) = 0.323 + 1.2546 \times 10^5 \cdot \lambda$, 0.395 or 0.42 for λ_l=1064 nm	Neglected (low fluence regime)	Expression similar to Snelling et al. (2000) and Smallwood et al. (2001), taking into account the shielding effect and setting α_T to 0.37	Neglected	Not considered	Not considered	Not considered
(Bladh & Bengtsson, 2004)	Identical to Melton (1984), with ρ_s=2200 kg m^{-3} and c_s=2100 J kg^{-1} K^{-1}	Identical to Snelling et al. (2000), with $E(m)$ calculated based on the data from Dalzell & Sarofim (1969) (i.e., 0.216 for λ_l=532 nm)	Identical to Snelling et al. (2000)	Identical to Snelling et al. (2000)	Neglected	Not considered	Not considered	Not considered
(Liu, Smallwood, & Snelling, 2005; Liu et al., 2006a)	Identical to Snelling et al. (2004), with ρ_s=1900 kg m^{-3} and c_s assumed to be the same as that of graphite	Rayleigh-Debye-Gans theory for polydisperse fractal aggregates with $E(m)$=0.40 for λ_l=1064 nm	Neglected (low fluence regime)	Fuchs approach based on Filippov & Rosner (2000), taking into account the shielding effect with α_T=0.37	Identical to Michelsen (2003)	Not considered	Not considered	Not considered
(Kock et al., 2006)	$\mathrm{d}(M_p, c_s, T_p)/\mathrm{d}t$ with ρ_s =1860 kg m^{-3} and $c_s = 1878 + 0.1082 \cdot T_p - 1.5149 \times 10^8/T_p^2$ J kg^{-1} K^{-1}	Not modeled (the maximum value of T_p being estimated by two-color pyrometry)	$2 \cdot \pi \cdot D_p \cdot D \cdot (\rho_s - \rho_\infty) \cdot f_c \cdot Kn_c \cdot \Delta h_v$ assuming that only C_3 sublimes with α_M=1.00	Transition regime $(2 \cdot \pi \cdot D_p \cdot \lambda_{cond} \cdot (T_p - T_g) \cdot f_h \cdot Kn_h)$, with α_T=1.00	Identical to Melton (1984)	Not considered	Not considered	Not considered

Ref.	$\mathbf{d}U_{\mathbf{int}}/\mathbf{d}t$	$\dot{Q}_{\mathbf{abs}}$	$\dot{Q}_{\mathbf{sub}}$	$\dot{Q}_{\mathbf{cond}}$	$\dot{Q}_{\mathbf{rad}}$	$\dot{Q}_{\mathbf{ann}}$	$\dot{Q}_{\mathbf{ox}}$	$\dot{Q}_{\mathbf{th}}$
(Hofmann, Kock, & Schulz, 2007) [3]	Identical to Kock et al. (2006)	Rayleigh approximation	$\Delta H_v/W_v \cdot (\pi \cdot D_p^2 \cdot W_v/N_A \cdot (1/N_{FM} + 1/N_c)^{-1})$, with N_{FM} and N_c depicting the flux term for the free molecular and continuum regime, respectively (see the equations provided in Hofmann, Kock, & Schulz (2007)), assuming that C_1 to C_7 sublime [1], [4]	Free molecular regime, continuum regime, transition regime (McCoy & Cha, 1974) and Fuchs approach	Identical to Melton (1984)	Not considered	Not considered	Not considered
(Michelsen et al., 2007) [5]	Identical to Melton (1984), with ρ_s and c_s expressed as in Michelsen (2003)	Refined sub-model accounting for saturation of the linear, single-photon absorption, and multiphoton absorption leading to C_2 photodesorption at high fluence [6]	Sub-model integrating thermal and nonthermal mechanisms, assuming that C_1 to C_5 sublime (only C_2 in the case of photodesorption), with α_M=0.50 for C_1 and C_2, 0.10 for C_3 and 10^{-4} for C_4 and C_5	Free molecular regime $(\pi \cdot D_p^2 \cdot \alpha_T \cdot P_g/(2 \cdot T_g) \cdot \sqrt{(R_m \cdot T_g)/2 \cdot \pi \cdot w_a \cdot (\gamma + 1)/(\gamma - 1) \cdot (T_p - T_g)}$, with α_T=0.30	Identical to Michelsen (2003), with re-absorption of background emission	Not considered	Identical to Michelsen (2003)	Richardson–Dushman approximation $4 \cdot \pi \cdot m_{el} \cdot (\pi \cdot D_p \cdot k_B \cdot T_p)^2/h^3 \cdot exp[-\phi/(k_B \cdot T_p)]$
(Bladh, Johnsson, & Bengtsson, 2008) [7]	Identical to Snelling et al. (2004), with ρ_s and c_s expressed as in Michelsen (2003)	Rayleigh-Debye-Gans theory for polydisperse fractal aggregates with $E(m) = 0.323 + 1.2546 \times 10^5 \cdot \lambda$ (Snelling et al., 2004)	Based on Hofeldt (1993); Snelling et al. (2000); Smallwood et al. (2001), considering the total area of the primary particles and assuming that C_1 to C_7 sublime with α_M=0.80 [1]	Fuchs approach, taking into account the shielding effect with α_T=0.30	Identical to Michelsen (2003)	Not considered	Not considered	Not considered
(Hofmann et al., 2008)	Identical to Melton (1984), with ρ_s=1860 kg m^{-3} and c_s expressed as in Kock et al. (2006)	Not modeled (the maximum value of T_p being estimated by two-color pyrometry)	Based on Snelling et al. (2000), with α_M=1.00 [1]	Free molecular regime, transition regime (McCoy & Cha, 1974) and Fuchs approach with α_T=0.25	Identical to Melton (1984)	Not considered	Not considered	Not considered
(Snelling et al., 2009)	Identical to Snelling et al. (2004), with ρ_s=1900 kg m^{-3} and c_s expressed as a function of T_p [8]	Identical to Snelling et al. (2000) and Smallwood et al. (2001), with $E(m)$=0.40 for λ_l=532 nm	Identical to Smallwood et al. (2001), with α_M=0.90	Identical to Liu et al. (2006a) with α_T=0.44	Identical to Liu et al. (2006a)	Not considered	Not considered	Not considered
(Hadef et al., 2010; Hadef et al., 2013)	Identical to Melton (1984), with ρ_s and c_s expressed as in Michelsen (2003)	Rayleigh approximation, with $E(m) = 0.323 + 1.2546 \times 10^5 \cdot \lambda$ (Snelling et al. (2004)	$\Delta H_v \cdot (\pi \cdot D_p^2 \cdot \alpha_M \cdot P_v)/(R_p \cdot T_p) \cdot [(R_m \cdot T_p)/(2 \cdot \pi \cdot w_v)]^K$ [9], assuming that C_1 to C_7 sublime, with α_M=0.50 in Hadef et al. (2010) and α_M=0.50 for C_1 and C_2, 0.10 for C_3 and 10^{-4} for C_4 to C_7 in Hadef et al. (2013) [1]	Free molecular regime (as in Michelsen et al. (2007)), with α_T=0.30	Planck function integrated over all wavelengths using the Rayleigh approximation	Not considered	Not considered	Not considered
(Bladh et al., 2011a; Bladh et al., 2011b)	Identical to Bladh, Johnsson, & Bengtsson (2008)	Rayleigh approximation, with $0.21<E(m)<0.45$ for λ_l=1064 nm (Bladh et al., 2011a)	Neglected (low fluence regime)	Identical to Bladh, Johnsson, & Bengtsson (2008), with α_T=0.48 in Bladh et al. (2011a) and 0.37 in Bladh et al. (2011b)	Neglected	Not considered	Not considered	Not considered

Ref.	$\mathbf{d}U_{\mathbf{int}}/\mathbf{d}t$	$\dot{Q}_{\mathbf{abs}}$	$\dot{Q}_{\mathbf{sub}}$	$\dot{Q}_{\mathbf{cond}}$	$\dot{Q}_{\mathbf{rad}}$	$\dot{Q}_{\mathbf{ann}}$	$\dot{Q}_{\mathbf{ox}}$	$\dot{Q}_{\mathbf{th}}$
(Charwath, Suntz, & Bockhorn, 2011)	Identical to Melton (1984), with no value specified for ρ_s and c_s	Rayleigh approximation, with $E(m)$=0.23 for λ_l=532 nm	Identical to Hadef et al. (2010), assuming that only C_3 sublimes with K=0.4 and α_M=0.90	Transition regime (McCoy & Cha, 1974), with α_T=0.28	Identical to Michelsen (2003)	Not considered	Not considered	Not considered
(Liu & Smallwood, 2013) [10]	Identical to Melton (1984), with no value specified for ρ_s and c_s	Rayleigh approximation, with $E(m)$=0.40 for λ_l=1064 nm	Identical to Hadef et al. (2010), assuming that only C_3 sublimes, with K=0.5 and α_M=0.77 (Michelsen et al., 2007) [1]	Transition regime (McCoy & Cha, 1974), with α_T=0.37	Identical to Liu, Smallwood, & Snelling (2005)	Not considered	Not considered	Not considered
(Bejaoui et al., 2015) [11]	Identical to Snelling et al. (2004), with ρ_s=1900 kg m^{-3} and c_s=2100 J kg^{-1} K^{-1}	Rayleigh approximation, with 0.22<$E(m)$<0.37 for λ_l=1064 nm	Identical to Michelsen et al. (2007), with α_M=0.20 for C_1 and C_2, 0.03 for C_3 and 10^{-4} for C_4 and C_5	Identical to Liu, Smallwood, & Snelling (2005) and Liu et al. (2006a), considering a free molecular regime with α_T=0.30	Neglected	Not considered	Not considered	Not considered
(Lemaire & Mobtil, 2015) [12]	Identical to Melton (1984), with ρ_s and c_s taken as in Michelsen (2003)	Identical to Michelsen et al. (2007), with $E(m)$=0.286 for λ_l=532 nm	Identical to Michelsen et al. (2007)	Identical to Michelsen et al. (2007)	Planck function integrated over all wavelengths, with re-absorption of background emission using the wavelength-dependent expression of E(m) issued from Goulay et al. (2013)	Not considered	Identical to Michelsen (2003)	Identical to Michelsen et al. (2007)
(Mitrani et al., 2016)	Identical to Michelsen (2003)	Rayleigh approximation	Issued from Michelsen et al. (2007), assuming that C_1 to C_5 sublime [1]	Transition regime (McCoy & Cha, 1974)	Identical to Michelsen (2003)	Not considered	Not considered	Model from Michelsen et al. (2007) including the effects of the positive charge buildup
(Chen et al., 2017)	Identical to Melton (1984), with ρ_s=1900 kg m^{-3} and c_s=2100 J kg^{-1} K^{-1}	Identical to Bladh, Johnsson, & Bengtsson (2008)	Issued from Snelling et al. (2000), with α_M=1.00	Identical to Liu, Smallwood, & Snelling (2005) and Liu et al. (2006a), considering a free molecular regime with α_T=0.30	Identical to Michelsen (2003)	Not considered	Not considered	Not considered
(Hadwin et al., 2017)	Identical to Melton (1984), with ρ_s=1900 kg m^{-3} and c_s expressed as in Snelling et al. (2009)	Rayleigh approximation, with $E(m)$=0.40 for λ_l=1064 nm	Identical to Hadef et al. (2010), with α_M=0.77 [1]	Identical to Michelsen et al. (2007), with α_T=0.37	Neglected	Not considered	Not considered	Not considered
(Cenker & Roberts, 2017)	Identical to Melton (1984), with ρ_s=1860 kg m^{-3} and c_s expressed as in Michelsen (2003)	Identical to Michelsen (2003), with $E(m) = 0.323 + 1.2546 \times 10^5 \cdot \lambda$ (Snelling et al., 2004)	Identical to Hofmann et al. (2008)	Fuchs approach including a shielding factor calculated based on the work from Johnsson et al. (2013), with α_T=0.37	Identical to Melton (1984)	Identical to Michelsen (2003)	Not considered	Identical to Mitrani et al. (2016)

Ref.	$\mathbf{d}U_{\mathbf{int}}/\mathbf{d}t$	$\dot{Q}_{\mathbf{abs}}$	$\dot{Q}_{\mathbf{sub}}$	$\dot{Q}_{\mathbf{cond}}$	$\dot{Q}_{\mathbf{rad}}$	$\dot{Q}_{\mathbf{ann}}$	$\dot{Q}_{\mathbf{ox}}$	$\dot{Q}_{\mathbf{th}}$
(Betrancourt et al., 2017)	Identical to Melton (1984), with ρ_s=1300 kg m^{-3} and c_s expressed as a function of T_p [8]	Rayleigh approximation, with 0.23<$E(m)$<0.27 for λ_i=1064 nm	Identical to Smallwood et al. (2001), with 0.01<α_M<0.04 [1]	Free molecular regime (as in Michelsen et al. (2007), but using temperature-dependent γ), with α_T=0.35	Neglected	Not considered	Not considered	Not considered
(Zhang et al., 2019)	Identical to Melton (1984), with no value specified for ρ_s and c_s	Rayleigh approximation, with $E(m)$=0.40 for λ_i=1064 nm	Identical to Smallwood et al. (2001), with α_M=0.2	Transition regime (McCoy & Cha, 1974), with α_T=0.26	Neglected	Not considered	Not considered	Not considered
(Bennett, Cenker, & Roberts, 2020) [13]	Based on Michelsen et al. (2007), with ρ_s=1860 kg m^{-3} and no value specified for c_s	Rayleigh approximation, with $E(m)$=0.40	Identical to Michelsen (2003)	Transition regime (McCoy & Cha, 1974), with α_T=0.37	Planck function integrated over all wavelengths	Not considered	Identical to Michelsen (2003)	Identical to Michelsen (2003)
(Menanteau & Lemaire, 2020)	Identical to Michelsen (2003), while neglecting soot melting	Identical to Michelsen et al. (2007), with $E(m)$=0.29 for λ_i=1064 nm	Identical to Michelsen (2003)	Free molecular regime (as in Michelsen et al. (2007)) and Fuchs approach, taking into account the shielding effect with α_T=0.47	Planck function integrated over all wavelengths with re-absorption of background emission	Identical to Michelsen (2003)	Issued from Michelsen (2003) while selecting the temperature-dependent enthalpies of formation of CO issued from Michelsen et al. (2008)	Identical to Michelsen et al. (2007)
(Lemaire & Menanteau, 2021; Menanteau & Lemaire, 2022; Lemaire & Menanteau, 2023a)	Identical to Michelsen (2003), while neglecting soot melting	Identical to Michelsen et al. (2007), while integrating the correction factor for internal multiple scattering from Yon et al. (2015), with $E(m)$=0.38 ± 0.15 and 0.29 ± 0.11 for λ_i=266 and 355 nm versus 0.25 ± 0.09 for λ_i=532 and 1064 nm	Identical to Michelsen (2003)	Fuchs approach, taking into account the shielding effect, with α_T=0.49	Planck function integrated over all wavelengths, with re-absorption of background emission	Identical to Michelsen (2003)	Identical to Menanteau & Lemaire (2020)	Identical to Michelsen et al. (2007) in Menanteau & Lemaire (2022) and identical to Mitrani et al. (2016) in Lemaire & Menanteau (2021; Lemaire & Menanteau (2023)

[1] Properties related to the soot evaporation rate (i.e., the soot vapor molecular weight (w_V), vapor pressure (P_V) and heat of vaporization (ΔH_V)) issued from polynomial functions fitted based on the data from Leider, Krikorian, & Young (1973)

[2] $c_s = (R/a_4)\cdot\left\{a_1\cdot(\theta_1/T_p)^2\cdot exp(\theta_1/T_p)\cdot\left[exp(\theta_1/T_p)-1\right]^{-2}+a_2\cdot(\theta_2/T_p)^2\cdot exp(\theta_2/T_p)\cdot\left[exp(\theta_2/T_p)-1\right]^{-2}+a_3\cdot T_p\right\}$, the values of the coefficients a_1, a_2, a_3, a_4, θ_1, θ_2 and θ_3 being reported in Leider, Krikorian, & Young (1973)

[3] Model then implemented by Cenker et al. (2015), selecting the properties of graphite from Johnsson, Bladh, & Bengtsson (2010), an $E(m)$ of 0.40 for λ_i=1064 nm and an α_T of 0.25 while neglecting sublimation and considering the Fuchs approach for the conduction sub-model.

[4] Molecular cross-sections of the vapor molecules issued from a polynomial function fitted based on the data from Michelsen (2003).

[5] Only the model proposed by Michelsen is presented in the table, noting that different model formulations proposed by other authors are also reported in Michelsen et al. (2007).

[6] $\dot{Q}_{abs} = \pi\cdot {D_p}^2\cdot\varepsilon_\lambda/4\cdot f_1\cdot B_{\lambda1}/q_1\cdot\left\{1-exp\left[-F\cdot q_{exp}(t)/B_{\lambda1}\right]\right\}+\sigma_{\lambda n}\cdot\pi\cdot {D_p}^3\cdot N_{ss}/6\cdot B_{\lambda n}^n/q_n\cdot\left\{1-exp\left[-\left(F\cdot q_{exp}(t)/B_{\lambda n}\right)^n\right]\right\}$.

[7] Model then implemented by Johnsson, Bladh, & Bengtsson (2010); Sun et al. (2015); Török, Mannazhi, & Bengtsson (2021), although an $E(m)$ of 0.40 for λ_i=1064 nm was selected in Johnsson, Bladh, & Bengtsson (2010), while a free molecular regime with an α_T of 0.37 was considered in Sun et al. (2015).

[8] $c_s(0-1200\,K) = -9.7768\times10^{-4}+2.7943\times10^{-4}\cdot T_p+1.4554\times10^{-5}\cdot T_p^2-3.4432\times10^{-8}\cdot T_p^3+3.6700\times10^{-11}\cdot T_p^4-1.9485\times10^{-14}\cdot T_p^5+4.1802\times10^{-18}\cdot T_p^6$ and $c_s(1200-5500K) = 2.9497\times10^{-1}+2.9614\times10^{-3}\cdot T_p-2.1232\times10^{-6}\cdot T_p^2+8.1901\times10^{-10}\cdot T_p^3-1.7516\times10^{-13}\cdot T_p^4+1.9628\times10^{-17}\cdot T_p^5-8.9817\times10^{-22}\cdot T_p^6$ (Michelsen et al., 2007).

[9] The value of the exponent K being set to 0.5 in Hadef et al. (2010) versus 0.4 in the model used by Hadef in Michelsen et al. (2007) to account for the non-ideality of the ambient gases and desorbed clusters.

[10] Model subsequently used in Betrancourt et al. (2019) as well as in Desgroux, Lamoureux, & Faccinetto (2024) where the radiation flux was then neglected.

[11] The so-called "extended LII model" is described in the table, noting that a "base model" was also used in Bejaoui et al. (2015). The latter was identical to that described in the table, except for the sublimation term, which was expressed as in Hadef et al. (2010), assuming that C_1 to C_7 sublime with α_M=0.77 [1].

[12] The so-called "refined model" is described in the table, noting that a "standard model" was also used in Lemaire & Mobtil (2015). The latter was similar to that described in the table, except for the absorption term, which was expressed as in Snelling et al. (2000); Smallwood et al. (2001), with an $E(m)$ of 0.286 for λ_i=532 nm, the sublimation term, which was expressed as in Hadef et al. (2010), assuming that C_1 to C_5 sublime with K=0.5 and α_M=0.8 (properties related to the soot evaporation rate being issued from Michelsen (2003)) and $\dot{Q}_{ox}$ and $\dot{Q}_{th}$ which were not activated.

[13] Model also integrating a theoretical term aimed at simulating the change of local gas temperature based on tracking of energy transferred from a single particle to the surrounding gas probe volume via conduction and sublimation.

Appendix 2. Nomenclature

A_0	pre-exponential factor of the Arrhenius-based relation accounting for the progression of the soot annealed fraction in the models proposed by Sipkens et al. (2019) and Liu (2024)	$[s^{-1}\ m]$
B_j	parameter representing the influence of diffusive and convective mass and heat transfer during sublimation	$[bar]$
$B_{\lambda 1}$	empirically determined saturation coefficient for linear absorption, used in model 4	$[J\ cm^{-2}]$
$B_{\lambda 1,a}$	empirically determined saturation coefficient for linear absorption of annealed soot in model 5	$[J\ cm^{-2}]$
$B_{\lambda 1,s}$	empirically determined saturation coefficient for linear absorption of unannealed soot in model 5	$[J\ cm^{-2}]$
$B_{\lambda a}$	empirically determined saturation coefficient related to the removal of carbon clusters from the annealed particle by photodesorption, used in model 3 (0.9 according to Michelsen (2003))	$[cm^4\ J^{-2}]$
$B_{\lambda n}$	empirically determined saturation coefficient for multi-photon absorption, used in model 4	$[J\ cm^{-2}]$
$B_{\lambda n,a}$	empirically determined saturation coefficient for multi-photon absorption of annealed soot particles in model 5	$[J\ cm^{-2}]$
$B_{\lambda n,s}$	empirically determined saturation coefficient for multi-photon absorption of unannealed soot particles in model 5	$[J\ cm^{-2}]$
$B_{\lambda s}$	empirically determined saturation coefficient related to the removal of carbon clusters from the unannealed particle by photodesorption, used in model 3 (0.4 according to Michelsen (2003))	$[cm^4\ J^{-2}]$
c	speed of light (2.998×10^{10})	$[cm\ s^{-1}]$
c_a	heat capacity of annealed soot	$[J\ g^{-1}\ K^{-1}]$
$C_{abs,a}$	absorption cross-section of the annealed fraction of aggregated soot particles	$[cm^2]$
$C_{abs,s}$	absorption cross-section of the unannealed fraction of aggregated soot particles	$[cm^2]$
$C_{abs,a}^{multi}$	absorption cross-section of the annealed fraction of aggregated soot particles in model 5	$[cm^2]$
$C_{abs,s}^{multi}$	absorption cross-section of the unannealed fraction of aggregated soot particles in model 5	$[cm^2]$
c_{el}	charge of an electron (1.60218×10^{-19})	$[C]$
c_m	heat capacity of liquid carbon	$[J\ g^{-1}\ K^{-1}]$
C_p	molar heat capacity of the surrounding gases at constant pressure	$[J\ mol^{-1}\ K^{-1}]$
C_p^{CO}	molar heat capacity of CO fitted from the NIST-JANAF database (Chase, 1998)	$[J\ mol^{-1}\ K^{-1}]$
$C_p^{O_2}$	molar heat capacity of O_2 fitted from the NIST-JANAF database (Chase, 1998)	$[J\ mol^{-1}\ K^{-1}]$
c_s	heat capacity of unannealed soot	$[J\ g^{-1}\ K^{-1}]$
D	diffusion coefficient of the vapor into gas	$[m^2\ s^{-1}]$
D_h	scaling factor involved in the estimation of D_{HC}: $D_h = 1.99345 + 0.30224 \cdot \alpha_T - 0.11276 \cdot {\alpha_T}^2$	$[-]$
D_{HC}	equivalent heat conduction diameter	$[cm]$
D_p	primary particle diameter	$[cm]$
$E(m)$	dimensionless refractive index function of unannealed soot	$[-]$
E_A	activation energy of the Arrhenius-based relation accounting for the progression of the soot annealed fraction in the models proposed by Sipkens et al. (2019) and Liu (2024)	$[J\ mol^{-1}]$
$E_a(m)$	dimensionless refractive index function of annealed soot	$[-]$
$E_{b,\lambda}$	blackbody spectral irradiance	$[W\ m^{-2}\ \mu m]$
F	laser fluence	$[J\ cm^{-2}]$
f	dimensionless Eucken correction to the thermal conductivity of a polyatomic gas	$[-]$
f_1	empirical scaling factor for linear absorption of annealed soot (Michelsen et al., 2007)	$[-]$
$f_{1,a}$	empirical scaling factor for linear absorption of annealed soot in model 5	$[-]$
$f_{1,s}$	empirical scaling factor for linear absorption of unannealed soot in model 5	$[-]$
f_a	absorption empirical scaling factor related to annealed soot (Michelsen, 2003)	$[-]$
f_c	empirical function used in Kock et al. (2006)	$[-]$
f_h	empirical function used in Kock et al. (2006)	$[-]$
h	Planck constant (6.626×10^{-34})	$[J\ s]$
h_{λ,N_p}	correction factor for multiple scattering within soot aggregates	$[-]$
K	dimensionless exponent used to define flux of sublimation clusters away from the surface	$[-]$
k_B	Boltzmann constant (1.381×10^{-23})	$[J\ K^{-1}]$
k_{diss}	rate constant for pyrolysis of annealed particles $k_{diss} = 1 \times 10^{18} \cdot exp[-9.6 \times 10^5 / (R \cdot T_p)]$ (Michelsen, 2003)	$[s^{-1}]$
k_{el}	Coulomb constant (8.987×10^9)	$[N\ m^2\ C^{-2}]$
k_g	heat conduction coefficient of surrounding gas	$[W\ cm^{-1}\ K^{-1}]$
k_h	scaling factor involved in the estimation of D_{HC}: $k_h = 1.04476 + 0.22329 \cdot \alpha_T + 7.14286 \cdot 10^{-3} \cdot {\alpha_T}^2$ $(-)$	$[-]$
k_{imig}	rate constant for interstitial migrations within annealed particles: $k_{imig} = 1 \times 10^8 \cdot exp[-8.3 \times 10^4 / (R \cdot T_p)]$ (Michelsen, 2003)	$[s^{-1}]$
kn_c	Knudsen number defined in Kock et al. (2006)	$[-]$
kn_h	Knudsen number defined in Kock et al. (2006)	$[-]$
$k_{ox,a}$	oxidation rate constant of annealed soot	$[s^{-1}\ cm^{-2}]$
$k_{ox,s}$	oxidation rate constant of unannealed soot	$[s^{-1}\ cm^{-2}]$
k_p	Boltzmann constant in effective pressure units (1.38065×10^{-22})	$[bar\ cm^3\ K^{-1}]$
k_{vmig}	rate constant for vacancy migrations within annealed particles: $k_{vmig} = 1.5 \times 10^{17} \cdot exp[-6.7 \times 10^5 / (R \cdot T_p)]$ (Michelsen, 2003)	$[s^{-1}]$
$k_{\lambda a}$	rate constant for removal of carbon clusters from the annealed particle by nonthermal photodesorption, used in model 3	$[s^{-1}]$
$k_{\lambda n}$	rate constant for removal of carbon clusters by nonthermal photodesorption, used in model 4	$[s^{-1}]$
$k_{\lambda n,a}$	rate constant for removal of C_2 from annealed by photodesorption in model 5	$[s^{-1}]$

(continued on next page)

(*continued*)

$k_{\lambda n,s}$	rate constant for removal of C_2 from unannealed by photodesorption in model 5	$[s^{-1}]$
$k_{\lambda s}$	rate constant for removal of carbon clusters from the unannealed particle by nonthermal photodesorption, used in model 3	$[s^{-1}]$
m_{el}	mass of an electron (9.1095×10^{-35})	$[J\,s^2\,cm^{-2}]$
M_p	primary particle mass	$[g]$
M_s	mass concentration of particles defined in Hofeldt (1993)	$[g\,m^{-3}]$
n	estimated number of photons needing to be absorbed to photodesorb C_2 clusters	[−]
N_A	Avogadro constant (6.02214×10^{23})	$[mol^{-1}]$
N_c	number of atoms in the primary particles: $N_c = M_p \cdot N_A / w_1$	[−]
N_d	number of lattice defects in the particles	[−]
N_{FM}	flux term for the free molecular regime defined in Hofmann et al. (2007)	$[W]$
N_C	flux term for the continuum regime defined in Hofmann et al. (2007)	$[W]$
N_p	number of primary particles in an aggregate	[−]
N_{ss}	density of carbon atoms on the surface of unannealed soot particles (2.8×10^{15} according to Michelsen (2003))	$[cm^{-2}]$
N_{sa}	density of carbon atoms on the surface of annealed soot particles (3.8×10^{15} according to Michelsen (2003))	$[cm^{-2}]$
N_{tot}	aggregate number density	[−]
$p(N_p)$	probability density function of aggregate size	[−]
P_{diss}	effective pressure issued from the rate of thermal photodesorption from annealed particles	$[bar]$
P_g	ambient pressure	$[bar]$
$P_{sat}^{C_j}$	saturation partial pressure of vaporized carbon clusters C_j	$[bar]$
P_v	saturation partial pressure of vaporized carbon clusters used in models 1 & 2	$[bar]$
$P_{\lambda a}$	effective pressure calculated based on the rate of nonthermal photodesorption of C_j clusters from annealed particles	$[bar]$
$P_{\lambda s}$	effective pressure calculated based on the rate of nonthermal photodesorption of C_j clusters from unannealed particles	$[bar]$
q_1	normalization constant of the integrated laser temporal profile defined in Michelsen et al. (2007)	$[s]$
$\dot{Q}_{abs}$	rate of energy increase by laser absorption	$[W]$
$\dot{Q}_{ann}$	rate of energy increase by annealing	$[W]$
$\dot{Q}_{cond}$	rate of energy increase by thermal conduction	$[W]$
$\dot{Q}_{cond,FM}$	rate of energy loss by conduction in the free molecular regime	$[W]$
$\dot{Q}_{cond,C}$	rate of energy loss by conduction in the continuum regime	$[W]$
q_{exp}	normalized laser irradiance	[−]
q_n	normalization constant of the integrated laser temporal profile raised to the nth power (Michelsen et al., 2007)	$[s]$
$\dot{Q}_{ox}$	rate energy increase by particle oxidation	$[W]$
$\dot{Q}_{rad}$	rate of energy loss by radiative emission	$[W]$
$\dot{Q}_{sub}$	rate of energy loss by sublimation	$[W]$
$\dot{Q}_{th}$	rate of energy loss by thermionic emission	$[W]$
R	universal gas constant (8.3145)	$[J\,mol^{-1}\,K^{-1}]$
R_m	universal gas constant expressed in effective mass units (8.3145×10^7)	$[g\,cm^2\,mol^{-1}\,K^{-1}\,s^{-2}]$
R_p	universal gas constant in expressed effective pressure units (83.145)	$[bar\,cm^3\,mol^{-1}\,K^{-1}]$
t	time	$[s]$
T_f^{CO}	temperature at which CO molecules are emitted from oxidizing soot (790 according to Michelsen et al. (2008))	$[K]$
T_g	ambient gas temperature	$[K]$
t_l	laser pulse duration	$[s]$
T_p	particle temperature	$[K]$
T_{ref}	reference temperature (0)	$[K]$
T_δ	limiting sphere temperature within the Fuchs heat conduction model	$[K]$
U_{int}	internal energy of soot particles	$[J]$
U_j	ejection speed of C_j away from the particle surface	$[cm\,s^{-1}]$
u_p	specific particle internal energy	$[J\,g^{-1}]$
w_a	molecular weight of air (28.74)	$[g\,mol^{-1}]$
w_c	molecular weight of carbon atom used in Eq. (35) (12.011)	$[g\,mol^{-1}]$
w_H	molecular weight of hydrogen atom used in Eq. (35) (1.008)	$[g\,mol^{-1}]$
w_j	molecular weight of C_j species (j × 12.011)	$[g\,mol^{-1}]$
w_v	average molecular weight of carbon cluster used in models 1 & 2	$[g\,mol^{-1}]$
X_a	mass fraction annealed	[−]
X_d	initial defect density (1×10^{-2} according to Dunne et al. (1997))	$[atom^{-1}]$
X_m	mass fraction melted	[−]
α_j	mass accommodation coefficient of vaporized species C_j (with $\alpha_1 = \alpha_2 = 0.5$, $\alpha_3 = 0.1$ and $\alpha_4 = \alpha_5 = 0.0001$ according to Michelsen (2003))	[−]
α_M	mass accommodation coefficient used in models 1 & 2	[−]
α_T	thermal accommodation coefficient	[−]
β	scaling factor used in the equation $E(m) = \lambda^{1-\xi} \cdot \beta/(6 \cdot \pi)$	$[cm^x]$
δ	distance between the equivalent heat conduction radius and the limiting sphere of the Fuchs heat conduction model	$[cm]$
γ	heat capacity ratio (C_p / C_v) for the gas surrounding the particles	[−]
γ^*	mean heat capacity ratio	[−]

(*continued on next page*)

(*continued*)

ΔH_{diss}	enthalpy of formation of C_j clusters by thermal sublimation of annealed soot	$[J\,mol^{-1}]$
ΔH_{imig}	enthalpy related to interstitial migrations (-1.9×10^4 as estimated in Michelsen (2003) based on the data from Konno & Sinclair (1995))	$[J\,mol^{-1}]$
ΔH_j	enthalpy of formation of carbon vapor species C_j (Michelsen, 2003): $\Delta H_1 = -5.111 \cdot T_p + 7.266 \times 10^5$, $\Delta H_2 = -12.326 \cdot T_p + 8.545 \times 10^5$, $\Delta H_3 = -26.921 \cdot T_p + 8.443 \times 10^5$, $\Delta H_4 = -2.114 \times 10^{-3} \cdot {T_p}^2 - 7.787 \cdot T_p + 9.811 \times 10^5$ and $\Delta H_5 = -2.598 \times 10^{-3} \cdot {T_p}^2 - 7.069 \cdot T_p + 9.898 \times 10^5$	$[J\,mol^{-1}]$
ΔH_{ox}	enthalpy of the reaction $2C + O_2 \rightarrow 2CO$ (-2.215×10^5)	$[J\,mol^{-1}]$
ΔH_v	average enthalpy of formation of carbon clusters used in Eq. (14)	$[J\,mol^{-1}]$
ΔH_{vmig}	enthalpy related to vacancy migrations (-1.4×10^5 as derived from the works of Marcos et al. (1997) and Ewels, Heggie, & Briddon (2002))	$[J\,mol^{-1}]$
$\Delta H_{\lambda,a}$	enthalpy required to photodesorb C_j clusters from annealed particles	$[J\,mol^{-1}]$
$\Delta H_{\lambda,s}$	enthalpy required to photodesorb C_j clusters from unannealed particles	$[J\,mol^{-1}]$
$\Delta\phi$	positive charge buildup	$[J]$
ε_λ	Emissivity at a wavelength λ as defined in Michelsen et al. (2007)	$[-]$
λ	wavelength	$[cm]$
λ_{cond}	thermal conductivity of gas	$[W\,m^{-1}\,K^{-1}]$
λ_l	laser-excitation wavelength	$[cm]$
ξ	dispersion exponent used in the equation $E(m) = \lambda^{1-\xi} \cdot \beta/(6 \cdot \pi)$	$[-]$
ρ_a	density of annealed soot	$[g\,m^{-3}]$
ρ_m	density of liquid carbon	$[g\,m^{-3}]$
ρ_s	density of unannealed soot	$[g\,m^{-3}]$
ρ_∞	density of vapor at infinity	$[g\,m^{-3}]$
$\overline{\sigma}$	average molecular cross-section for C_1 to C_7 vaporized clusters	$[-]$
σ_{SB}	Stefan–Boltzmann constant (5.6704×10^{-12})	$[W\,cm^{-2}\,K^{-4}]$
$\sigma_{\lambda a}$	empirically determined cross-section for photodesorption of carbon clusters from the annealed particle, used in model 3	$[cm^{-1}\,s^{-1}]$
$\sigma_{\lambda n}$	empirically determined cross-section for removal of C_2 clusters by photodesorption, used in model 4	$[cm^{2n-1}\,J^{1-n}]$
$\sigma_{\lambda n,a}$	empirically determined cross-section for removal of C_2 clusters by photodesorption from annealed soot particles in model 5	$[cm^{2n-1}\,J^{1-n}]$
$\sigma_{\lambda n,s}$	empirically determined cross-section for removal of C_2 clusters by photodesorption from unannealed soot particles in model 5	$[cm^{2n-1}\,J^{1-n}]$
$\sigma_{\lambda s}$	empirically determined cross-section for photodesorption of carbon clusters from the unannealed particle, used in model 3	$[cm^{-1}\,s^{-1}]$
Φ	equivalence ratio	$[-]$
ϕ	work function	$[J]$

Acronyms

DoE	design of experiments (first appearance in section 2.1)
EW	excitation wavelength (first appearance in section 2.1)
HAB	height above the burner (first appearance in section 3)
IR	infrared (first appearance in section 1)
LEM	laser extinction method (first appearance in section 1)
LII	laser-induced incandescence (first appearance in the abstract)
LIF	laser-induced fluorescence (first appearance in section 1)
LMI	laser-modulated incandescence (first appearance in section 2.1)
MPA	multi-photon absorption (first appearance in section 5.3.1)
MRD	mean relative deviation (first appearance in section 5.1.2)
MS	multiple scattering (first appearance in section 5.1.1)
NTP	nonthermal photodesorption (first appearance in section 5.3.1)
OOB	out-of-bounds (first appearance in section 5.1.1)
PMT	photomultiplier tube (first appearance in section 6)
PSLII	peak LII signal (first appearance in section 5.3.1)
SE	shielding effect (first appearance in section 2.1)
SLII	LII signal (first appearance in section 5.3.1)
TEM	transmission electron microscopy (first appearance in section 1)
TiRe-LII	Time-resolved laser-induced incandescence (first appearance in section 2.1)

Data availability

Data will be made available on request.

References

Arden Pope, C., III, & Dockery, D. W. (2006). Health effects of fine particulate air pollution: Lines that connect. *Journal of the Air; Waste Management Association, 56*, 709–742. https://doi.org/10.1080/10473289.2006.10464485

Bejaoui, S., Batut, S., Therssen, E., Lamoureux, N., Desgroux, P., & Liu, F. (2015). Measurements and modeling of laser-induced incandescence of soot at different heights in a flat premixed flame. *Applied Physics B, 118*, 449–469. https://doi.org/10.1007/s00340-015-6014-3

Bejaoui, S., Lemaire, R., Desgroux, P., & Therssen, E. (2014). Experimental study of the E(m,λ)/E(m,1064) ratio as a function of wavelength, fuel type, height above the burner and temperature. *Applied Physics B, 116*, 313–323. https://doi.org/10.1007/s00340-013-5692-y

Bejaoui, S., Lemaire, R., & Therssen, E. (2015). Analysis of laser-induced fluorescence spectra obtained in spray flames of diesel and rapeseed methyl ester using the multiple-excitation wavelength laser-induced incandescence technique with IR, UV and visible excitations. *Combustion Science and Technology, 187*, 906–924. https://doi.org/10.1080/00102202.2014.973949

Bennett, A. M., Cenker, E., & Roberts, W. L. (2020). Effects of soot volume fraction on local gas heating and particle sizing using laser induced incandescence. *Journal of Aerosol Science, 149*, Article 105598. https://doi.org/10.1016/j.jaerosci.2020.105598

Betrancourt, C., Liu, F., Desgroux, P., Mercier, X., Faccinetto, A., Salamanca, M., Ruwe, L., Kohse-Höinghaus, K., Emmrich, D., Beyer, A., Gölzhäuser, A., & Tritscher, T. (2017). Investigation of the size of the incandescent incipient soot particles in premixed sooting and nucleation flames of n-butane using LII, HIM, and 1 nm-SMPS. *Aerosol Science & Technology, 51*, 916–935. https://doi.org/10.1080/02786826.2017.1325440

Betrancourt, C., Mercier, X., Liu, F., & Desgroux, P. (2019). Quantitative measurement of volume fraction profiles of soot of different maturities in premixed flames by extinction-calibrated laser-induced incandescence. *Applied Physics B, 125*, 16. https://doi.org/10.1007/s00340-018-7127-2

Bladh, H., & Bengtsson, P.-E. (2004). Characteristics of laser-induced incandescence from soot in studies of a time-dependent heat- and mass-transfer model. *Applied Physics B, 78*, 241–248. https://doi.org/10.1007/s00340-003-1362-9

Bladh, H., Johnsson, J., & Bengtsson, P.-E. (2008). On the dependence of the laser-induced incandescence (LII) signal on soot volume fraction for variations in particle size. *Applied Physics B, 90*, 109–125. https://doi.org/10.1007/s00340-007-2826-0

Bladh, H., Johnsson, J., & Bengtsson, P.-E. (2009). Influence of spatial laser energy distribution on evaluated soot particle sizes using two-colour laser-induced incandescence in a flat premixed ethylene/air flame. *Applied Physics B, 96*, 645–656. https://doi.org/10.1007/s00340-009-3523-y

Bladh, H., Johnsson, J., Olofsson, N.-E., Bohlin, A., & Bengtsson, P.-E. (2011a). Optical soot characterization using two-color laser-induced incandescence (2C-LII) in the soot growth region of a premixed flat flame. *Proceedings of the Combustion Institute, 33*, 641–648. https://doi.org/10.1016/j.proci.2010.06.166

Bladh, H., Johnsson, J., Rissler, J., Abdulhamid, H., Olofsson, N.-E., Sanati, M., Pagels, J., & Bengtsson, P.-E. (2011b). Influence of soot particle aggregation on time-resolved laser-induced incandescence signals. *Applied Physics B, 104*, 331–341. https://doi.org/10.1007/s00340-011-4470-y

Bond, T. C., Doherty, S. J., Fahey, D. W., Forster, P. M., Berntsen, T., DeAngelo, B. J., Flanner, M. G., Ghan, S., Kärcher, B., Koch, D., Kinne, S., Kondo, Y., Quinn, P. K., Sarofim, M. C., Schultz, M. G., Schulz, M., Venkataraman, C., Zhang, H., Zhang, S., Bellouin, N., Guttikunda, S. K., Hopke, P. K., Jacobson, M. Z., Kaiser, J. W., Klimont, Z., Lohmann, U., Schwarz, J. P., Shindell, D., Storelvmo, T., Warren, S. G., & Zender, C. S. (2013). Bounding the role of black carbon in the climate system: A scientific assessment. *Journal of Geophysical Research: Atmospheres, 118*, 5380–5552. https://doi.org/10.1002/jgrd.50171

Bukatyi, V. I., Sutorikhin, I. A., & Shaiduk, A. M. (1983). Combustion dynamics of a carbon particle in a CO_2 laser beam. *Combustion, Explosion and Shock Waves, 19*, 69–73. https://doi.org/10.1007/BF00790240

Burakov, V. S., Kondrashov, N. G., Stavrov, A. A., & Zakharova, I. S. (1977). Laser heating and sublimation of carbon particles in a flame. *Journal of Engineering Physics, 32*, 584–591. https://doi.org/10.1007/BF00860611

Butenko, Y. V., Kuznetsov, V. L., Chuvilin, A. L., Kolomiichuk, V. N., Stankus, S. V., Khairulin, R. A., & Segall, B. (2000). Kinetics of the graphitization of dispersed diamonds at "low" temperatures. *Journal of Applied Physics, 88*, 4380–4388. https://doi.org/10.1063/1.1289791

Cenker, E., Bruneaux, G., Dreier, T., & Schulz, C. (2015). Determination of small soot particles in the presence of large ones from time-resolved laser-induced incandescence. *Applied Physics B, 118*, 169–183. https://doi.org/10.1007/S00340-014-5966-Z

Cenker, E., & Roberts, W. L. (2017). Quantitative effects of rapid heating on soot-particle sizing through analysis of two-pulse LII. *Applied Physics B, 123*, 74. https://doi.org/10.1007/s00340-017-6653-7

Charwath, M., Suntz, R., & Bockhorn, H. (2011). Constraints of two-colour TiRe-LII at elevated pressures. *Applied Physics B, 104*, 427–438. https://doi.org/10.1007/s00340-011-4432-4

Chase, J., M.W. (1998). NIST JANAF thermochemical tables. 4th edition. *Journal of Physical and Chemical Reference Data Monograph, 9*. American Institute of Physics.

Chen, L., Wu, J., Yan, M., Wu, X., Gréhan, G., & Cen, K. (2017). Determination of soot particle size using time-gated laser-induced incandescence images. *Applied Physics B, 123*, 96. https://doi.org/10.1007/s00340-017-6669-z

Dalzell, W. H., & Sarofim, A. F. (1969). Optical constants of soot and their application to heat-flux calculations. *Journal of Heat Transfer, 91*, 100–104. https://doi.org/10.1115/1.3580063

Daun, K. J. (2009). Thermal accommodation coefficients between polyatomic gas molecules and soot in laser-induced incandescence experiments. *International Journal of Heat and Mass Transfer, 52*, 5081–5089. https://doi.org/10.1016/j.ijheatmasstransfer.2009.05.006

Desgroux, P., Lamoureux, N., & Faccinetto, A. (2024). Combining performances of E(m)-corrected LII and absorption for in situ measurements of the volume fraction of 2–4 nm soot particles. *Journal of Aerosol Science, 179*, Article 106385. https://doi.org/10.1016/j.jaerosci.2024.106385

Dobbins, R. A., & Megaridis, C. M. (1987). Morphology of flame-generated soot as determined by thermophoretic sampling. *Langmuir, 3*, 254–259. https://doi.org/10.1021/la00074a019

Du, Y., Xu, X., Chu, M., Guo, Y., & Wang, J. (2016). Air particulate matter and cardiovascular disease: The epidemiological, biomedical and clinical evidence. *Journal of Thoracic Disease, 8*, E8–E19. https://doi.org/10.3978/j.issn.2072-1439.2015.11.37

Dunne, L. J., Nolan, P. F., Munn, J., Terrones, M., Jones, T., Kathirgamanathan, P., Fernandez, J., & Hudson, A. D. (1997). Experimental verification of the dominant influence of extended carbon networks on the structural, electrical and magnetic properties of a common soot. *Journal of Physics: Condensed Matter, 9*, 10661–10673. https://doi.org/10.1088/0953-8984/9/48/010

Eckbreth, A. C. (1977). Effects of laser-modulated particulate incandescence on raman scattering diagnostics. *Journal of Applied Physics, 48*, 4473–4479. https://doi.org/10.1063/1.323458

Eremin, A. V., Gurentsov, E. V., Hofmann, M., Kock, B. F., & Schulz, C. (2006). TR-LII for sizing of carbon particles forming at room temperature. *Applied Physics B, 83*, 449–454. https://doi.org/10.1007/s00340-006-2199-9

Ewels, C. P., Heggie, M. I., & Briddon, P. R. (2002). Adatoms and nanoengineering of carbon. *Chemical Physics Letters, 351*, 178–182. https://doi.org/10.1016/S0009-2614(01)01371-9

Filippov, A. V., & Rosner, D. E. (2000). Energy transfer between an aerosol particle and gas at high temperature ratios in the knudsen transition regime. *International Journal of Heat and Mass Transfer, 43*, 127–138. https://doi.org/10.1016/S0017-9310(99)00113-1

Fuchs, N. A. (1934). Über die Verdampfungsgeschwindigkeit kleiner Tröpfchen in einer Gasatmosphäre. *Physikalische Zeitschrift der Sowjetunion, 6*, 225–243.

Fuchs, N. A. (1959). In R. S. Bradley (Ed.), *Evaporation and droplet growth in gaseous media*. Pergamon Press. ISBN 978-1483212203.

Goulay, F., Schrader, P. E., López-Yglesias, X., & Michelsen, H. A. (2013). A data set for validation of models of laser-induced incandescence from soot: Temporal profiles of LII signal and particle temperature. *Applied Physics B, 112*, 287–306. https://doi.org/10.1007/s00340-013-5504-4

Güttler, A., Zecho, T., & Küppers, J. (2004). A LEED and STM study of H(D) adsorption on C(0 0 0 1) surfaces. *Chemical Physics Letters, 395*, 171–176. https://doi.org/10.1016/j.cplett.2004.07.077

Hadef, R., Geigle, K. P., Meier, W., & Aigner, M. (2010). Soot characterization with laser-induced incandescence applied to a laminar premixed ethylene-air flame. *International Journal of Thermal Sciences, 49*, 1457–1467. https://doi.org/10.1016/j.ijthermalsci.2010.02.014

Hadef, R., Geigle, K. P., Zerbs, J., Sawchuk, R. A., & Snelling, D. R. (2013). The concept of 2D gated imaging for particle sizing in a laminar diffusion flame. *Applied Physics B, 112*, 395–408. https://doi.org/10.1007/s00340-013-5507-1

Hadwin, P. J., Sipkens, T. A., Thomson, K. A., Liu, F., & Daun, K. J. (2017). Quantifying uncertainty in auto-compensating laser-induced incandescence parameters due to multiple nuisance parameters. *Applied Physics B, 123*, 114. https://doi.org/10.1007/s00340-017-6693-z

Häger, J., Glatzer, D., Kuze, H., Fink, M., & Walther, H. (1997). Rotationally excited NO molecules incident on a graphite surface: Molecular rotation and translation after scattering. *Surface Science, 374*, 181–190. https://doi.org/10.1016/S0039-6028(96)01212-5

Hiers, R. (1997). Rarefaction effects in small particle combustion. *Journal of Thermophysics and Heat Transfer, 11*, 232–238. https://doi.org/10.2514/2.6227

Hiers, R. S. (2000). Critical behavior in small particle combustion. *Journal of Thermophysics and Heat Transfer, 14*, 53–58. https://doi.org/10.2514/2.6489

Hiers, R. (2008). A control volume derivation of the energy equation for LII modeling. *Applied Physics B, 92*, 635–641. https://doi.org/10.1007/s00340-008-3122-3

Hofeldt, D. L. (1993). Real-time soot concentration measurement technique for engine exhaust streams. *SAE Technical Paper.. ,* Article 930079. https://doi.org/10.4271/930079

Hofmann, M., Kock, B. F., Dreier, T., Jander, H., & Schulz, C. (2008). Laser-induced incandescence for soot-particle sizing at elevated pressure. *Applied Physics B, 90*, 629–639. https://doi.org/10.1007/s00340-007-2877-2

Hofmann, M., Kock, B., & Schulz, C. (2007). A web-based interface for modeling laser-induced incandescence (LIISim). *Proceedings of the Third European combustion meeting, chania, Greece*. http://www.LIIsim.com.

Jia, H., Ma, X., Yu, F., & Quaas, J. (2021). Significant underestimation of radiative forcing by aerosol–cloud interactions derived from satellite-based methods. *Nature Communications, 12*, 3649. https://doi.org/10.1038/s41467-021-23888-1

Jiaqiang, E., Xu, W., Ma, Y., Tan, D., Peng, Q., Tan, Y., & Chen, L. (2022). Soot formation mechanism of modern automobile engines and methods of reducing soot emissions: A review. *Fuel Processing Technology, 235*, Article 107373. https://doi.org/10.1016/j.fuproc.2022.107373

Johansson, K. O., El Gabaly, F., Schrader, P. E., Campbell, M. F., & Michelsen, H. A. (2017). Evolution of maturity levels of the particle surface and bulk during soot growth and oxidation in a flame. *Aerosol Science & Technology, 51*, 1333–1344. https://doi.org/10.1080/02786826.2017.1355047

Johnsson, J., Bladh, H., & Bengtsson, P.-E. (2010). On the influence of bimodal size distribution in particle sizing using laser-induced incandescence. *Applied Physics B, 99*, 817–823. https://doi.org/10.1007/s00340-010-3986-x

Johnsson, J., Bladh, H., Olofsson, N.-E., & Bengtsson, P.-E. (2013). Influence of soot aggregate structure on particle sizing using laser-induced incandescence: Importance of bridging between primary particles. *Applied Physics B, 112*, 321–332. https://doi.org/10.1007/s00340-013-5355-z

Kock, B. F., Tribalet, B., Schulz, C., & Roth, P. (2006). Two-color time-resolved LII applied to soot particle sizing in the cylinder of a diesel engine. *Combustion and Flame, 147*, 79–92. https://doi.org/10.1016/j.combustflame.2006.07.009

Konno, T. J., & Sinclair, R. (1995). Crystallization of amorphous carbon in carbon-cobalt layered thin films. *Acta Metallurgica et Materialia, 43*, 471–484. https://doi.org/10.1016/0956-7151(94)00289-T

Kuhlmann, S. A., Reimann, J., & Will, S. (2006). On heat conduction between laser-heated nanoparticles and a surrounding gas. *Journal of Aerosol Science, 37*, 1696–1716. https://doi.org/10.1016/j.jaerosci.2006.06.009

Kuhlmann, S. A., Reimann, R., & Will, S. (2005). Heat conduction issues in laser-induced incandescence. In *Proceedings of the international Bunsen discussion meeting 2005: Laser-induced incandescence, quantitative interpretation, modelling, application. September 25-28 (2005). CEUR workshop proceedings, 195* p. 11). Code 99269.

Leider, H., Krikorian, O., & Young, D. (1973). Thermodynamic properties of carbon up to the critical point. *Carbon, 11*, 555–563. https://doi.org/10.1016/0008-6223(73)90316-3

Lemaire, R., Bejaoui, S., & Therssen, E. (2013). Study of soot formation during the combustion of diesel, rapeseed methyl ester and their surrogates in turbulent spray flames. *Fuel, 107*, 147–161. https://doi.org/10.1016/j.fuel.2012.12.072

Lemaire, R., & Menanteau, S. (2021). Modeling laser-induced incandescence of diesel soot—Implementation of an advanced parameterization procedure applied to a refined LII model accounting for shielding effect and multiple scattering within aggregates for α_T and E(m) assessment. *Applied Physics B, 127*, 138. https://doi.org/10.1007/s00340-021-07665-y

Lemaire, R., & Menanteau, S. (2023a). Study of the wavelength dependence of the absorption function of diesel soot by LII modeling integrating the effect of multiple scattering within aggregates. *Applied Physics B, 129*, 79. https://doi.org/10.1007/s00340-023-08002-1

Lemaire, R., & Menanteau, S. (2023b). Benchmark of models commonly used to simulate laser-induced incandescence of soot. In *10th international conference on fluid flow, heat and mass transfer, FFHMT 2023, 158* pp. 1–8). https://doi.org/10.11159/ffhmt23.158

Lemaire, R., & Menanteau, S. (2024). Comparison of the predictive ability of standard and refined LII models to simulate experimental data taken from two databases from the literature. *10th international workshop on laser-induced incandescence*. Muskoka, Ontario, Canada, June 2024.

Lemaire, R., & Mobtil, M. (2015). Modeling laser-induced incandescence of soot: A new approach based on the use of inverse techniques. *Applied Physics B, 119*, 577–606. https://doi.org/10.1007/s00340-015-6032-1

Leroy, O., Perrin, J., Jolly, J., Péalat, M., & Lefebvre, M. (1997). Thermal accommodation of a gas on a surface and heat transfer in CVD and PECVD experiments. *Journal of Physics D Applied Physics, 30*, 499–509. https://doi.org/10.1088/0022-3727/30/4/001

Lippmann, M. (2014). Toxicological and epidemiological studies of cardiovascular effects of ambient air fine particulate matter (PM2.5) and its chemical components: Coherence and public health implications. *Critical Reviews in Toxicology, 44*, 299–347. https://doi.org/10.3109/10408444.2013.861796

Liu, F. (2024). *Modeling laser-induced annealing of young soot during LII*. Ontario, Canada: 10th International Workshop on Laser-Induced Incandescence, Muskoka. June 2024. pp. 24-27.

Liu, F., Daun, K. J., Snelling, D. R., & Smallwood, G. J. (2006b). Heat conduction from a spherical nano-particle: Status of modeling heat conduction in laser-induced incandescence. *Applied Physics B, 83*, 355–382. https://doi.org/10.1007/s00340-006-2194-1

Liu, F., Rogak, S., Snelling, D. R., Saffaripour, M., Thomson, K. A., & Smallwood, G. J. (2016). Effects of laser fluence non-uniformity on ambient-temperature soot measurements using the auto-compensating laser-induced incandescence technique. *Applied Physics B, 122*, 286. https://doi.org/10.1007/s00340-016-6553-2

Liu, F., Sipkens, T. A., & Corbin, J. C. (2025). Soot volume fraction anomaly in AC-LII measurements revisited: The effect of laser induced annealing. In *Proceedings of the combustion institute – Canadian section, spring technical meeting*. Calgary, Alberta, May 12-15 (2025).

Liu, F., & Smallwood, G. J. (2013). Relationship between soot volume fraction and LII signal in AC-LII: Effect of primary soot particle diameter polydispersity. *Applied Physics B, 112*, 307–319. https://doi.org/10.1007/s00340-012-5330-0

Liu, F., Smallwood, G. J., & Snelling, D. R. (2005). Effects of primary particle diameter and aggregate size distribution on the temperature of soot particles heated by pulsed lasers. *Journal of Quantitative Spectroscopy and Radiative Transfer, 93*, 301–312. https://doi.org/10.1016/j.jqsrt.2004.08.027

Liu, F., & Snelling, D. R. (2007). The unsteady-state energy conservation equation for a small spherical particle in LII modeling. *Applied Physics B, 89*, 115–121. https://doi.org/10.1007/s00340-007-2761-0

Liu, F., Snelling, D. R., & Smallwood, G. J. (2021). A critical evaluation of the thermal accommodation coefficient of soot determined by the laser-induced incandescence technique. In *Proceedings of the international bunsen discussion meeting 2005: Laser-induced incandescence, quantitative interpretation, modelling, application. September 25-28 (2005). CEUR workshop proceedings, 195* p. 35). Code 99269.

Liu, F., Yang, M., Hill, F. A., Snelling, D. R., & Smallwood, G. J. (2006a). Influence of polydisperse distributions of both primary particle and aggregate size on soot temperature in low-fluence LII. *Applied Physics B, 83*, 383–395. https://doi.org/10.1007/s00340-006-2196-z

Liu, F., Yon, J., Fuentes, A., Lobo, P., Smallwood, G. J., & Corbin, J. C. (2020). Review of recent literature on the light absorption properties of Black carbon: Refractive index, mass absorption cross section, and absorption function. *Aerosol Science & Technology, 54*, 33–51. https://doi.org/10.1080/02786826.2019.1676878

López-Yglesias, X., Schrader, P. E., & Michelsen, H. A. (2014). Soot maturity and absorption cross sections. *Journal of Aerosol Science, 75*, 43–64. https://doi.org/10.1016/j.jaerosci.2014.04.011

Maffi, S., De Iuliis, S., Cignoli, F., & Zizak, G. (2011). Investigation on thermal accommodation coefficient and soot absorption function with two-color Tire-LII technique in rich premixed flames. *Applied Physics B, 104*, 357–366. https://doi.org/10.1007/s00340-011-4536-x

Mansmann, R., Terheiden, T., Schmidt, P., Menser, J., Dreier, T., Endres, T., & Schulz, C. (2018). LIISim: A modular signal processing toolbox for laser-induced incandescence measurements. *Applied Physics B, 124*, 69. https://doi.org/10.1007/s00340-018-6934-9

Marcos, P. A., López, M. J., Rubio, A., & Alonso, J. A. (1997). Thermal road for fullerene annealing. *Chemical Physics Letters, 273*, 367–370. https://doi.org/10.1016/S0009-2614(97)00616-7

Martin, J. W., Salamanca, M., & Kraft, M. (2022). Soot inception: Carbonaceous nanoparticle formation in flames. *Progress in Energy and Combustion Science, 88*, Article 100956. https://doi.org/10.1016/j.pecs.2021.100956

Mathworks. (2013). *Matlab documentation*. Available at: http://www.mathworks.com.

McCoy, B. J., & Cha, C. Y. (1974). Transport phenomena in the rarefied gas transition regime. *Chemical Engineering Science, 29*, 381–388. https://doi.org/10.1016/0009-2509(74)80047-3

Megaridis, C. M., & Dobbins, R. A. (1989). Comparison of soot growth and oxidation in smoking and non–smoking ethylene diffusion flames. *Combustion Science and Technology, 66*, 1–16. https://doi.org/10.1080/00102208908947136

Melton, L. A. (1984). Soot diagnostics based on laser heating. *Applied Optics, 23*, 2201–2208. https://doi.org/10.1364/ao.23.002201

Menanteau, S., & Lemaire, R. (2020). Analysis of the influence of the conduction sub-model formulation on the modeling of laser-induced incandescence of diesel soot aggregates. *Entropy, 22*, 21. https://doi.org/10.3390/e22010021

Menanteau, S., & Lemaire, R. (2021). Sensitivity analysis focusing on model formulations and parameterization for the simulation of laser-induced incandescence signals of soot. *Appl. Therm. Eng. Heat Transfer Fluid Mech. Thermodyn. Virtual Conf.*, 25–28. July 2021.

Menanteau, S., & Lemaire, R. (2022). Parameterization of a refined model aimed at simulating laser-induced incandescence of soot using a visible excitation wavelength of 532 nm. *Journal of Advanced Research in Fluid Mechanics and Thermal Sciences, 98*, 92–103. https://doi.org/10.37934/arfmts.98.1.92104

Mi, X., Saylam, A., Endres, T., Schulz, C., & Dreier, T. (2021). Near-threshold soot formation in premixed flames at elevated pressure. *Carbon, 181*, 143–154. https://doi.org/10.1016/j.carbon.2021.05.014

Michelsen, H. A. (2003). Understanding and predicting the temporal response of laser-induced incandescence from carbonaceous particles. *The Journal of Chemical Physics, 118*, 7012–7045. https://doi.org/10.1063/1.1559483

Michelsen, H. A. (2009). Derivation of a temperature-dependent accommodation coefficient for use in modeling laser-induced incandescence of soot. *Applied Physics B, 94*, 103–117. https://doi.org/10.1007/s00340-008-3278-x

Michelsen, H. A. (2017). Probing soot formation, chemical and physical evolution, and oxidation: A review of in situ diagnostic techniques and needs. *Proceedings of the Combustion Institute, 36*, 717–735. https://doi.org/10.1016/j.proci.2016.08.027

Michelsen, H. A. (2021). Effects of maturity and temperature on soot density and specific heat. *Proceedings of the Combustion Institute, 38*, 1197–1205. https://doi.org/10.1016/j.proci.2020.06.383

Michelsen, H. A., Colket, M. B., Bengtsson, P.-E., D'Anna, A., Desgroux, P., Haynes, B. S., Houston Miller, J., Nathan, G. J., Pitsch, H., & Wang, H. (2020). A review of terminology used to describe soot formation and evolution under combustion and pyrolytic conditions. *ACS Nano, 14*, 12470–12490. https://doi.org/10.1021/acsnano.0c06226

Michelsen, H. A., Linne, M. A., Kock, B. F., Hofmann, M., Tribalet, B., & Sculz, C. (2008). Modeling laser-induced incandescence of soot: Enthalpy changes during sublimation, conduction, and oxidation. *Applied Physics B, 93*, 645–656. https://doi.org/10.1007/s00340-008-3181-5

Michelsen, H. A., Liu, F., Kock, B. F., Bladh, H., Boiarciuc, A., Charwath, M., Dreier, T., Hadef, R., Hofmann, M., Reimann, J., Will, S., Bengtsson, P.-E., Bockhorn, H., Foucher, F., Geigle, K.-P., Mounaïm-Rousselle, C., Schulz, C., Stirn, R., Tribalet, B., & Suntz, R. (2007). Modeling laser-induced incandescence of soot: A summary and comparison of LII models. *Applied Physics B, 87*, 503–521. https://doi.org/10.1007/s00340-007-2619-5

Michelsen, H. A., Schrader, P. E., & Goulay, F. (2010). Wavelength and temperature dependences of the absorption and scattering cross sections of soot. *Carbon, 48*, 2175–2191. https://doi.org/10.1016/j.carbon.2010.02.014

Michelsen, H. A., Schulz, C., Smallwood, G. J., & Will, S. (2015). Laser induced incandescence: Particulate diagnostics for combustion, atmospheric, and industrial applications. *Progress in Energy and Combustion Science, 51*, 2–48. https://doi.org/10.1016/j.pecs.2015.07.001

Michelsen, H. A., Witze, P. O., Kayes, D., & Hochgreb, S. (2003). Time-resolved laser-induced incandescence of soot: The influence of experimental factors and microphysical mechanisms. *Applied Optics, 42*, 5577–5590. https://doi.org/10.1364/ao.42.005577

Mitrani, J. M., Shneider, M. N., Stratton, B. C., & Raitses, Y. (2016). Modeling thermionic emission from laser-heated nanoparticles. *Applied Physics Letters, 108*, Article 054101. https://doi.org/10.1063/1.4940992

Miura, Y., Kasai, H., Diño, W. A., Nakanishi, H., & Sugimoto, T. (2003). Effective pathway for hydrogen atom adsorption on graphene. *Journal of the Physical Society of Japan, 72*, 995–997. https://doi.org/10.1143/JPSJ.72.995

Mobtil, M., & Lemaire, R. (2012). Modeling laser-induced incandescence of soot integrating spatial and temporal dependences of parameters involved in energy and mass balances. In *Proceedings of the 5th International Workshop Meeting on Laser-Induced Incandescence*. LII2012, Le Touquet Paris-Plage, France, 8–11 may 2012, CEUR Workshop Proceedings: 865. Code 101856.

Ni, T., Pinson, J. A., Gupta, S., & Santoro, R. J. (1995). Two-dimensional imaging of soot volume fraction by the use of laser-induced incandescence. *Applied Optics, 34*, 7083–7091. https://doi.org/10.1364/AO.34.007083

Puri, R., Richardson, T. F., Santoro, R. J., & Dobbins, R. A. (1993). Aerosol dynamic processes of soot aggregates in a laminar ethene diffusion flame. *Combustion and Flame, 92*, 320–333. https://doi.org/10.1016/0010-2180(93)90043-3

Ramanathan, V., & Carmichael, G. (2008). Global and regional climate changes due to black carbon. *Nature Geoscience, 1*, 221–227. https://doi.org/10.1038/ngeo156

Reimann, J., Kuhlmann, S.-A., & Will, S. (2009). 2D aggregate sizing by combining laser-induced incandescence. *Applied Physics B, 96*, 583–592. https://doi.org/10.1007/s00340-009-3546-4

Rettner, C. T., Auerbach, D. J., Tully, J. C., & Kleyn, A. W. (1996). Chemical dynamics at the gas-surface interface. *Journal of Physical Chemistry, 100*, 13021–13033. https://doi.org/10.1021/jp9536007

Saffaripour, M., Geigle, K.-P., Snelling, D. R., Smallwood, G. J., & Thomson, K. A. (2015). Influence of rapid laser heating on the optical properties of in-flame soot. *Applied Physics B, 119*, 621–642. https://doi.org/10.1007/s00340-015-6072-6

Schulz, C., Kock, B. F., Hofmann, M., Michelsen, H., Will, S., Bougie, B., Suntz, R., & Smallwood, G. (2006). Laser-induced incandescence: Recent trends and current questions. *Applied Physics B, 83*, 333–354. https://doi.org/10.1007/s00340-006-2260-8

Sha, X., & Jackson, B. (2002). First-principles study of the structural and energetic properties of H atoms on a graphite (0 0 0 1) surface. *Surface Science, 496*, 318–330. https://doi.org/10.1016/S0039-6028(01)01602-8

Shampine, L. F., & Reichelt, M. W. (1997). The MATLAB ODE suite. *SIAM Journal on Scientific Computing, 18*, 1–22. https://doi.org/10.1137/S1064827594276424

Sipkens, T. A., Hadwin, P. J., Grauer, S. J., & Daun, K. J. (2017). Applying model selection to laser-induced incandescence. In *9th International conference on inverse problems in engineering, waterloo*. Canada, May 23-26 (2017).

Sipkens, T. A., Hadwin, P. J., Grauer, S. J., & Daun, K. J. (2018a). Using Bayesian model selection and time-resolved laser-induced incandescence to probe the sublimation properties of soot. In *Proceedings of the combustion Institute – Canadian section, spring technical meeting*. Toronto, Canada, May 14-17 (2018).

Sipkens, T. A., Hadwin, P. J., Grauer, S. J., & Daun, K. J. (2018b). Predicting the heat of vaporization of iron at high temperatures using time-resolved laser-induced incandescence and Bayesian model selection. *Journal of Applied Physics, 123*, Article 095103. https://doi.org/10.1063/1.5016341

Sipkens, T. A., Menser, J., Mansmann, R., Schulz, C., & Daun, K. J. (2019). Investigating temporal variation in the apparent volume fraction measured by time-resolved laser-induced incandescence. *Applied Physics B, 125*, 140. https://doi.org/10.1007/s00340-019-7251-7

Smallwood, G. J., Snelling, D. R., Liu, F., & Gülder, Ö. L. (2001). Clouds over soot evaporation: Errors in modeling laser-induced incandescence of soot. *Journal of Heat Transfer, 123*, 814–818. https://doi.org/10.1115/1.1370507

Snelling, D. R., Link, O., Thomson, K. A., & Smallwood, G. J. (2011). Measurement of soot morphology by integrated LII and elastic light scattering. *Applied Physics B, 104*, 385–397. https://doi.org/10.1007/s00340-011-4394-6

Snelling, D. R., Liu, F., Smallwood, G. J., & Gülder, Ö. L. (2000). Evaluation of the nanoscale heat and mass transfer model of LII: Prediction of the excitation intensity. In *Proceedings of NHTC'00 – 34th national heat transfer conference*. Pittsburgh, Pennsylvania, August 20-22 (2000).

Snelling, D. R., Liu, F., Smallwood, G. J., & Gülder, Ö. L. (2004). Determination of the soot absorption function and thermal accommodation coefficient using low-fluence LII in a laminar coflow ethylene diffusion flame. *Combustion and Flame, 136*, 180–190. https://doi.org/10.1016/j.combustflame.2003.09.013

Snelling, D. R., Smallwood, G. J., Liu, F., Gülder, Ö. L., & Bachalo, W. D. (2005). A calibration-independent laser-induced incandescence technique for soot measurement by detecting absolute light intensity. *Applied Optics, 44*, 6773–6785. https://doi.org/10.1364/AO.44.006773

Snelling, D. R., Thomson, K. A., Liu, F., & Smallwood, G. J. (2009). Comparison of LII derived soot temperature measurements with LII model predictions for soot in a laminar diffusion flame. *Applied Physics B, 96*, 657–669. https://doi.org/10.1007/s00340-009-3614-9

Sun, Z. W., Gu, D. H., Nathan, G. J., Alwahabi, Z. T., & Dally, B. B. (2015). Single-shot, time-resolved planar laser-induced incandescence (TiRe-LII) for soot primary particle sizing in flames. *Proceedings of the Combustion Institute, 35*, 3673–3680. https://doi.org/10.1016/j.proci.2014.07.066

Talebi Moghaddam, S., & Daun, K. J. (2018). Plasma emission during time-resolved laser-induced incandescence measurements of aerosolized metal nanoparticles. *Applied Physics B, 124*, 159. https://doi.org/10.1007/s00340-018-7028-4

Török, S., Mannazhi, M., & Bengtsson, P.-E. (2021). Laser-induced incandescence (2λ and 2C) for estimating absorption efficiency of differently matured soot. *Applied Physics B, 127*, 96. https://doi.org/10.1007/s00340-021-07638-1

Vander Wal, R. L., Ticich, T. M., & Stephens, A. B. (1998). Optical and microscopy investigations of soot structure alterations by laser-induced incandescence. *Applied Physics B, 67*, 115–123. https://doi.org/10.1007/s003400050483

Vander Wal, R. L., Ticich, T. M., & Stephens, A. B. (1999). Can soot primary particle size be determined using laser-induced incandescence. *Combustion and Flame, 116*, 291–296. https://doi.org/10.1016/S0010-2180(98)00040-6

Wang, H. (2011). Formation of nascent soot and other condensed-phase materials in flames. *Proceedings of the Combustion Institute, 33*, 41–67. https://doi.org/10.1016/j.proci.2010.09.009

Weeks, R. W., & Duley, W. W. (1974). Aerosol-particle sizes from light emission during excitation by TEA CO_2 laser pulses. *Journal of Applied Physics, 45*, 4661–4662. https://doi.org/10.1063/1.1663111

Will, S., Schraml, S., & Leipertz, A. (1995). Two-dimensional soot-particle sizing by time-resolved laser-induced incandescence. *Optics Letters, 20*, 2342–2344. https://doi.org/10.1364/OL.20.002342

Xu, L., Wang, Y., & Liu, D. (2022). Effects of oxygenated biofuel additives on soot formation: A comprehensive review of laboratory-scale studies. *Fuel, 313*, Article 122635. https://doi.org/10.1016/j.fuel.2021.122635

Yon, J., Lemaire, R., Therssen, E., Desgroux, P., Coppalle, A., & Ren, K. F. (2011). Examination of wavelength dependent soot optical properties of diesel and diesel/rapeseed methyl ester mixture by extinction spectra analysis and LII measurements. *Applied Physics B, 104*, 253–271. https://doi.org/10.1007/s00340-011-4416-4

Yon, J., Liu, F., Bescond, A., Caumont-Prim, C., Roze, C., Ouf, F.-X., & Coppalle, A. (2014). Effects of multiple scattering on radiative properties of soot fractal aggregates. *Journal of Quantitative Spectroscopy and Radiative Transfer, 133*, 374–381. https://doi.org/10.1016/j.jqsrt.2013.08.022

Yon, J., Therssen, E., Liu, F., Bejaoui, S., & Hebert, D. (2015). Influence of soot aggregate size and internal multiple scattering on LII signal and the absorption function variation with wavelength determined by the TEW-LII method. *Applied Physics B, 119*, 643–655. https://doi.org/10.1007/s00340-015-6116-y

Zecho, T., Güttler, A., Sha, X., Jackson, B., & Küppers, J. (2002). Adsorption of hydrogen and deuterium atoms on the (0001) graphite surface. *The Journal of Chemical Physics, 117*, 8486–8492. https://doi.org/10.1063/1.1511729

Zhang, Y., Liu, F., Clavel, D., Smallwood, G. J., & Lou, C. (2019). Measurement of soot volume fraction and primary particle diameter in oxygen enriched ethylene diffusion flames using the laser-induced incandescence technique. *Energy, 177*, 421–432. https://doi.org/10.1016/j.energy.2019.04.062

Zhang, Z., Zhou, L., & He, X. (2023). Can laser-induced incandescence calibrated by laser extinction method be used for quantitative determination of soot volume fraction in laminar flames? *Applications in Energy and Combustion Science, 13*, Article 100103. https://doi.org/10.1016/j.jaecs.2022.100103

Zheng, A. X., Manikandan, S. R., Wonfor, S. E., Stainberg, A. M., & Mazumdar, Y. C. (2023). Planar time-resolved laser-induced incandescence for pressurized premixed Jet-A combustion. *Applied Physics B, 129*, 71. https://doi.org/10.1007/s00340-023-08015-w